THESIS

ELECTROHYDRODYNAMIC FLOW IN A BARBED PLATE ELECTROSTATIC PRECIPITATOR

Submitted by

Peter J. McKinney

Department of Civil Engineering

In partial fulfillment of the requirements

for the Degree of Master of Science

Colorado State University

Fort Collins, Colorado

Summer 1988

COLORADO STATE UNIVERSITY

July 8, 1988

WE HEREBY RECOMMEND THAT THE THESIS PREPARED UNDER OUR SUPERVISION BY PETER J. MCKINNEY ENTITLED ELECTROHYDRODYNAMIC FLOW IN A BARBED PLATE ELECTROSTATIC PRECIPITATOR BE ACCEPTED AS FULFILLING IN PART REQUIREMENTS FOR THE DEGREE OF MASTER OF SCIENCE.

Committee on Graduate Work

Paul J. Wilbur

Virgil A. Sandborn

Robert N. Meroney

Jane V. Davidson
Adviser

Department Head

ABSTRACT OF THESIS

ELECTROHYDRODYNAMIC FLOW IN A BARBED PLATE
ELECTROSTATIC PRECIPITATOR

The large scale secondary flows and turbulence induced by the inhomogeneous negative corona discharge in the conventional wire-plate precipitator are known to reduce collection efficiencies, particularly in applications with high mass loadings of fine particulates. Electrohydrodynamic theory suggests that a modification in electrode geometry is necessary to control the electrically induced flow. A plate-plate precipitator using a barbed plate discharge electrode is designed to provide a more uniform current density distribution. Electrical and fluid dynamic characteristics of four model barbed plate electrodes, with varying plate-to-plate and barb spacing, are evaluated and compared to characteristics of a laboratory wire-plate precipitator in a specially designed wind tunnel facility. Current-voltage characteristics of each electrode are presented and the visual appearance of the corona discharge discussed. Hot-film anemometer measurements of the turbulent flow field downstream of the active precipitator include mean and turbulence intensity profiles, as well as spectral analysis of the flow. Gas eddy diffusivities are estimated from integral length scale calculations. A laser light sheet is used to visualize the flow in the inter-electrode space.

Results show that the electical characteristics of the planar electrodes are well within the range needed for industrial precipitation and that the scale of the current inhomogeneities within

the precipitator are reduced. Fluid dynamic measurements confirm that electrode geometry has a significant effect on the electrohydrodynamic turbulence production. Turbulence intensity data indicate that the point discharges in the planar geometry cause higher turbulence levels than the wire discharges. Turbulent diffusivites are correspondingly higher in the planar geometry. These results indicate that mixing may actually be enhanced in the suggested design.

Flow field measurements made downstream of the precipitator may not however be representative of the electrically induced flow within the precipitator. Plate end effects observed in the visualization procedure may have a significant effect on the downstream flow and bias the meaurements. Additional study is necessary to determine if the planar geometry is a viable design. The most important test of any new precipitation design is measurement of its particle collection efficiency.

Peter J. McKinney
Fluid Mechanics Program
Civil Engineering Department
Colorado State University
Fort Collins, Colorado 80523
July, 1988

ACKNOWLEDGMENTS

I am indebted to Dr. J. H. Davidson for her guidance and many hours of help in preparing this thesis. Thanks are also due to my parents, whose patient support and guidance helped me to push forward at difficult times. Finally, the support of the U.S. Environmental Protection Agency through Grant No. R-813645-01-0 is gratefully acknowledged.

TABLE OF CONTENTS

LIST OF TABLES

LIST OF FIGURES

NOMENCLATURE

A	collection surface area
$E(f)$	nondimensional power spectrum
E_i	electric field
f	frequency
f_c	Nyquist Frequency
F	dimensionless electric number, $IL/\beta A\rho U^2$
g	gravitational acceleration
$G(f)$	power spectrum
h	sampling interval
I	total current, turbulence intensity
J_i	current density vector
K	eddy diffusivity
ℓ	integral length scale, characteristic eddy size
L	collector plate spacing
N	number of samples
$\rho(u')$	probability density
P	gas pressure
$R(\tau)$	autocorrelation function
Re	dimensionless Reynolds number, uL/ν
t	time
T	total sampling time
u'	fluctuating velocity
u_i	gas velocity vector
u_{rms}	root mean square velocity

U	bulk or mean gas speed
w_e	particle electric migration velocity
x_i	spatial cartesian coordinate
y	Fourier transform of fluctuating velocity data
z	elevation

Greek Symbols

β	ion mobility
ϵ	electric permittivity
ϵ_{ijk}	alternating tensor
λ	eddy size
η	precipitator efficiency
μ	fluid viscosity
ν	fluid kinematic viscosity
ρ	fluid density
ρ_c	ionic space charge density
ϕ	electric potential

CHAPTER 1

INTRODUCTION

Electrostatic precipitation is the process of removing suspended particles from a gas stream by using a strong electric field. Particles are first charged via a corona discharge and are subsequently carried to a nearby collection plate under the influence of the prevailing electric field. Electrostatic precipitators are widely used in industrial applications such as coal fired power generation plants and cement factories to remove pollutants from the stack effluent. The typical industrial precipitator is the wire-plate design, a section of which is shown in Figure 1.1.

The wire-plate precipitator is operated by applying a high voltage to wires which are suspended between electrically grounded plates. Since the radius of curvature of the wires is very small compared to both the radius of curvature of the plate and distance from the wires to the plate, an electrical breakdown of the gas in the vicinity of the wires can occur without a complete sparkover to the ground plate. This local ionization of gas is known as a corona discharge and is observed as a visible glow around the wire electrode. Ions with charge like that of the wire electrodes move out of the corona region along electric field lines, traveling in the direction of decreasing field strength. Generally, large scale precipitators employ negatively charged wire electrodes to generate the corona

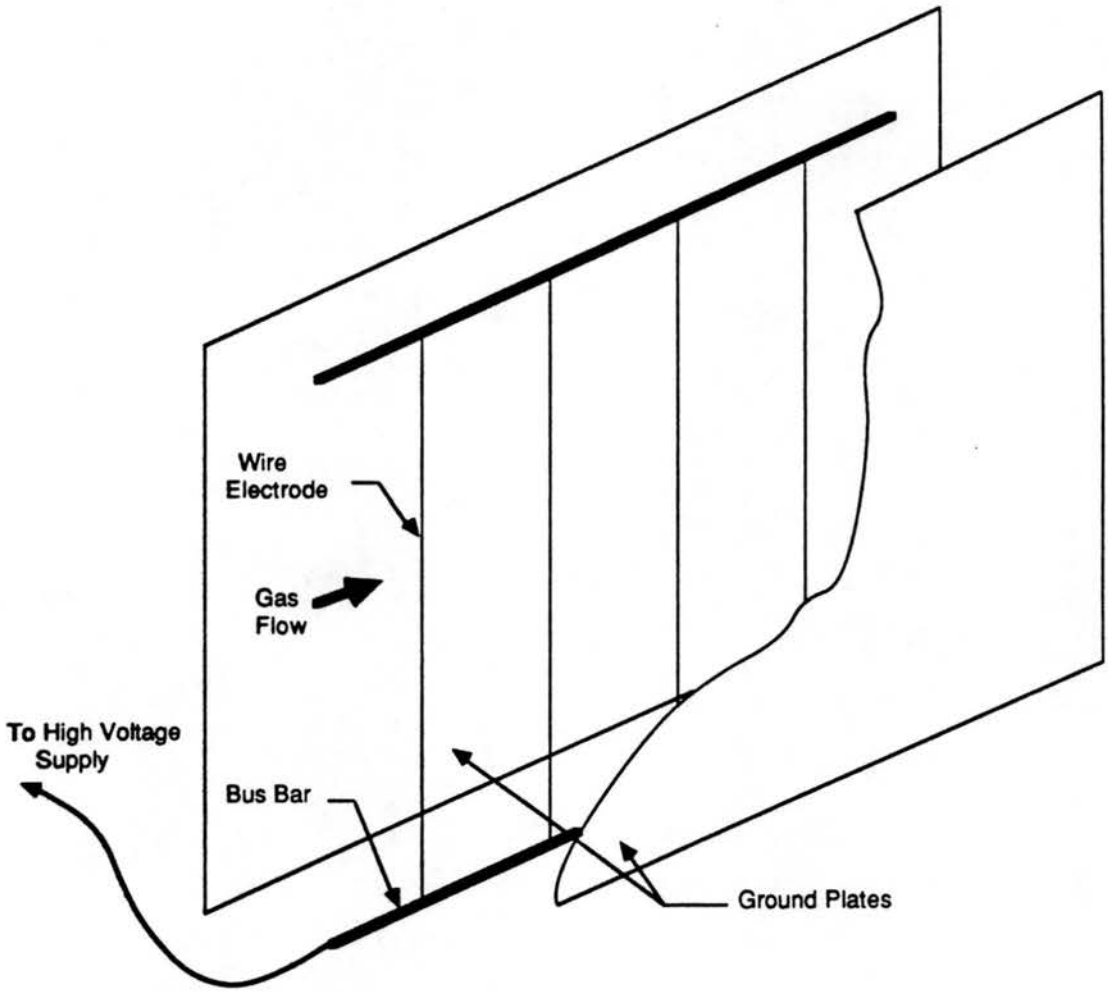

Figure 1.1. Schematic of a wire-plate precipitator.

discharge. The negative corona is distinctive in that discrete tufts of the visible corona glow appear at various locations along the wire.

Particle collection in the precipitator is accomplished through particle interaction with ions in the inter-electrode space. Particles being convected downstream in the flue gas become charged either by an ordered collision with an ion or by a collision due to turbulent diffusion. Once charged, a particle migrates toward the grounded collector plate under the influence of the electric field and the bulk gas motion and eventually adheres to the plate, thus becoming "collected". The collection plates are rapped with mechanical hammers at periodic intervals. As a result, the accumulated collected dust falls into hoppers beneath the active precipitator.

Although the mass collection efficiencies of modern precipitators can be as high as 99 percent, much of the mass escaping the precipitator is in the form of fine particulates. As a result, the actual collection efficiency in terms of particles collected is much lower. There are a number of factors which may inhibit the collection of smaller diameter particles or reduce precipitator efficiency in general. Back corona can form on the collector plates in the presence of particles with high electrical resistivity. Also, particle re-entrainment can occur during the plate rapping procedure. This allows particles to re-join the bulk gas flow and be convected out of the precipitator. Gas "sneakage" is another problem, one in which some of the particle laden gas eludes the electric field altogether. Particles sometimes pass below the discharge wires through the hopper region or through the low electric field regions between the negative corona tufts. Gas disturbances due to duct geometry and upstream conditions can also cause a reduction in precipitator efficiency.

Recent evidence exists that the corona discharge itself produces significant flow modification that may reduce collection efficiencies, particularly for fine particles which tend to follow the gas motion closely.

In this study a novel planar electrode is experimentally investigated to determine if electrically induced flow disturbances can be controlled through a modification in electrode geometry. The design of the planar electrode is based on the concept that a more uniform distribution of current within a precipitator may reduce the scale of the electrohydrodynamic (EHD) flow and thus reduce mixing.

In order to test the effectiveness of the novel planar electrode design, a small precipitator test section is constructed with an aspect ratio of 1 to 4 in an existing wind tunnel at the Fluid Dynamics and Diffusion Laboratory at Colorado State University. The model precipitator is easily modified to accommodate either a series of the traditional wire electrodes or a new novel planar electrode. A series of hot-film anemometer velocity measurements are made downstream of the test section for varying wire and planar electrode geometries. Both gas (air) velocity and current density are varied to cover the range observed in industrial precipitators.

Analyses of the hot-film velocity data include calculations of mean velocity, turbulence intensity, and probability density functions for each flow. Power spectral density functions, integral length scales, and eddy diffusivities are also computed to obtain information on the scale of turbulence generated by each electrode geometry.

Additionally, flow visualization is performed by introducing smoke into the channel upstream of the precipitator and examining the flow field in various planes using a laser light sheet.

Results confirm that electrode geometry plays a significant role in turbulence generation. Although theory suggests that secondary flows may be reduced in a planar geometry, analysis of the flow downstream of a barbed planar electrode indicates that turbulent intensities and diffusivities are increased as much as 50 percent over the conventional wire-plate design.

CHAPTER 2

BACKGROUND

2.1 Electrohydrodynamic Flows in the Wire-Plate Precipitator

Electrically induced secondary flow, commonly referred to as the corona or electric wind, is the result of an electrode geometry that produces a non-uniform (asymmetric) electric field. Although the phenomenon has only relatively recently been studied in electrostatic precipitators, it was first encountered in the early 1700's when Francis Hauksbee (1709) felt a weak blowing sensation when he held a charged tube near his face. It wasn't until much later that the first qualitative work was reported. Chattock (1899) developed a relationship between the electric wind pressure and the corona current. A more complete history of the corona wind phenomenon is provided by Robinson (1963).

It is well documented that the corona discharge in the wire-plate geometry of an electrostatic precipitator results in an electric wind. The early numerical work of Ramadan and Soo (1969) predicted a circulating secondary flow between the wire and plate electrodes under the assumptions of laminar flow and uniform positive corona discharge along the wire. Yabe et al. (1978) and Yamamoto & Velkoff (1981) went a step further by attaining experimental verification of the numerical predictions. In both cases, two dimensional vortices were observed in the plane perpendicular to the wire electrodes as a result of the corona jet impinging on the ground plate. Yabe et al. examined only

the pressure fields at the electrodes in order to make a fluid flow field prediction. Yamamoto and Velkoff, on the other hand, used the schlieren optical technique to study the fluid motion and a smoke visualization procedure to simulate the motion of charged particles.

The experimental work of Yabe et al. and that of Yamamoto and Velkoff was performed using a positive corona discharge. Because a positive corona is inherently more stable and uniform than a negative corona, these studies do not accurately depict the true picture of the electrically modified flow within the typical industrial electrostatic precipitator. The uniform discharge assumed is rarely possible outside of a controlled laboratory environment. A negative corona is used in most precipitators because it is advantageous in obtaining higher sparkover currents. Since a negative corona depends upon the availability of electrons on the electrode surface, the discharge is spotty and appears as "tufts". In addition dust, corrosion, and other electrode surface imperfections may cause a non-uniform discharge in either the negative or the positive configuration. Figure 2.1 depicts the discharge structure in a uniform corona discharge as compared to a nonuniform discharge.

A number of experimental studies have shown that the negative corona discharge results in an increase in the turbulence level of the gas flow and/or secondary flows within an electrostatic precipitator. Leonard et al. (1981,1983) made use of both smoke-wire visualization and hot-wire anemometry to show an increase in turbulence due to a negative corona at gas velocities less than 2.0 m/sec in a small scale model precipitator. Davidson and Shaughnessy's (1984,1986) hot wire anemometer studies of the flow in a large scale laboratory precipitator indicate that a negative corona discharge can produce

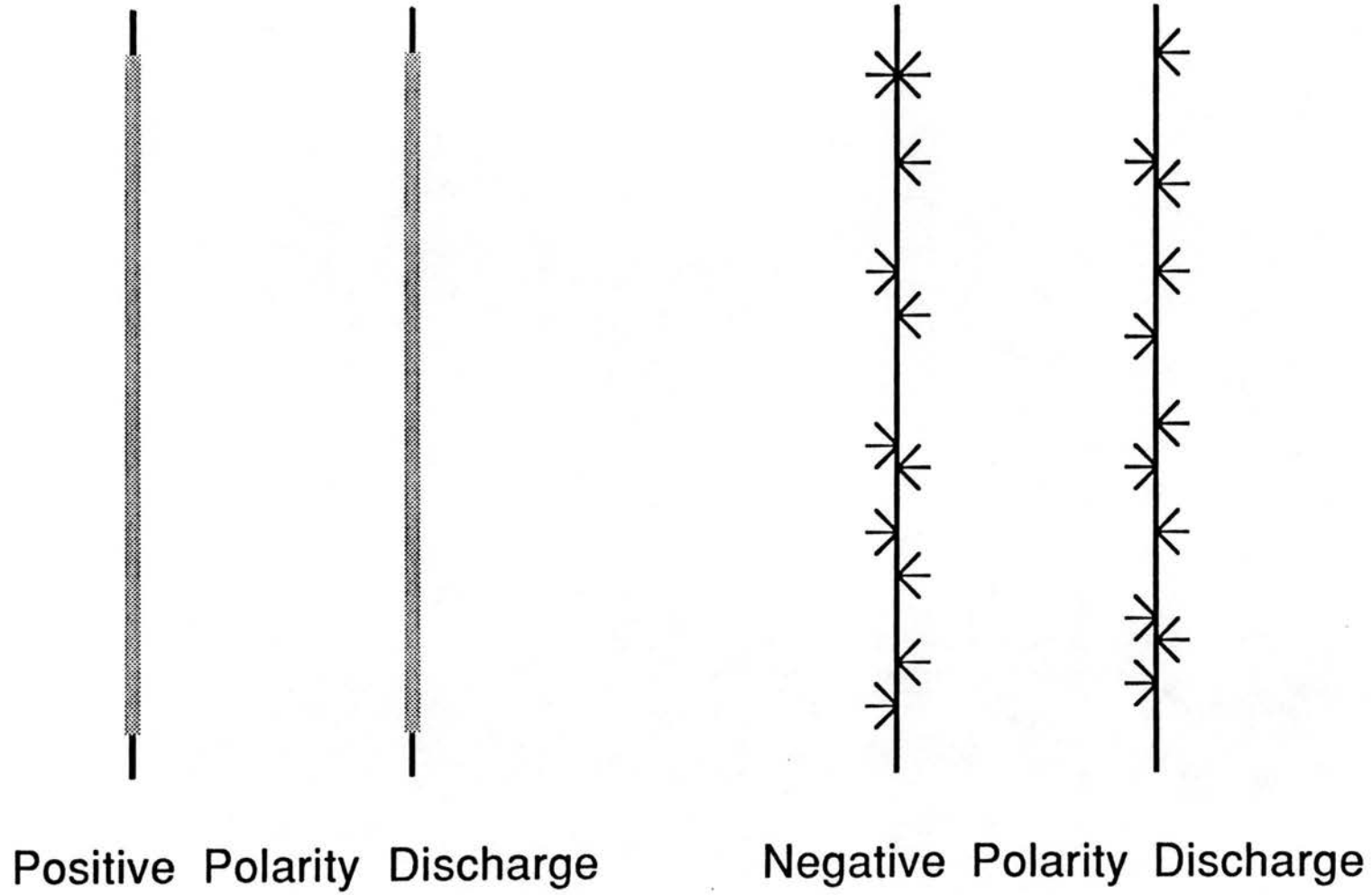

Figure 2.1. Corona discharge structure with positive and negative polarities.

turbulence levels as much as three times greater than the normal aerodynamic turbulence at gas flow speeds of 1.0 m/sec. Ushimaru et al. (1982) discovered horizontal vortical motions in a model precipitator using a laser Doppler velocimeter and laser light sheets. The vortical motions observed appeared as a result of the strong discharge at specific corona tufts. Also using laser Doppler anemometry, Larsen and Christensen (1986) measured similar axial rolls in a slightly larger test section. The rolls were forced into a structured pattern using barbs on the wire electrodes to create corona tufts at regular intervals.

In addition to creating electrically generated flow disturbances, the tuft-like character of the negative discharge may affect precipitator performance by providing areas with low or zero current. Yamamoto and Sparks (1986) created a three dimensional computer model of the negative corona tufts and from the results hypothesized that sneakage of the particles between tufts results in a decrease in precipitator efficiency.

2.2 Precipitator Efficiency

Traditionally, precipitator design is based upon the Deutsch efficiency equation,

$$\eta = 1 - \exp\left(\frac{-Aw_e}{U}\right) \tag{2.1}$$

where η is particle concentration, U is the gas flow rate, A is the effective collection surface area, and w_e is the particle migration velocity. This equation assumes infinitely rapid mixing, a single

constant particle migration velocity and complete collection at the grounded collector plate (no re-entrainment). A number of studies have been performed to study the effect of lowered turbulence levels on precipitator efficiency. Two numerical studies began with the convective diffusion equation.

Leonard et al. (1980) arrived at an analytical solution to the diffusion equation but used a numerically calculated entrance flow profile. It was concluded that an improvement in gas flow quality could vastly improve the precipitator performance. Experimental work by Leonard et al. (1981) in a two stage bench scale precipitator demonstrated the validity of the diffusion models postulated earlier. Using a hot wire anemometer for turbulence measurements and an optical particle concentration measurement method, they showed that efficiencies improve with decreasing turbulence levels.

Feldman et al. (1977) began with an equation similar to that of Leonard et al. but then proceeded to solve for particle concentrations numerically using boundary conditions appropriate for simulating reentrainment and non-reentrainment conditions. By characterizing reentrainment as a ratio of diffusive to electrical migration forces, they concluded that as diffusive forces become large, reentrainment becomes significant and a loss in precipitator efficiency results.

More recent numerical work has been done by Larsen and Sorensen (1984). Larsen and Sorensen extended the work of Leonard and Feldman on the convective diffusion equation by examining the effects of secondary flows. They imposed an axial roll upon the bulk gas flow and concluded that there is a decrease in precipitator efficiency for an increase in roll strength.

It seems, then, that one could increase precipitator efficiency by reducing mixing through a reduction in the scale of turbulence and secondary flows. The majority of mixing within a flow is the result of large scale motions or circulations. Because surrounding geometry (both physical and electrical in the case of precipitators) plays a large role in the creation of such motions, one must turn to geometry in order to control them. Shaughnessy et al. (1985) and Davidson and Shaughnessy (1986) have postulated that an effective method of reducing the scale of corona turbulence and secondary flows would be to redesign the discharge electrode so as to produce a more uniform electric field.

2.3 Electrohydrodynamic Theory

An examination of the equations governing particle free gas flows developed by Davidson and Shaughnessy (1986) points to electrode geometry as a critical factor in controlling electrically induced flows. Before attempting to select a more suitable electrode geometry one must first examine the appropriate electrohydrodynamic equations.

The set of electrodynamic equations used to couple the electrical effects to the fluid flow are a set of reduced Maxwell equations:

$$\epsilon \frac{\partial E_i}{\partial x_i} = \rho_c , \tag{2.2}$$

$$E_i = - \frac{\partial \phi}{\partial x_i} , \tag{2.3}$$

$$\frac{\partial J_i}{\partial x_i} = 0 , \tag{2.4}$$

and Ohm's law:

$$J_i = \beta |\rho_c| E_i \ , \tag{2.5}$$

where ϵ is the gas permitivity, E_i is the electric field strength, ρ_c is the space charge density, ϕ is the electric potential, J_i is the current density, and β is the ion mobility. The applicable fluid mechanics equations are the incompressible continuity equation:

$$\frac{\partial u_i}{\partial x_i} = 0 \tag{2.6}$$

and the Navier-Stokes equation with an electric body force term included:

$$\rho \left[\frac{\partial u_i}{\partial t} + u_j \frac{\partial u_i}{\partial x_j} \right] = - \frac{\partial P}{\partial x_i} + \mu \frac{\partial^2 u_i}{\partial x_i^2} + \rho_c E_i , \tag{2.7}$$

where u_i is the instantaneous fluid velocity, ρ is the density, P is the pressure, and μ is the absolute viscosity.

Davidson and Shaughnessey (1986) have shown that the body force term, $\rho_c E_i$, may be represented by J_i/β and broken up into its rotational and irrotational components by expressing the current density, J_i, as the sum of a scalar and vector potential. The irrotational component may then be combined with the pressure term in the Navier-Stokes equation to create a modified pressure, leaving the rotational portion of the electric body force term to be examined independently.

They go on to show that the curl of the electric body force can be written as:

$$\frac{1}{\beta} \epsilon_{ijk} \frac{\partial J_k}{\partial x_j} = \epsilon_{ijk} \frac{\partial \rho_c}{\partial x_j} E_k \tag{2.8}$$

by taking the curl of equation (2.5) and using equation (2.3). Thus, the only situations in which the electric body force is irrotational occur when the ionic space charge, ρ_c, is uniform or when the electric field lines are everywhere normal to contours of constant space charge density. Flippen (1982) has shown that the latter is true only for three cases; concentric spheres, concentric cylinders, and parallel plates. Clearly, the electric body force in the wire-plate precipitator is rotational and as a result electric flow disturbances exist.

Nondimensionalization of the Navier-Stokes equation (2.7) is used to estimate the relative magnitude of the electric body force and thus flow modifications. Using the parameters I, A, U, and L to represent total current, plate area, bulk gas speed, and plate separation, the dimensionless equation of motion is as follows:

$$\frac{\partial u_i}{\partial t} + u_j \frac{\partial u_i}{\partial x_j} = - \frac{\partial P}{\partial x_i} + \frac{1}{Re} \frac{\partial^2 u_i}{\partial x_j^2} + F J_i \tag{2.9}$$

The nondimensionalization procedure is presented in Appendix B. The dimensionless electric number, F, is the ratio of the electric body force to the inertial force and is written as

$$F = \left[\frac{IL/\beta A}{\rho U^2}\right] \tag{2.10}$$

Using values from Table 2.1 representative of a typical commercial wire-plate precipitator, values of F = 0.87 and Re = 4310 are obtained for estimates of the electric and Reynolds numbers, respectively. These values indicate that there is a strong electrical influence on the flow.

In light of the above electrohydrodynamic discussion, it seems reasonable to select one of the three special geometries discussed by Flippen as a basis for the redesign of the discharge electrode. A parallel plate design is selected due to its ability to handle larger volumes of gas than the concentric cylinder geometry and because it is easily adapted from the wire-plate design. The only drawback is that a corona discharge on a flat plate is physically impossible. To remedy this situation an array of sharp protrusions are placed at equally spaced intervals throughout the face of the discharge plate, thereby creating a uniform pattern of corona tufts and an electric field approximating that of the parallel plate geometry.

This design does not produce a uniform discharge but does reduce the scale of the electrical nonuniformity within the precipitator flow channel. Figure 2.2 is a sketch of the barbed plate electrode design. The flow from such a design is envisioned as closely spaced corona wind jets originating from the individual barbs. An illustration of the conceptual secondary flows set up by such a geometry, as opposed to a wire-plate geometry, is shown in Figure 2.3. Although such an electrode design does not eliminate electrohydrodynamic flow disturbances, it does offer the possibility of reducing the scale of

Table 2.1. Industrial Electrostatic Precipitator Characteristics

	Text Values*	General Electric+	Flakt+
Plate Spacing (cm)	20-38	23-31	30-40
Aspect Ratio (ht./wd.)	30-60	20-50	34-45
Wire Diameter (mm)	2.75-6.4	3-4.75	2.5
Wire Spacing (cm)	10-35	20-25	23
Gas Flow rate (m/sec)	.75-4.5	0.9 -1.52	1.4
Current Density (mA/m^2)	.1-1	0.05-0.3	0.5-0.7
Sparkover (kV)	40-65		
Temperature (°C)	100-480	138-166	149-204
Pressure (atm)	1	1	1
Operating Voltage (kV)	40-65	35-55	55-75

*Assimilated from White (1963), Oglesby and Nichols (1978), and McDonald and Dean (1982).

+Based on telephone conversation with the manufacturer.

General Electric Environmental Services, Inc.
200 N. 7th St., Lebanon, PA 17042

Flakt, Inc., Air Pollution Control Group
P.O. Box 59018, Knoxville, TN 37950

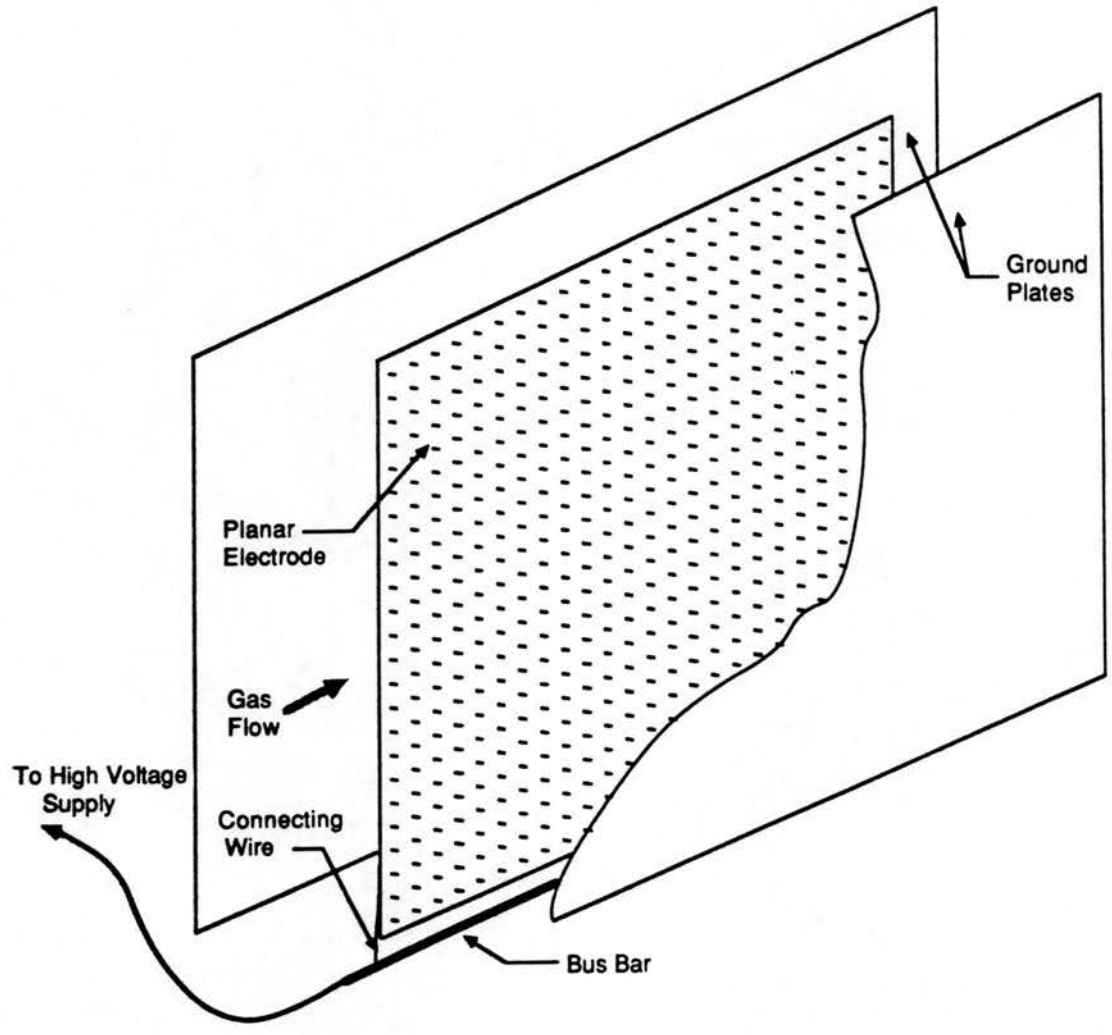

Figure 2.2. Barbed plate electrostatic precipitator.

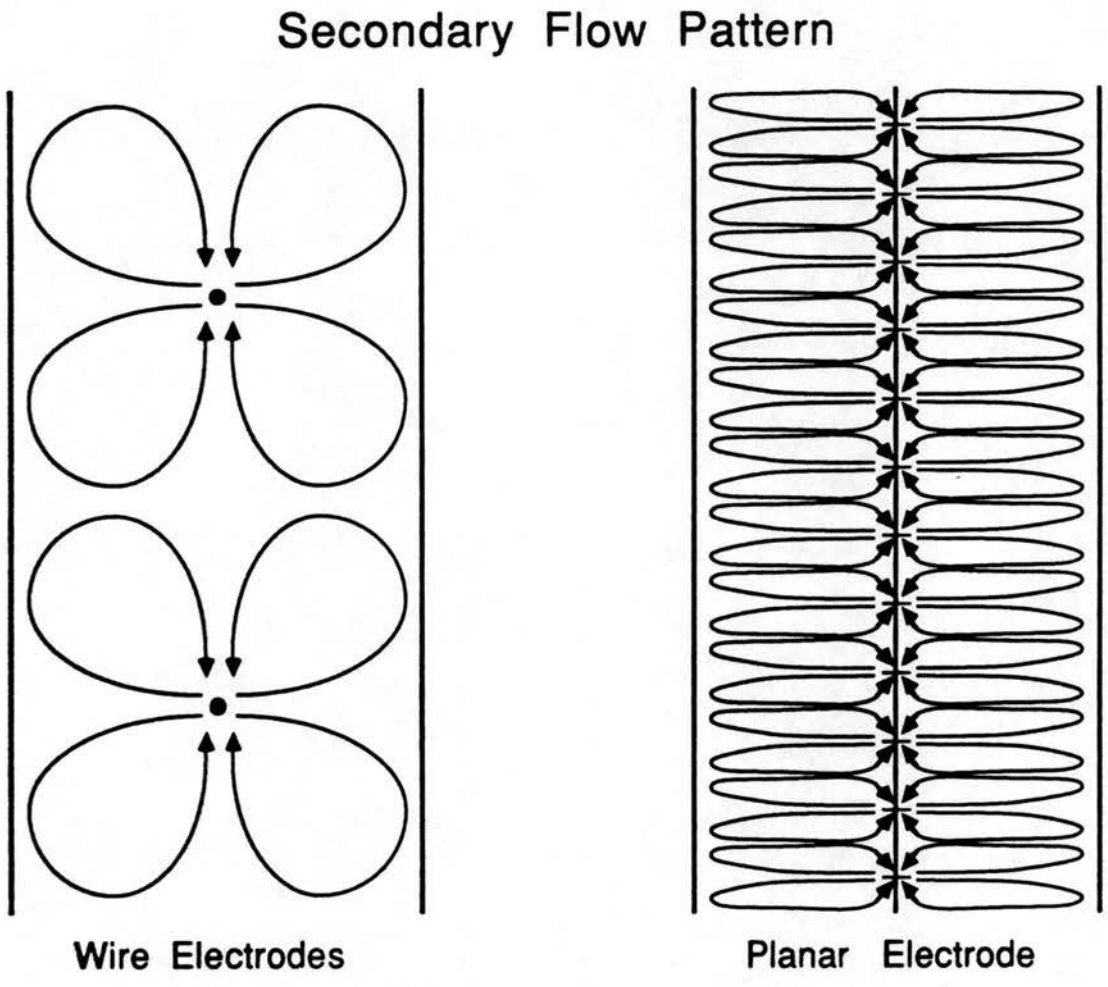

Figure 2.3. Conceptual sketch of EHD flow.

the electrically generated secondary flow and turbulence. The electrical inhomogeneity is on the order of the barb to barb spacing which is substantially less than the nonuniformities in the wire plate design which are on the order of the wire to wire spacing.

The concept of using a barbed plate electrode in a precipitator is not a new idea. A number of U.S. and foreign patents have been obtained for planar electrodes. U.S. patent holders include Bridge (1906), Fortescue (1922), Shively and Harlow (1940), Steuernagel (1969), Blier (1971), and Robertson (1974). None of the patents, however, cite fluid properties as a basis for the new electrode design.

CHAPTER 3

EXPERIMENTAL FACILITY AND METHODS

The primary purpose of these experiments is to assess whether or not the electrically induced gas flow in electrostatic precipitators can be controlled through the use of a novel planar electrode. A wind tunnel test section enclosing a small precipitator model is designed specifically to measure the electrohydrodynamic flow in both a standard wire-plate precipitator and a plate-plate precipitator. Experiments to determine the magnitude and structure of the electrically induced turbulent flow are carried out using a variety of planar electrodes. These measurements are then compared to those of a standard wire-plate geometry.

Measurement of the velocity field in the vicinity of the high electric field of a corona discharge is difficult. Laser Doppler anemometer measurements are not accurate in the presence of the electric field since velocity measurements are made by using "seed" particles within the flow field. This presents a problem in an electrostatic precipitator because the particles become charged and do not move with the same velocity as the gas. Using a hot-film anemometer within the high electric field region is impossible for two reasons. First, if the grounded probe support is placed nearer to the electrodes than the collector plates, the field will be oriented toward the probe support. Second, if the probe assembly is placed in a region of high electric field, the probe itself will develop a

corona discharge and anomalous velocities and velocity readings will result. Placing a hot-film anemometer probe downstream of the high voltage area is a viable solution. The probe must be located far enough downstream so that the presence of the electric field does not cause anomalous velocities. In these experiments, the hot film probe is located at least 46 cm (18 in.) downstream of the precipitator electrode to avoid electric field effects.

The experiments are performed at room temperature and pressure (approximately 21.1 degrees Celsius and 87.1 kPa, respectively). Using particle-free air, gas flow measurements are obtained for mean flow speeds of 0.5, 1.0, and 2.0 m/sec, and negative electric current levels up to 5.3 mA.

Time series streamwise velocity data are taken at several cross-stream locations downstream of the precipitator test section. The amplitude content of the turbulent flow field is examined by computing the mean velocity, turbulence intensity, and probability density function (PDF). Information on the structure and frequency content of the EHD induced turbulence is obtained through spectral analysis, including the evaluation of an integral length scale.

3.1 EHD Wind Tunnel

The experimental studies for this project are performed at Colorado State University in the EHD wind tunnel facility in the Fluid Dynamics and Diffusion Laboratory (FDDL) shown in Figure 3.1.

The EHD wind tunnel, shown in Figure 3.2, is a vertical loop tunnel which can be operated as a closed loop tunnel or may be configured to allow air to enter from and exit to the exterior atmosphere. The 122 cm (48 in.) diameter vaneaxial fan is manufactured

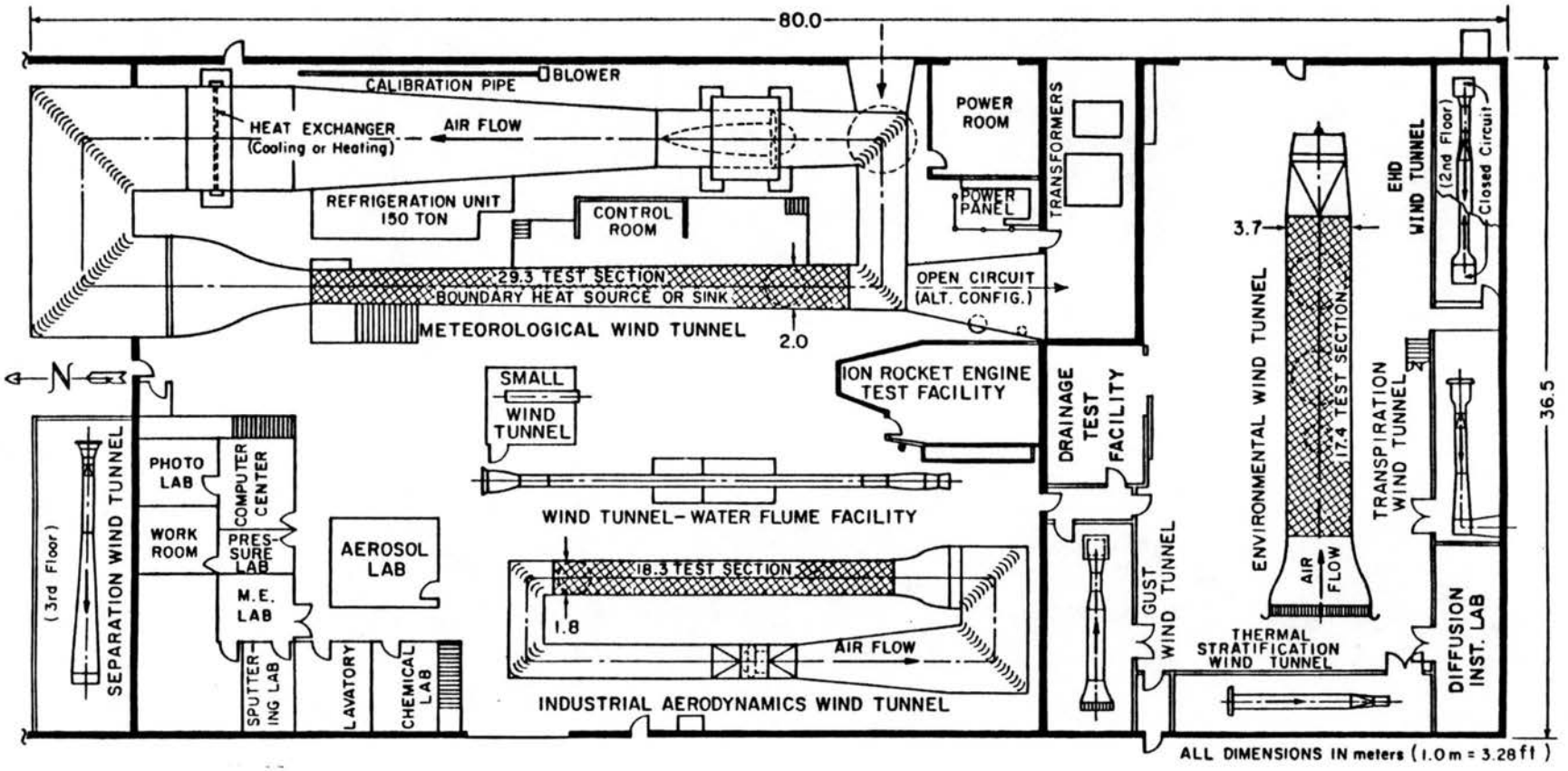

Figure 3.1. Fluid Dynamics and Diffusion Laboratory at Colorado State University.

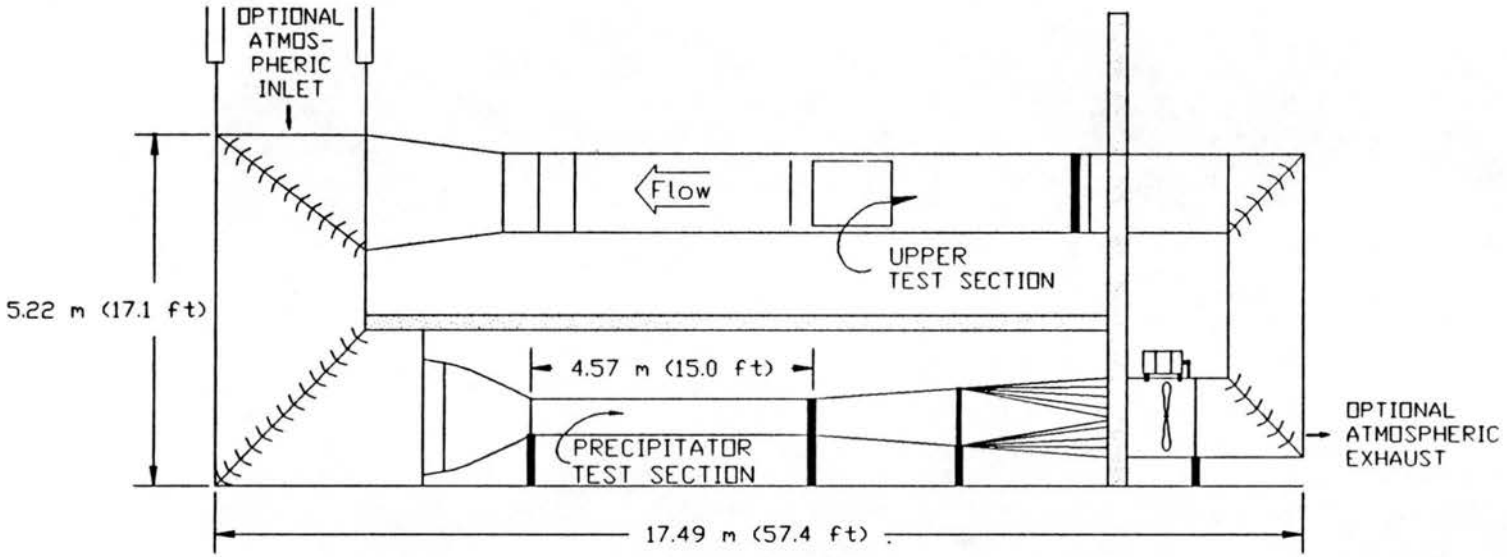

Cross - Sectional View of EHD
Vertical Loop Wind Tunnel

Figure 3.2. EHD wind tunnel.

by the Buffalo Forge Company (490 Broadway, Buffalo, NY 14204). The fan is controlled by a Louis Allis (16555 W. Ryerson Road, New Berlin, WI 53151) Saber 3300 3-phase, non-regenerative, DC static drive. The motor itself is a Louis-Allis Flexitoro 20 H.P. type GPNR motor (model 718336G001).

The tunnel has two test sections, one in the upper portion of the loop and the other in the lower. The upper test section is 122 cm (48 in.) square and 9.8 meters (32 ft) in length. The lower section is 61 cm (2 ft) square and is 4.6 meters (15 ft) in length. There is a smooth contraction preceding the lower test section and a divergence following it to bring the tunnel diameter to 122 cm (48 in.) at the fan. The fan and controller system are capable of providing velocities from 0 to 52 m/sec in the lower test section.

The model precipitator test channel is built into the lower test section as shown in Figure 3.3. Air enters the channel through a 29.2 cm (11.5 in.) deep 61 cm (24 in.) square Astrocel Superinterception absolute air filter manufactured by American Air Filter (215 Central Avenue, Louisville, Kentucky 40208). The filter serves as a flow straightener and provides a large pressure drop, thus allowing better flow control at low flow speeds. At the filter exit, a contraction reduces the 61 cm (24 in.) square cross section to a rectangular section 61 cm (24 in.) high and 15.25 cm (6 in.) wide.

The 61 cm (24 in.) by 15.25 cm (6 in.) test channel is constructed of ten removable panels to facilitate tunnel entry and electrode replacement and modification. The panels are constructed of standard 2 by 4 lumber frames (5 cm by 10 cm) which support 2 cm (3/4 in.) thick plywood and/or Plexiglas panels which form the wall of the flow channel. Each panel is bolted to both the floor and the roof

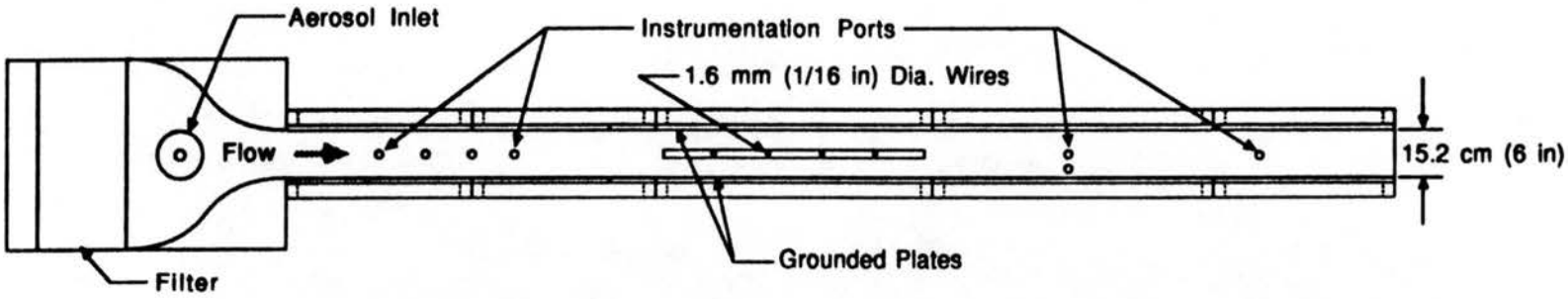

Top View

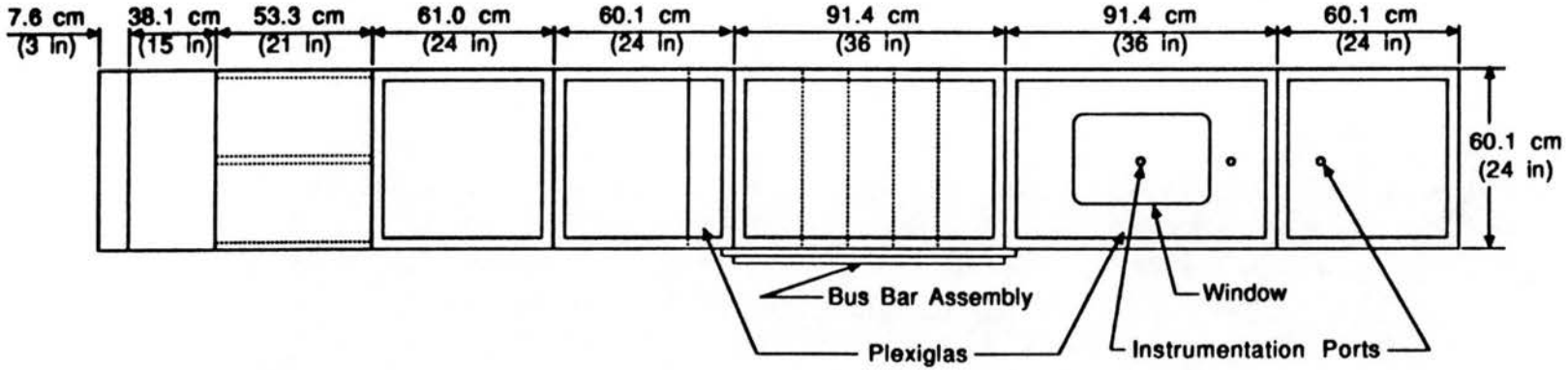

Side View

Figure 3.3. Model precipitator test section.

of the tunnel. One Plexiglas panel contains a 30.5 km by 45.7 cm (12 in. by 18 in.) access window to permit easy access to the tunnel. Instrumentation ports are located on several of the panels. A special set of panels enclose the active precipitator section. Two collector plates are constructed of plywood laminated with 1.0 mm (0.04 in.) thick galvanized steel using contact cement. A third panel is fabricated completely of Plexiglas and supports a planar electrode in one planar electrode geometry. Following the test channel, two pieces of flat plywood are placed in the tunnel at an angle of approximately 15 degrees to make a smooth transition back into the tunnel divergence.

Instrumentation ports are provided on top of the tunnel at four locations forward of the test section, and on the top, bottom, and side of the tunnel at a distance 45.7 cm (18 in.) downstream of the test section. Additional ports are provided on the side of the tunnel at distances of 76.2 cm (30 in.) and 106.7 cm (42 in.) downstream of the test section. Each port is a hole threaded to accommodate a probe support mount (TSI part # 1138-1). A 45.7 cm (18 in.) probe support is inserted in the mount, which contains a finger tightened set screw. The probe is traversed through the mount, using the set screw to hold it in place at the desired location.

3.2 Wire-Plate Precipitator Test Section

The wire-plate configuration is shown in Figure 3.4. The collector plates are electrically grounded to a common ground on the electrical "low side" of the power supply by 2 cm (3/4 in.) wide braided tinned copper cable. The discharge wires are mounted vertically along the centerline of the tunnel, between the plates.

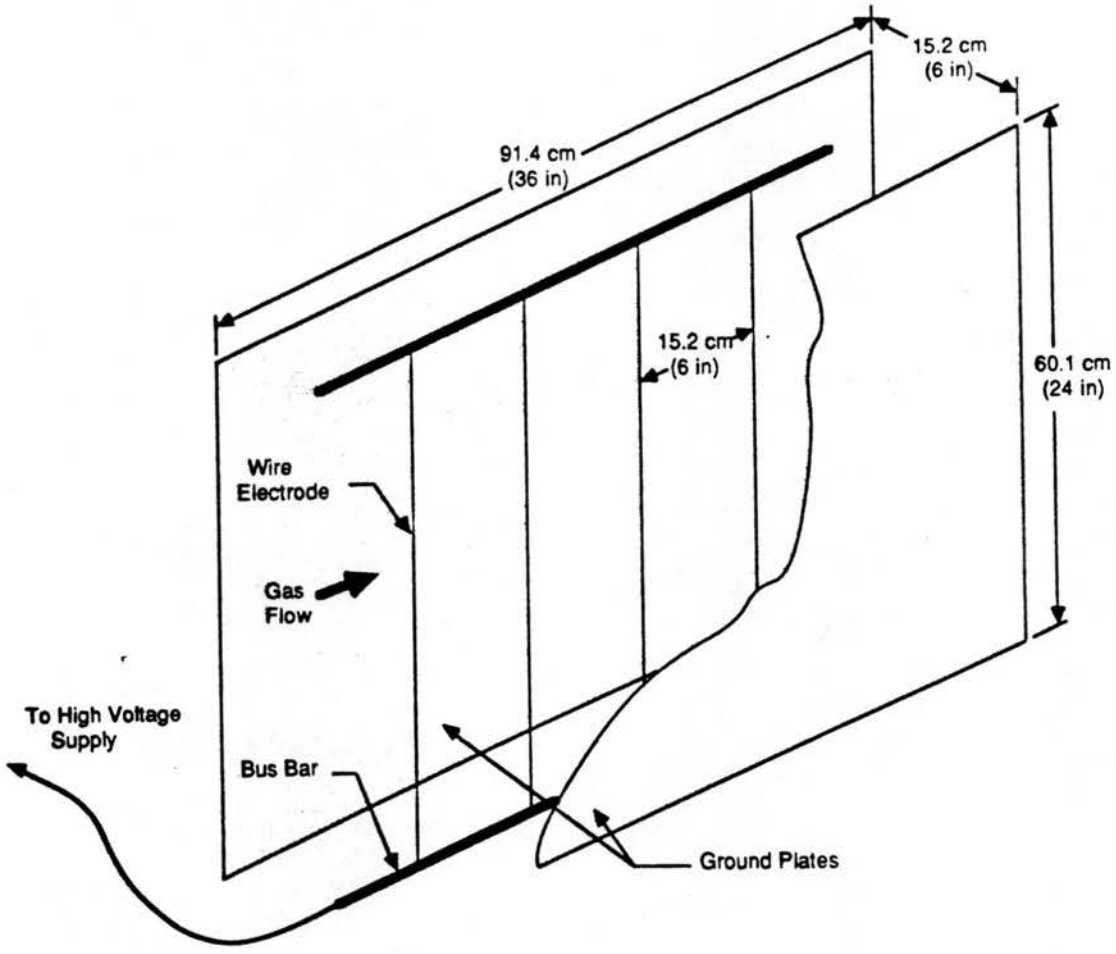

Figure 3.4. Wire-plate precipitator test section.

Nine mounting holes are provided in the floor and the ceiling of the tunnel at 7.62 cm (3 in.) intervals to accommodate a variety of wire to wire spacings. The wires used in this study are 1.6 mm (1/16 in.) diameter stainless steel rods. To model the wire-plate design, a single configuration of four wires at 15.2 cm (6 in.) intervals is used.

High voltage is supplied to the wires by means of a "bus bar" mounted in the floor of the tunnel. The wires are connected to the bus bar using set screws to hold them into specially drilled holes. Small holes are drilled through the tunnel floor to permit the wire electrodes to be attached to the bus bar. Similar holes are drilled through the 1 cm (3/8 in.) thick Plexiglas tunnel ceiling to allow the electrodes to be secured to a plastic bar. The bus bar and wire electrodes are electrically isolated from the rest of the tunnel (and ground) by using slabs of 2 cm (3/4 in.) thick Plexiglas for the tunnel construction surrounding the high voltage area.

3.3 Plate Geometry

Two basic precipitator geometry configurations are used for the planar electrodes. In the half-channel electrode configuration, shown in Figure 3.5, the planar electrode is mounted in the center of the test channel parallel to the collector plates. Electrical power is supplied by running a small wire between the electrode and the bus bar. Thin plastic walls are extended upstream and downstream a distance of 61 cm (24 in.) to alleviate plate edge effects and to correctly model a full-scale retrofit application. Effectively, the high voltage plate electrode replaces the wires in the conventional design.

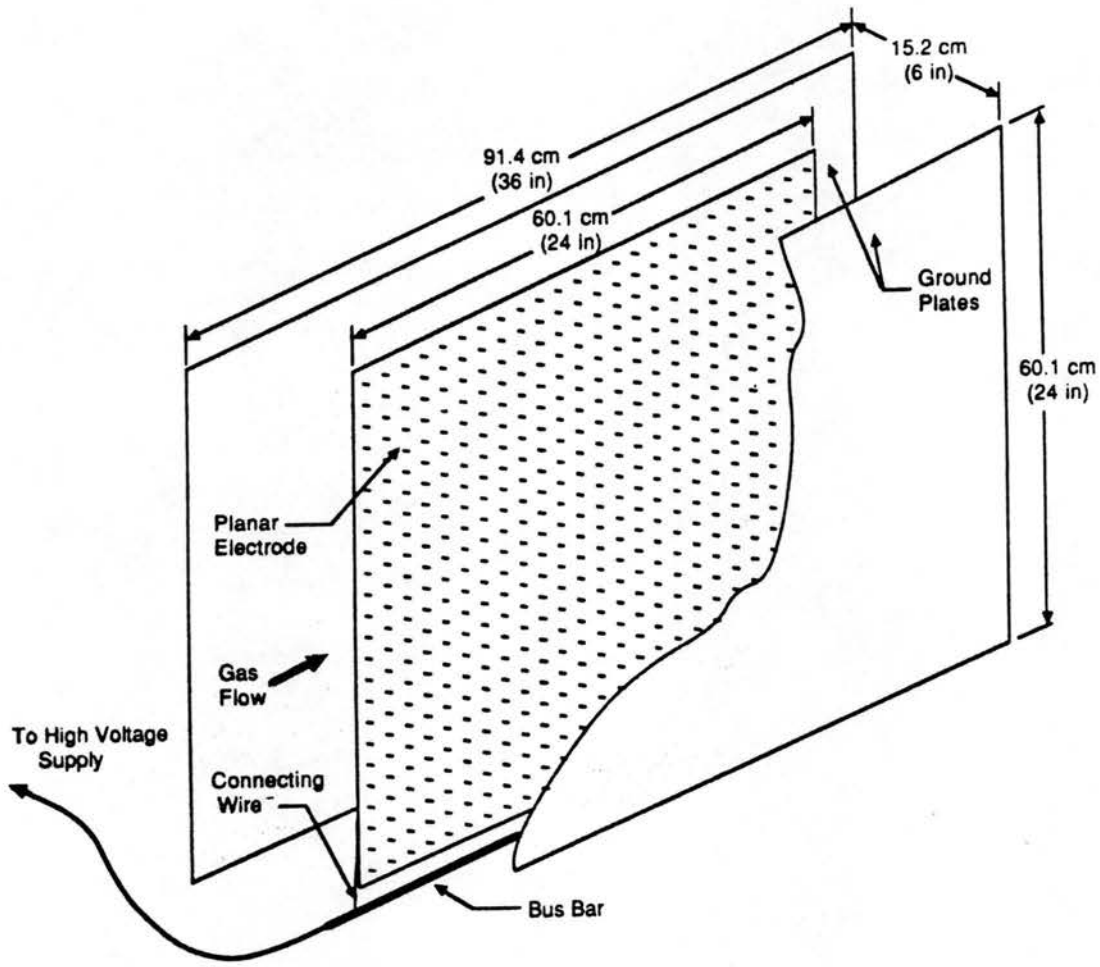

Figure 3.5. Half-channel barbed plate precipitator.

In the full-channel electrode configuration illustrated in Figure 3.6, the planar electrode is mounted on one side of the test section channel and a ground plate on the other. In retrofit applications, this design requires removal of the wires and replacement of alternate collector plates with the barbed plate electrode. A new wall panel, made entirely out of 2 cm (3/4 in.) thick Plexiglas, is installed on the electrode side of the tunnel to provide adequate insulation. The planer electrode is affixed to the Plexiglas wall using clear plastic tape to facilitate replacement and modification of the electrode. The high voltage power is supplied to the rear of the electrode though a small opening in the Plexiglas wall.

Four types of planar electrode configurations are studied in this experiment. Plate A is constructed of two aluminum plates 61 cm (24 in.) square and 1.3 mm (0.05 in.) thick. Barbs made of thumb tacks are aligned at 2.5 cm (1.0 in.) square intervals, as shown in Figure 3.7, resulting in a total of 576 raised points per side. The tacks are 1 mm (0.04 in.) wide and protrude 5 mm (0.2 in.) through pre-drilled holes in each plate. The plates are riveted together in five places so that the tack heads are back to back and the points protrude outward. Plate B is similar to plate A but utilizes only one aluminum plate. Steel rods are inserted through drilled holes in the offset configuration, shown in Figure 3.7, resulting in a total of 572 points per side at 2.7 cm (1.0625 in.) intervals. The rods are 0.9 mm (0.035 in.) in diameter and protrude 3.5 mm (0.14 in.) from each side of the plate. Plate C is identical to plate B but with twice as many points. Plates A, B, and C are each mounted in the center of the channel, effectively replacing the wires and thus creating the half-channel configuration discussed above. Plate D is one side of the

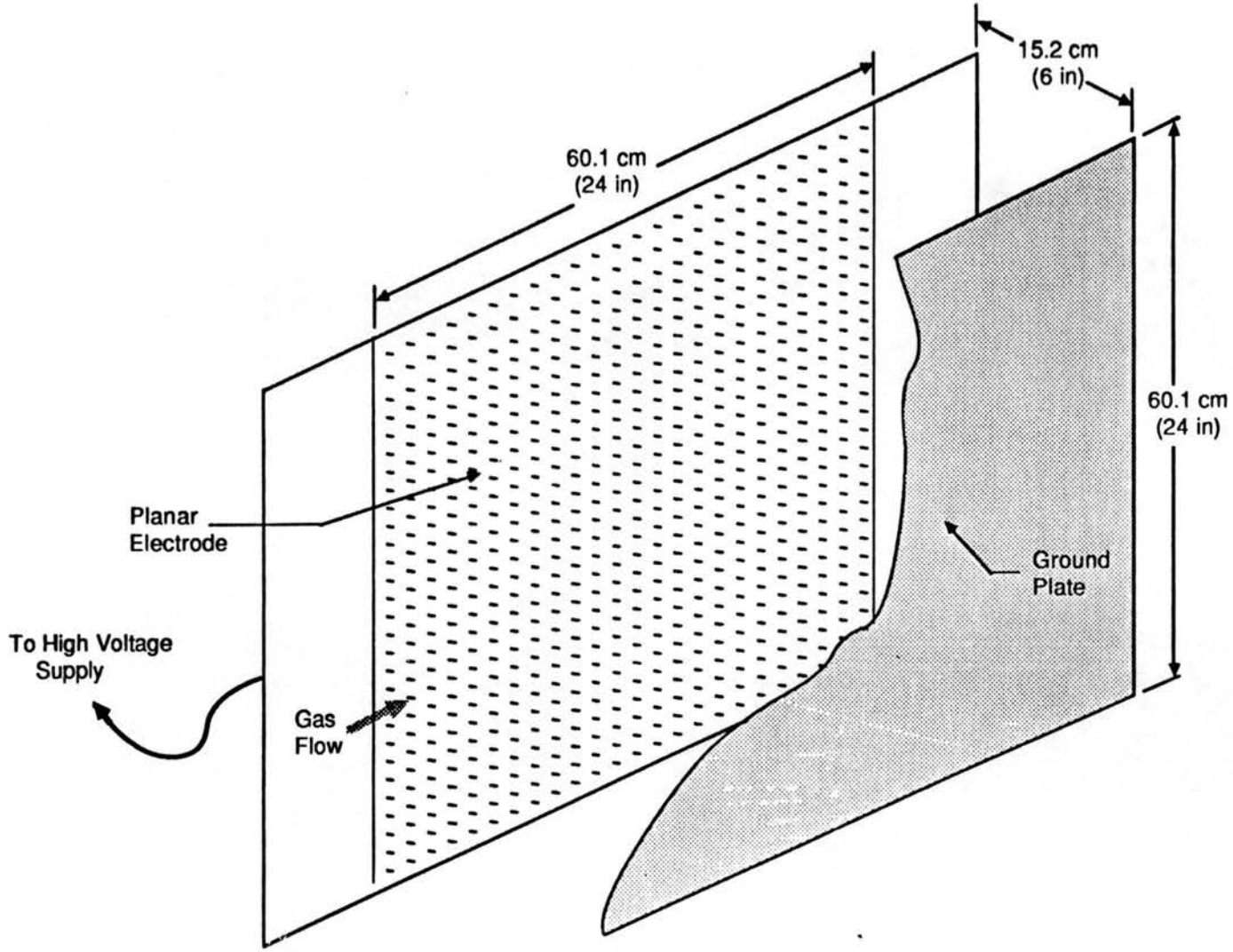

Figure 3.6. Full-channel barbed plate precipitator.

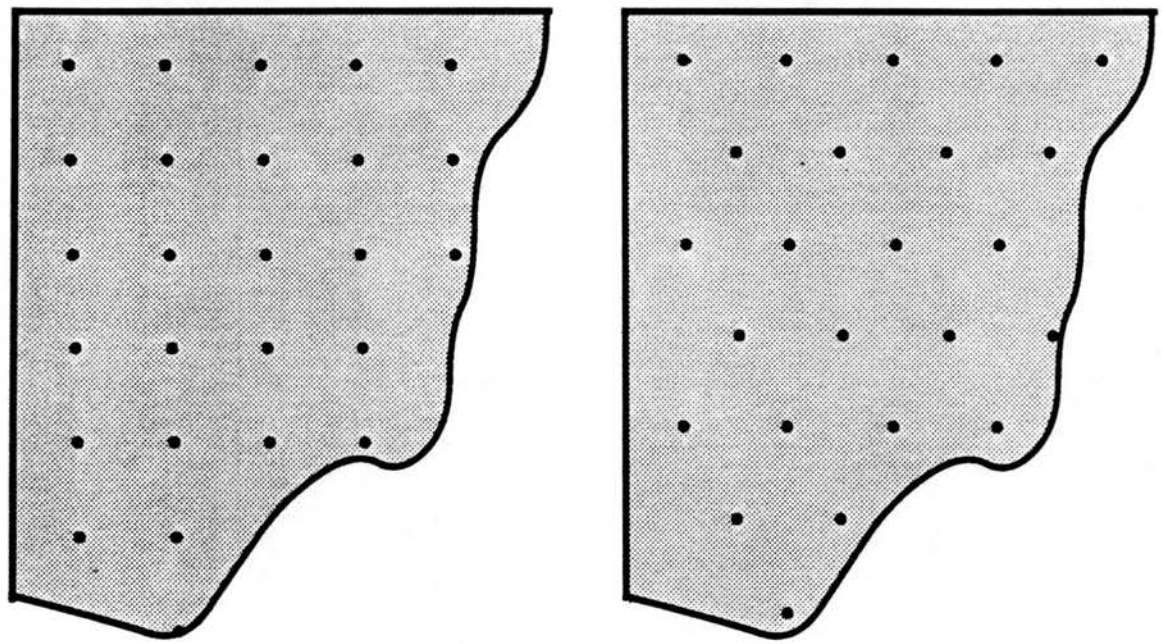

Figure 3.7. Barb patterns.

plate A electrode and is used in the full-channel electrode configuration.

3.4 Instrumentation

3.4.1 High Voltage Equipment

High voltage for the precipitator model is provided by a Hipotronics Inc. (Route 22, P.O Drawer A, Brewster, NY 10509) model 875-13 DC power supply. The 1000 watt power supply can be operated at three maximum power levels, 75 kV at 13 mA, 60 kV at 16 mA, or 50 kV at 20 mA. Triple range analog meters are included for monitoring current and voltage levels. Other features include reversible polarity, a line reactor to enable continuous operation when sparkover occurs, and a 2% maximum rms ripple. In these experiments the power supply is operated in the negative polarity configuration only.

3.4.2 Flow Measurement Equipment

Hot-film anemometry is used to obtain time series velocity data. The data acquisition configuration is illustrated in Figure 3.8. The Thermo Systems Inc. (TSI) (500 Cardigan Road, P.O. Box 64394 St. Paul, MN 55164) 1050 anemometer is a constant temperature hot wire/hot film anemometer. Included in the anemometer unit is a TSI 1057 signal conditioner with both high and low pass filters with a rolloff of 12 dB/octave. The 1057 also has a zero suppression circuit with a range of 0 to 29 volts and an output amplifier capable of a gain of 10 or 100. TSI type 1210 hot film probes are used exclusively in this study.

Equipment used to monitor the hot film signal include a Tektronix Inc. (P.O. Box 500, Beaverton, Oregon 97077) model T932A 35 MHz 2

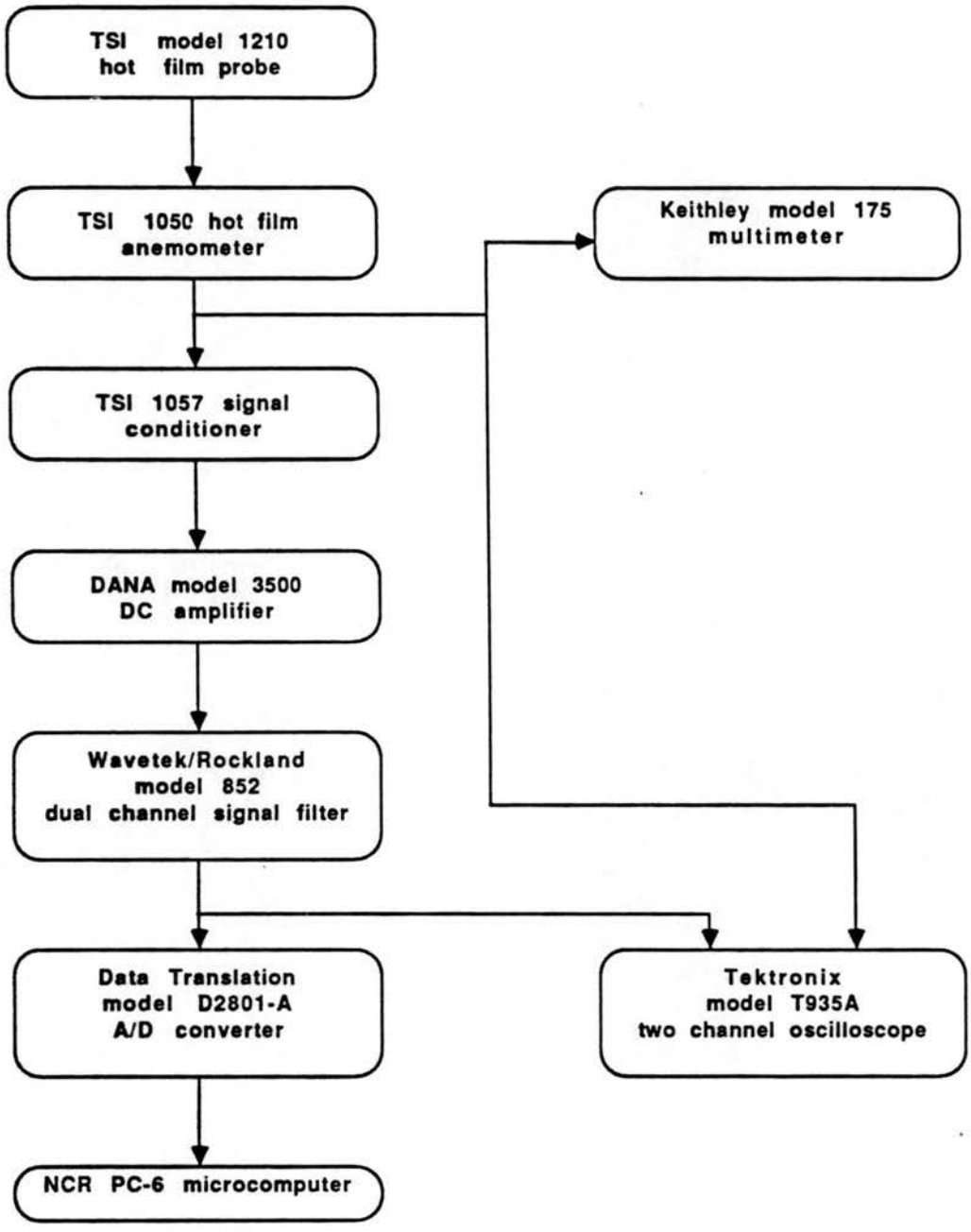

Figure 3.8. Data acquisition system.

channel oscilloscope and a Keithly Instruments, Inc. (28775 Aurora Road, Cleveland, Ohio 44139) model 175 autoranging multimeter. Signal conditioning is achieved with the TSI 1057 signal conditioner as well as Dana model 3500 DC amplifier and a Wavetek/Rockland model 852 dual channel signal filter, with roll-off characteristics of 48 dB/octave per channel. The output of the anemometer bridge is passed internally to the model 1057 signal conditioner where the signal is DC suppressed to obtain an output signal remaining in the range of 0.0 to 0.5 volts. This DC offset is usually approximately 2.5 volts but depends upon both the specific hot film being used and the mean flow. The suppressed signal is then amplified by a factor of 20 by the DANA amplifier and then low-pass filtered at 200 Hz using the Wavetek filter. A roll-off of 96 dB per octave is achieved by passing the signal through each of the filter's two channels in series. The signal is sampled and converted to digital form at a rate of 400 Hz.

The hot film probes are calibrated with the steady flow of a TSI model 1125 calibrator. The calibration pressures are measured with a Datametrics (340 Fordham Road, Wilmington, MA 01887) type C-1018 electric manometer. The manometer consists of a Datametrics 0 - 10 torr barocel pressure sensor with a type 525 thermal base and a Newport Laboratories (Santa Ana, CA) series 2000B/SER digital power meter built in to the unit. Calibration points are acquired and analyzed with a computerized data acquisition system. The software, HWCAL, is described in Appendix A. The barocel voltage output and the hot film anemometer bridge output are each sampled 100 times over a 2 second interval and averaged to obtain a single calibration point. An equipment schematic for evaluation is shown in Figure 3.9.

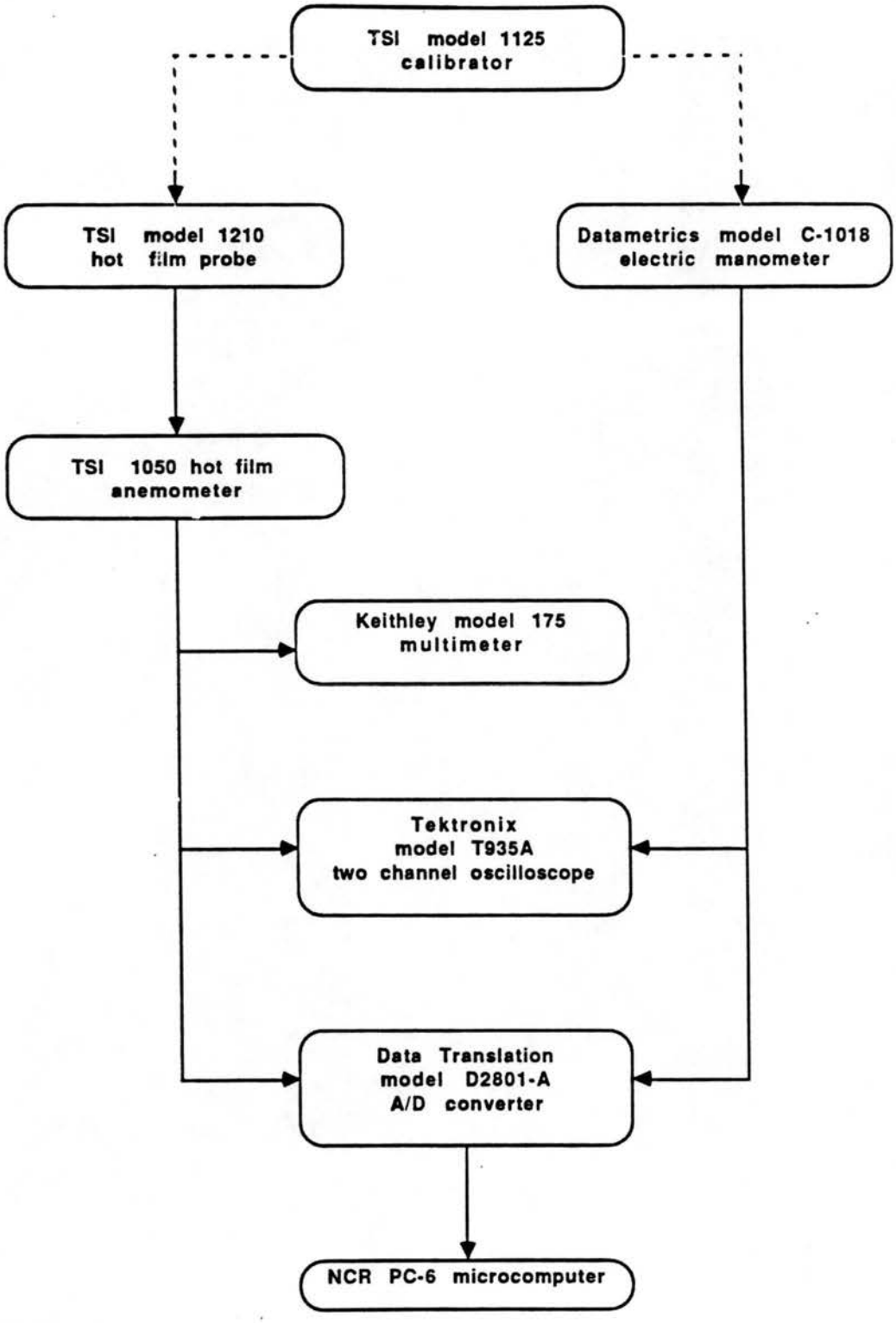

Figure 3.9. Hot-film calibration flow chart.

Velocity is computed from the pressure using Bernoulli's equation,

$$\frac{P_1}{\gamma} + \frac{V_1^2}{2g} + z_1 = \frac{P_2}{\gamma} + \frac{V_2^2}{2g} + z_2 \ , \qquad (3.1)$$

where P is fluid pressure, V is velocity, γ is specific weight, g is the gravitational acceleration and z is the elevation. Adjustments are made for the area ratios in the calibrator. Atmospheric pressure and temperature are assumed constant at 87.1 kPa and 21.1 degrees Celcius respectively. A 4th order polynomial curve fit of the calibration data, using a least squares method, is used to obtain an equation for gas velocity in terms of anemometer bridge voltage. A typical calibration plot along with the computed coefficients is shown in Figure 3.10. Once calculated, the coefficients of the calibration equation are saved for use by the data analysis programs.

Signal digitizing is accomplished with an NCR (Dayton, Ohio 45479) PC-6 microcomputer (IBM PC/XT compatible) equipped with a 20 megabyte fixed disk and a Data Translation (100 Locke Drive, Marlborough, MA 01752) model D2801-A 16 channel analog and digital I/O system add-on board (up to 27,500 conversions per second in DMA mode). A Hercules color graphics adapter card (CGA standard) is also added to the system in order to run the software needed to gather the data. The program, TURBDATA, described in Appendix A, is used to acquire and analyze all data.

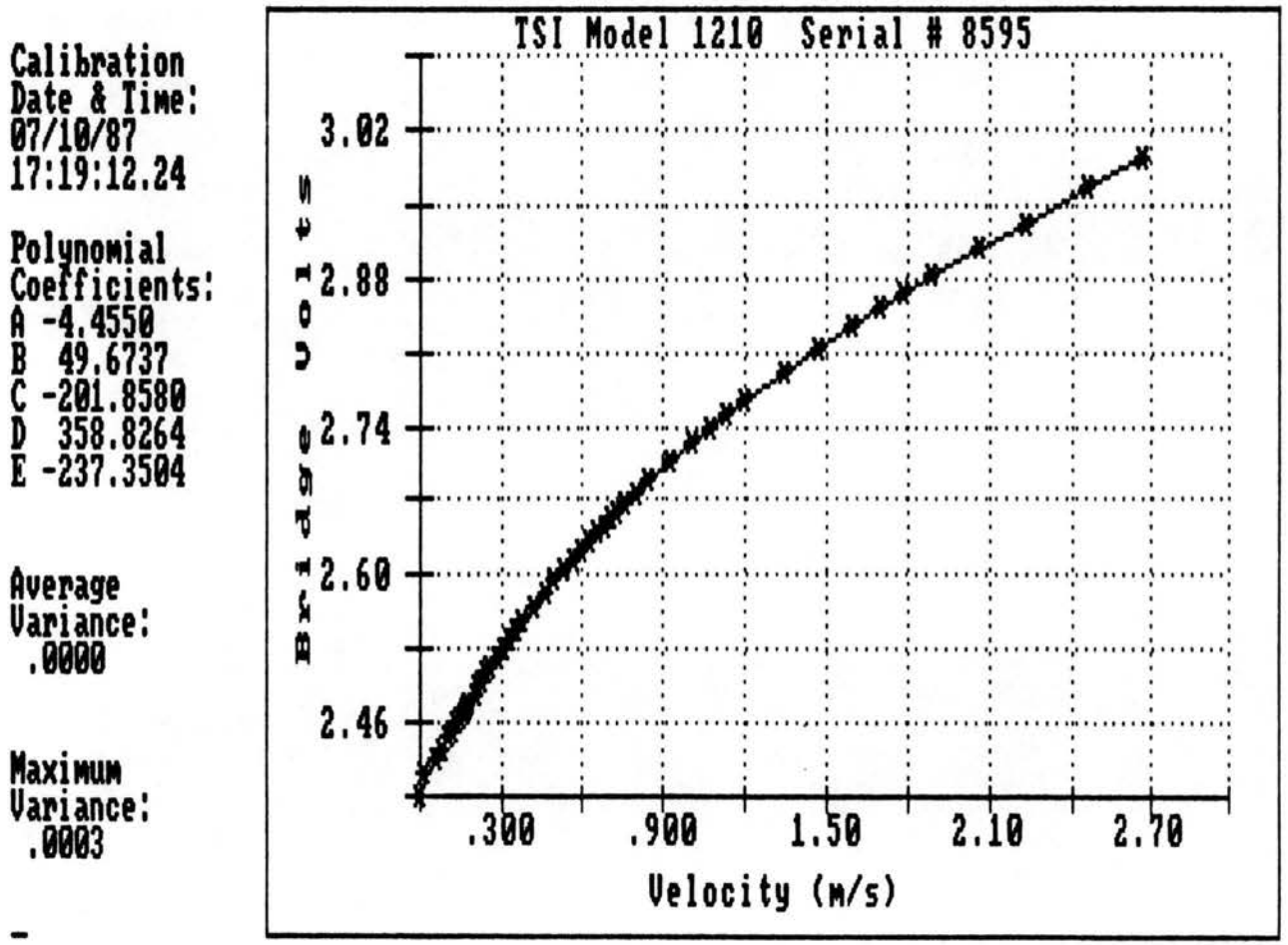

Figure 3.10. Hot-film calibration plot.

3.4.3 Flow Visualization Equipment

Visualization of the flow within the precipitator test section is accomplished by using a laser light sheet to illuminate a plane of smoke introduced into the upstream channel. The laser light sheet is created by directing a Spectra Physics (1250 West Middlefield Road, Mt. View, CA 94042) Stabilite Model 124A 35 mW Helium-Neon laser through a quartz or pyrex glass rod. The laser is powered by a Spectra Physics Model 225 Laser Excitor. An aerosol was generated using a Rosco (Port Chester, New York, 10573) Model 8215 Fog/Smoke Machine and piped into the aerosol inlet upstream of the active precipitator. Smoke was also created by dipping a cotton-tipped applicator into titanium tetrachloride (Fisher Scientific Company, Chemical Manufacturing Division, Fair Lawn, NJ, 07410) and inserting it into an upstream instrumentation port. A professional quality 3/4 inch video film of the flow visualization is made.

3.5 Data Acquisition and Analysis

3.5.1 Hot Film Measurements Near Corona Discharge

The introduction to this chapter mentions the selection of the hot film probe for velocity measurements and states that the probe must be placed an "adequate" distance from the corona discharge. Anomalous velocities may be created by a corona discharge from the probe itself, known as probe leakage. Davidson (1984) and Kumaran et al. (1983) have both studied this effect in laboratory precipitators, with Kumaran citing a necessary probe to electrode distance of 56 cm and Davidson reporting 46 cm to eliminate leakage. Several tests similar to those conducted by Davidson are undertaken in this study to check for probe leakage. In the half-channel electrode

configuration, a Keithley model 614 pico-ammeter is connected to the probe to check for leakage current. With the probe placed 46 cm (18 in.) upstream of the precipitator test section, high voltages up to 60 kV are applied to the wire electrodes. At 60 kV, the current leakage is on the order of $1E^{-7}$ Amps. This is considerably lower than the 1.25 μA reported by Davidson to cause anomalous velocities. The fact that this low leakage is insignificant is confirmed by using the hot film to obtain mean and root mean square measurements of the flow 46 cm upstream of the precipitator. No significant variations in either of these two properties are observed when the high voltage is introduced. The measurements are taken upstream of the precipitator in order to avoid the corona generated turbulence that is swept downstream.

Probe leakage is also measured in the full-channel electrode configuration. In this configuration, the probe must be placed at least 106.7 cm (42 in.) downstream of the active precipitator section to avoid anomalous velocities.

3.5.2 Mean Velocity and Turbulence Intensity Profiles

Streamwise mean velocity and turbulence intensity profiles are measured in both the horizontal and vertical directions. Horizontal profiles are obtained by traversing the hot film probe from ground plate to ground plate at the vertical center. The probe is traversed manually, in 1.0 cm increments, using a scale mounted directly beneath the probe support as a reference. A 90 degree elbow (TSI part # 1125) is used to orient the probe correctly.

Each data point is obtained from a 4096 sampling sweep with 15 ms digitization intervals yielding a 61 second sampling span. The mean

velocity, U, for a given point is the arithmetic average of the instantaneous velocities (u_i),

$$U = \frac{1}{N} \sum_{i=1}^{N} u_i \ . \tag{3.2}$$

Turbulence intensity (I) is defined as the percentage ratio of the root mean square (rms) velocity to the mean velocity where,

$$u_{rms} = \frac{1}{N} \left[\sum_{i=1}^{N} (u_i - U)^2 \right]^{1/2} \tag{3.3}$$

and

$$I(\%) = \frac{u_{rms}}{U} (100). \tag{3.4}$$

where u is the local mean velocity.

Vertical profiles are acquired in a similar manner but measurements are taken at 5.0 cm increments from the ceiling to the floor of the tunnel. Also, due to the fact that the probe support is only 18 inches long, the top half of the vertical profiles are taken by mounting the probe support through the top of the tunnel, while the bottom half of the profile is obtained using a bottom mount.

3.5.3 Data Acquisition for PDF and Power Spectra

In order to achieve reasonably accurate power spectra and probability density functions from digital data, a fairly large time series of velocity data is needed. In determining the sampling

frequency, the concept of the Nyquist frequency or folding frequency as described in Bendat & Piersol (1971) is used. The Nyquist frequency is given as

$$f_c = \frac{1}{2h} \tag{3.5}$$

where h is the sampling interval. In order to obtain information at a given frequency, digital samples must be taken at a rate twice that frequency. As explained in Tennekes & Lumley (1972) frequencies in the spectrum of a flow can thought of as "eddies" of size $\lambda = U/f$, where U is the mean flow velocity and f is the frequency of interest. Thus the sampling frequency is determined by the smallest eddy of interest and the largest mean velocity. In this series of tests, the largest mean velocity used is 2.0 m/sec. The smallest point to point separation on an electrode is approximately 1.0 cm, making that the smallest eddy size of interest. This combination results in a frequency of 200 Hz and necessitates a sampling rate of 400 Hz.

Available computer memory makes record lengths greater than 16,384 points difficult to handle. Because of this, the number of samples digitized per sweep is 16,384. The instrumentation setup is the standard setup described in section 3.1.3. The hot film signal is low pass filtered at 200 Hz using the Wavetek filters. The typical digital sampling sweep used for the PDF and the power spectrum analyses consists of 16,384 points sampled at 2.5 ms intervals (400 Hz) resulting in a 41 second sweep.

3.5.4 Probability Density Functions

The probability density function (PDF) for a sample sweep is calculated using the algorithm of Bendat & Piersol (pp. 309-311). The instantaneous fluctuating velocity, u' is obtained by subtracting the mean velocity from each instantaneous velocity value. The PDF is then evaluated by:

$$p(u') = \lim_{\Delta u' \to 0} \left[\frac{\text{Prob. } [u' \leq u'(t) \leq u' + \Delta u']}{\Delta u'} \right] . \qquad (3.6)$$

Numerically, the following general technique is applied:

For **N** data samples with minimum velocity **a** and maximum velocity **b**, an interval width **W** is defined by

$$W = \frac{(b - a)}{K} \qquad (3.7)$$

where **K** is the number of velocity intervals the data span is to be divided into. The data is sorted such that

$$N = \sum_{i=0}^{K+1} N_i \qquad (3.8)$$

where N_i is the number of samples that fall into velocity interval **i**. The PDF is then defined to be

$$p(u') = \left[\frac{N_i}{N} \right] \left[\frac{K}{(b - a)} \right] \qquad (3.9)$$

where **u'** is the velocity corresponding to velocity interval **i**.

For the sample sets in this study, **K** is 256.

3.5.5 Spectral Analysis

The power spectrum, G(f) is calculated to determine the frequency content of the velocity data and is defined as

$$G(f) = \lim_{\Delta f \to 0} \frac{1}{(\Delta f)} \left[\lim_{T \to \infty} \frac{1}{T} \int_0^T u'^2(t,f,\Delta f)dt \right] . \qquad (3.10)$$

The one dimensional single sided power spectral density function is calculated by first performing a fast fourier transform (FFT) on the time series of data. Because the ASYST FFT routine can handle a maximum of 4,096 points, the series of 16,384 points is separated into four 4,096 point segments. The spectral analysis is carried out on each segment separately and the results are then averaged to obtain the final result. This procedure is described as "segment averaging" by Bendat & Piersol. Each segment of data is treated as follows:

A cosine taper is applied to each end of the segment using the function

$$X = X \left\{ \frac{1}{2} \left[1 - \cos \left(\pi \frac{n_i}{\left(\frac{N}{10}\right)} \right) \right] \right\} \qquad i = 1, 2, \ldots, \frac{N}{10} \qquad (3.11)$$

for the first N/10 data points, and

$$X = X \left\{ \frac{1}{2} \left[1 - \cos \left(\pi \frac{\left[\frac{N}{10}\right] - n_i}{\left[\frac{N}{10}\right]} \right) \right] \right\} \quad i = 1, 2, \ldots, \frac{N}{10} \quad (3.12)$$

for the last 1/10 of the data. In these expressions, X is the data value itself and N is the total number of data points in the segment. The cosine taper is suggested by Bingham, Godfrey, and Tukey (1967) as a way to minimize the side lobe leakage observed when an FFT is performed on a sectionally discontinuous function.

An FFT is then performed on the segment using the ASYST software. The equation

$$G(f) = \frac{2h}{N} |Y|^2 \tag{3.13}$$

where h is the sampling interval, is applied to each point in the positive (first) half of the FFT result (Y) to obtain the single sided power spectral density. The remaining portion of the FFT output is a mirror image of the first half and pertains to the (imaginary) negative frequencies. The energy contributed by this portion of the spectrum is reflected in the factor of 2 in equation 3.13.

An advantage of the segment averaging technique is that it is actually a "smoothing" procedure. The major disadvantage is that because the effective sample record length is reduced to one fourth of the original record length, a portion of the low frequency information is lost.

The validity of each spectrum computed is checked by calculating the root mean square velocity through the integration of the spectral density function,

$$u_{rms} = \sqrt{\int_0^\infty G(f)\, df} \tag{3.14}$$

and comparing it to the rms calculated directly from the time series velocity data (eq. 3.3).

The nondimensional spectrum (E(f)) is defined by

$$E(f) = \frac{G(f)}{(u_{rms})^2} . \tag{3.15}$$

The integral length scale is a measure of the large scale eddies in the flow and is defined by

$$\ell = U \int_0^\infty R(\tau)\, d\tau \tag{3.16}$$

where $R(\tau)$ is the autocorrelation function. It is computed by numerically performing a forward and then inverse FFT on the time series data to obtain an autocorrelation. Eight data segments are used, each augmented with zeros to avoid the overlapping circular autocorrelation, as recommended by Bendat and Piersol. Additionally the spectrum is reflected before the inverse transform as suggested by Akins and Peterka (1975). The resulting array is then numerically integrated to the first zero crossing using the ASYST software to obtain the integral length scale, ℓ.

Eddy diffusivity is a relative measure of turbulent mixing and is a scaling factor used in the convective diffusion equation to scale the magnitude of turbulent diffusion against convective transport. Tennekes and Lumley (1977) show that the eddy diffusivity, K, is proportional to the product of a length scale and velocity characteristic of the flow. Thus eddy diffusivity is represented as

$$K \alpha u_{rms}\, \ell \tag{3.17}$$

where u_{rms} is the rms velocity and l is the integral length scale.

CHAPTER 4

RESULTS

Flow measurements are made using hot-film anemometry to characterize the differences induced in the gas flow by varying precipitator electrode geometry. Horizontal and vertical streamwise mean flow and turbulence intensity profiles are obtained downstream of both the wire-plate precipitator model as well as a representative planar electrode (Plate A) to determine the tunnel flow characteristics. Further time series velocity measurements for all electrodes are taken at the center of the the channel downstream of the active precipitator model for varying precipitator current density values. These measurements are used to compute digitally the probability density functions and power spectra and to plot turbulence intensity versus current density curves. Additionally, the autocorrelation is calculated to obtain an estimate of an integral length scale and gas diffusivity.

Flow visualization is performed using a laser light sheet to view the flow in the inter-electrode space of the precipitator.

4.1 Electrical Characteristics

4.1.1 Current-Voltage Characteristics

Figure 4.1 plots the current-voltage (I-V) characteristics for each of the tested electrodes. The data is independent of gas speed over the range investigated (0-2 m/sec). The I-V curves indicate two

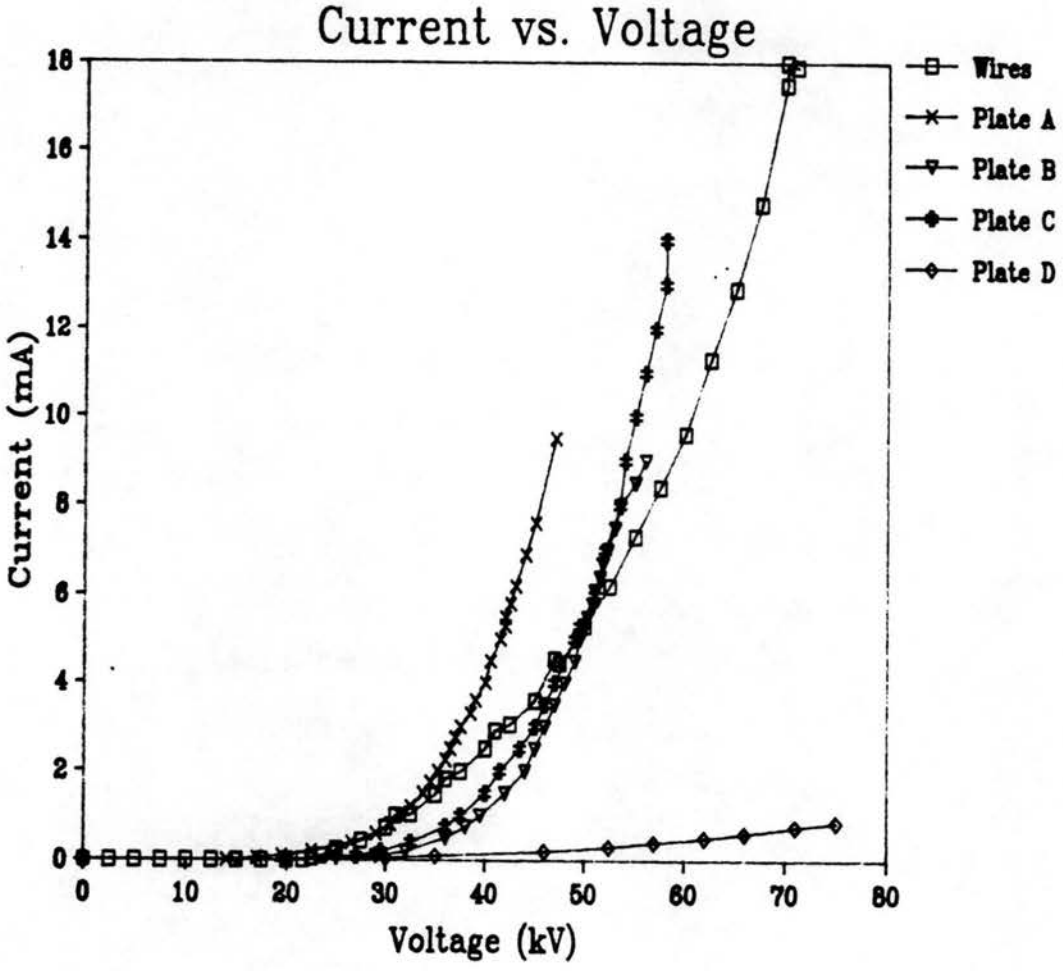

Figure 4.1. Current-voltage characteristics.

crucial points. The first is the initiation of a corona discharge when the applied voltage is sufficiently high to cause current flow. In the wire-plate geometry, corona onset occurs at approximately 20 kV. Current is first measured in the half-channel planar geometries at 15 to 17 kV. In this geometry, the onset of corona occurs at lower voltages because of a slight reduction in electrode separation due to the raised barbs. The large electrode spacing of the full-channel geometry with plate D results in a higher voltage of nearly 30 kV before a corona discharge is established. The second important data point on the I-V curve is the current and voltage at which sparkover occurs. Sparkover in the wire-plate precipitator is achieved at 68 kV and 15.0 mA. In the half-channel planar geometries sparkover occurs at substantially lower voltages and current levels: 47 kV and 9.5 mA for plate A; 55 kV and 8.5 mA for plate B; 56 kV and 11.0 mA for plate C. The voltage and current levels at sparkover in the plate D full-channel configuration are not known. The 1 kW power supply cannot provide sufficient voltage to produce a sparkover in this geometry.

Sparkover does not always occur at precisely the values quoted above. On humid days, sparkover can occur at lower voltage levels. In addition sparkover may occur at lower voltage levels after the precipitator has been operating for a length of time (e.g. 15-20 min). Reasons for this may include a buildup of static charge on the Plexiglas tunnel surfaces. Each electrode can also be operated at the higher electric potentials, shown on the I-V curves, but only for a few seconds at a time, as sparkover occurs almost immediately. Both the onset of corona and sparkover are discussed further in section 4.1.2 in terms of the visual appearance of the discharge.

The I-V curve for plate D differs greatly from all others for three reasons. First, the electrode to collector plate spacing for plate D is 15.2 cm (6 in), covering the full width of the test channel, in which the electrode plate is mounted on one side of the channel and the ground plate on the other. The electrode to plate spacing for all other electrodes is only half of the channel width (the electrode is mounted in the center of the tunnel and ground plates are positioned on each side wall). The large plate spacing of the plate D electrode results in much lower current flow for a given voltage. Second, because there is only one ground plate in the plate D configuration, the ground electrode area is half of that of each of the other electrodes, thus yielding double the current density for a given total current. (Note that the plot is current vs. voltage, not current density vs. voltage.) Third, the maximum voltage available from the high voltage power supply is not sufficient to produce the rapid rise in current seen in the other I-V curves.

The shift to the left in the I-V curve for plate A, relative to the other plate electrodes, is due to a reduction in electrode spacing. While the barbs on all plates result in a reduced electrode to collector spacing over that of the wires, the thumb tack barbs used for plate A are slightly longer than the wire barbs used for plates B and C (5 mm vs. 3.5 mm). In addition, Plate A is constructed of two metal sheets riveted back to back while the other center plates use only one sheet. The resulting decrease in electrode spacing creates the opposite effect observed for plate D. More current is present for a given voltage.

The only other major differences in the shapes of the I-V curves are their slopes. Initially, the rate of current increase with

voltage is highest in the wire geometry. This trend reverses once the wire discharge pattern stabilizes. An exception is the full-channel geometry of plate D. As mentioned above, the voltage available is not sufficient to produce a rapid rise in the I-V curve. This is reflected in the fact that plate D never attains a full discharge on all barbs. At the highest available voltage (75 kV) only the edge barbs are brightly lit.

4.1.2 Observations of Corona Discharge

Because of the vastly differing geometries of the wire and planar electrodes, the appearances of the corona discharge of the two electrode types also differ. In addition, the corona discharge character changes for each electrode as the applied voltage is increased.

In examining the wire electrodes, the discharge cannot be seen nor heard until an applied voltage of 20 kV is reached. As the voltage is slowly increased beyond 20 kV, each wire attains a dull blue glow, along with a few strong (bright) tufts. The tufts are bright blue in color and are generally stationary. The dull blue glow completely encases each wire, creating the image of a twinkling or moving "sheath" on each wire. The intensity of the dull glow increases slightly as voltage is applied. This is accompanied by an audible hiss, which grows louder as the voltage is increased. The twinkling or movement is most likely caused by the smooth stainless steel wire used for the electrodes and would not occur on a corroded wire, typical of those found in an industrial installation. In such a case, discharge tends to stabilize at points of surface imperfection.

The dull blue glow is generally nonexistent within 1 cm of a strong tuft. As the voltage is increased beyond 40 kV the strong tufts grow more prevalent and completely extinguish the dull blue glow. The distance at which these strong tufts can co-exist is reduced to 1 cm, from approximately 2 cm when first observed. At higher voltages many of the strong tufts move rapidly up and down the wire, sometimes forcing otherwise stationary tufts to move when the distance between the tufts becomes small.

The appearance of the planar electrode discharge differs from that of the wires since all discharges on a planar electrode occur on the barbs. For all planar discharge electrodes (with the exception of the full-channel configuration) the first observed corona discharge points occur at a lower voltage level because of the reduced electrode separation. For each plate in the half-channel configuration, the corona discharge first appears on the barbs along the edges of the plate, most prominently on the vertical edges. This usually occurs at about 15 to 17 kV. As the voltage is increased, points on the interior portions of the plate begin to discharge and the discharge at the plate edges appears to strengthen. As in the case of the wire electrodes there is an audible hiss, but it is not as loud as in the case of the wire electrodes.

Just prior to sparkover (45 kV for plate A and 55 kV for plate B) almost all barbs on plates A and B contain a corona discharge that is fairly strong although the edge discharges are slightly stronger than the others. Plates C and D never reach a complete discharge. Plate C is similar to plate B but contains twice as many discharge barbs. Approximately half of these points contain a discharge just prior to sparkover. Again, all edge barbs are discharging at 45 kV. This

appearance indicates that there is greater current flow at the edge barbs. In some cases one side of a plate in the half-channel configuration lights up slightly brighter than the other. This is most likely due to poor centering of the plate in the channel.

In the full-channel configuration, Plate D never contains any interior discharging barbs due to the lack of voltage needed at the larger plate separation. At the maximum voltage of the power supply (75 kV), the plate draws less than 1.0 mA of current and only the vertical edge points contain a visible corona discharge.

The current distribution is generally more uniform in the planar electrode situation for two reasons. First, the wire-to-wire spacing generates a much greater geometrical discontinuity (15.2 cm, 6 in.) than does the barb spacing of the plates (2.5 cm, 1 in. or less). Secondly, the individual corona discharge points are of higher intensity in the wire electrode situation because there are fewer discharge points. Assuming a total current of 5 mA, the average current of an individual tuft on the wires is 20.5 μA based on 1 cm tuft spacing. At an assumed current of 5 mA, the average discharge per barb for a half channel plate is 5.3 μA.

The only detrimental factor in the planar electrode current distribution is that of the edge effects mentioned above. The strong discharges at the leading and trailing edges of a plate create a more nonuniform field and actually may simulate the effects of two wires, one residing at each end of the existing plate position.

4.2 Flow Characteristics

4.2.1 Tunnel Characterization in the Absence of Corona

To determine the flow characteristics of the test facility, mean velocity and turbulence intensity profiles in the absence of a corona discharge are measured. It is important, in comparing the results of this study to actual precipitation operation, that the flow be two-dimensional. Figures 4.2 through 4.9 are streamwise mean velocity and turbulence intensity profiles obtained 46 cm downstream of the precipitator in the absence of a corona discharge at centerline mean flow speeds of 0.5, 1.0, and 2.0 m/sec. Both horizontal and vertical mean velocity and turbulence intensity profiles are obtained in the wire plate geometry, and the half-channel planar geometry.

Figure 4.2 shows the horizontal mean velocity profiles at the vertical center in the wire-plate geometry. The presence of the wires in the flow channel cannot be detected at flow speeds of 0.5 and 1.0 m/sec. At the 2.0 m/sec mean flow speed, a velocity deficit due to the wakes of the wires is measured at the channel center. The boundary layers near the walls also become more prominent at the 2.0 m/sec flow speed, each occupying approximately 1/4 of the flow channel width. The corresponding turbulence intensity profiles, shown in Figure 4.3, are very similar for each of the three flow speeds. At 0.5 m/sec, the turbulence intensity is 5% for the center 2/3 of the channel and rises to 30% near the walls. For bulk flow speeds of 1.0 and 2.0 m/sec, the region containing the 5% turbulence intensity is reduced to the center 1/2 of the channel and the turbulence intensity at the walls only rises to about 23%.

The vertical mean velocity profiles obtained at the tunnel horizontal center, shown in Figure 4.4, show that in the absence of a

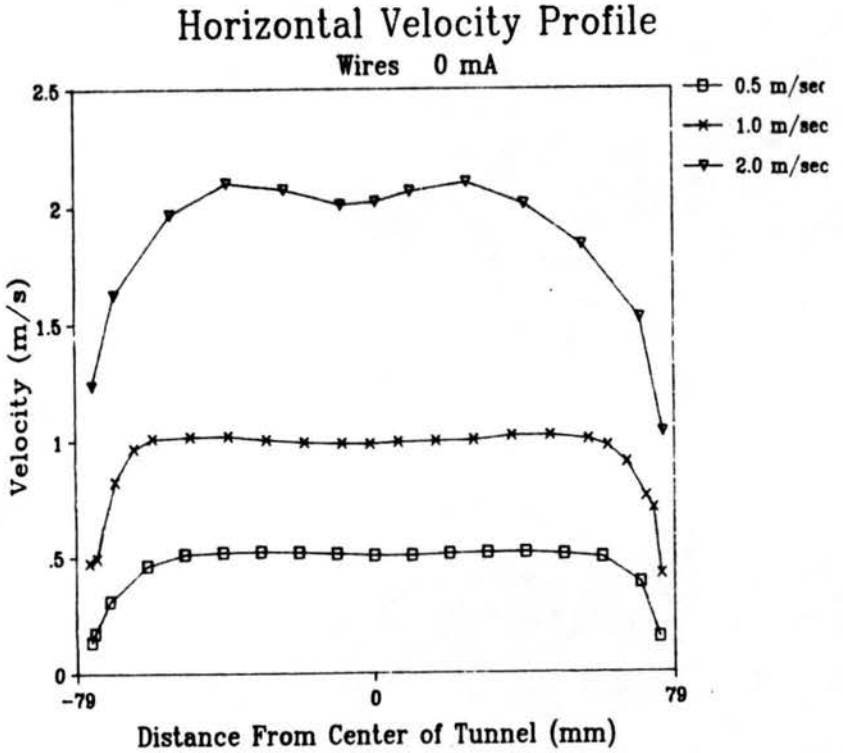

Figure 4.2. Horizontal mean velocity profiles at 0 mA in wire-plate geometry.

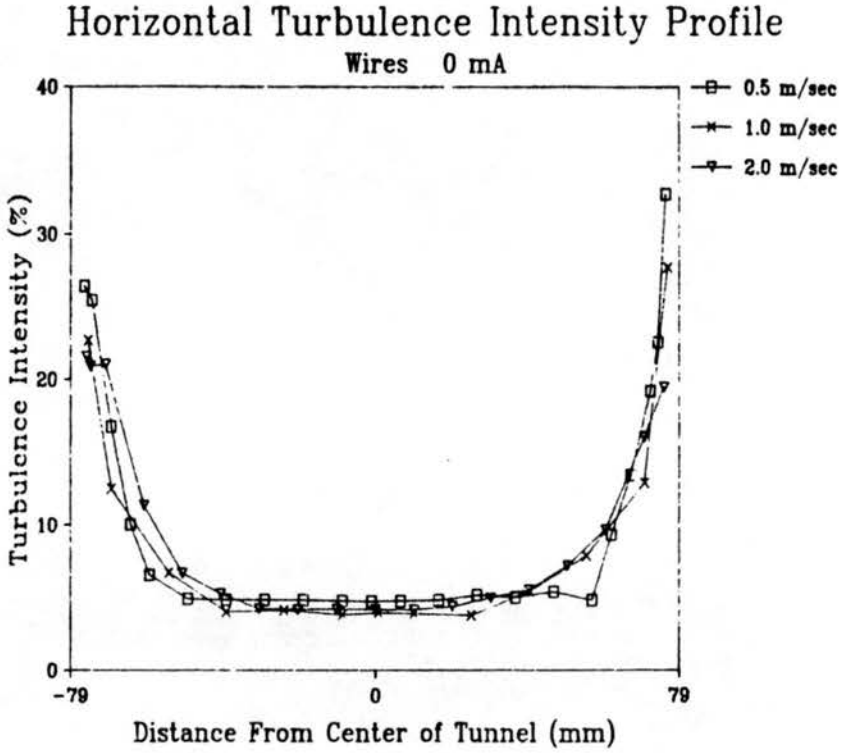

Figure 4.3. Horizontal turbulence intensity profiles at 0 mA in wire-plate geometry.

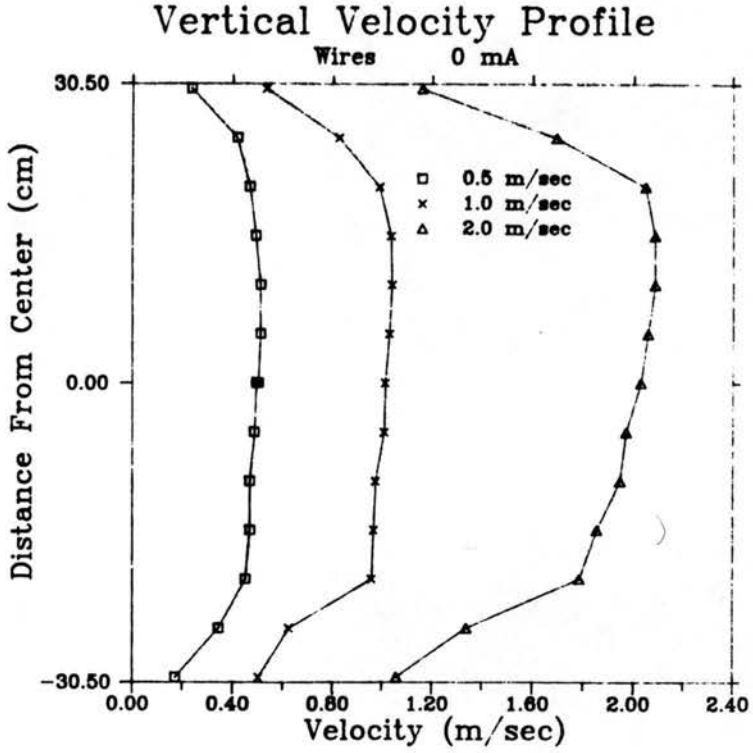

Figure 4.4. Vertical mean velocity profiles at 0 mA in wire-plate geometry.

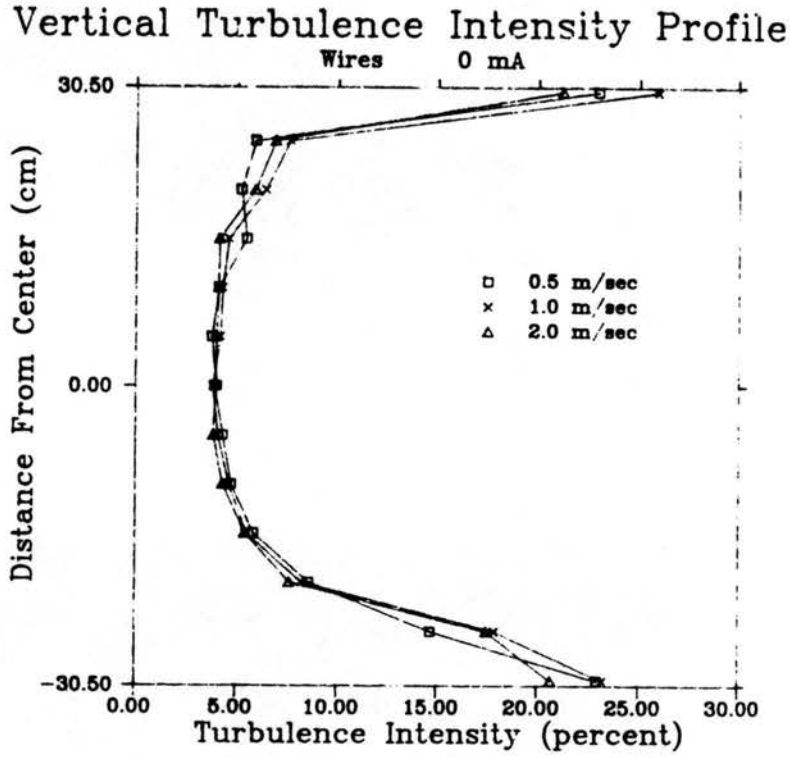

Figure 4.5. Vertical turbulence intensity profiles at 0 mA in wire-plate geometry.

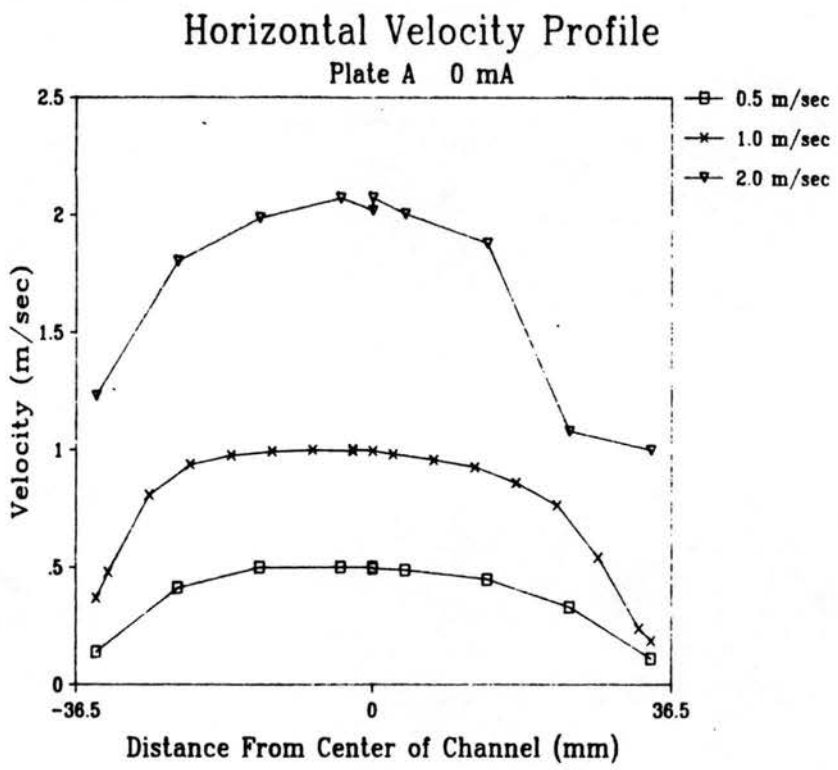

Figure 4.6. Horizontal mean velocity profiles at 0 mA in plate A geometry.

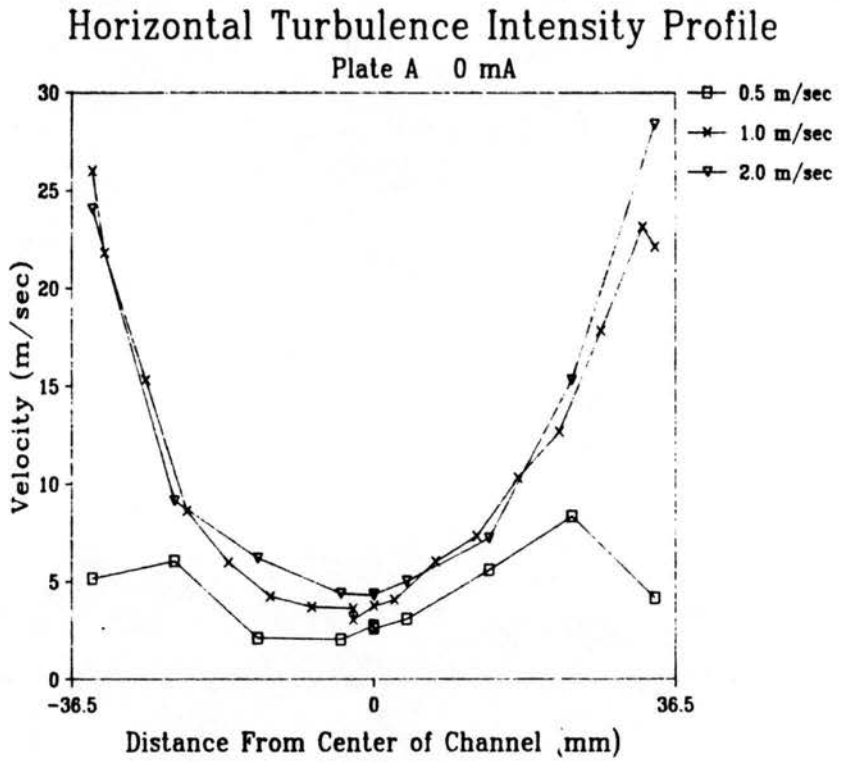

Figure 4.7. Horizontal turbulence intensity profiles at 0 mA in plate A geometry.

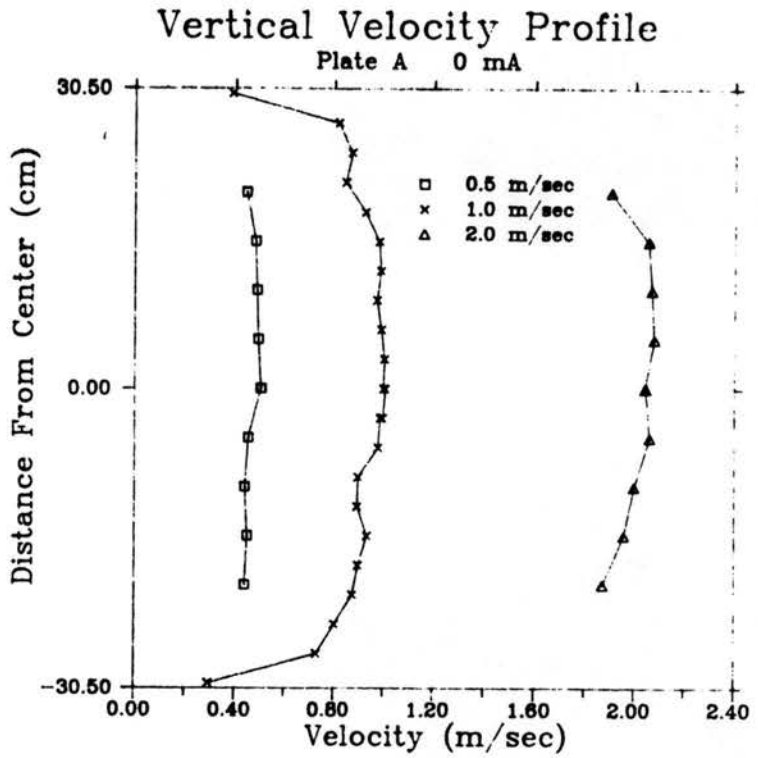

Figure 4.8. Vertical mean velocity profiles at 0 mA in plate A geometry.

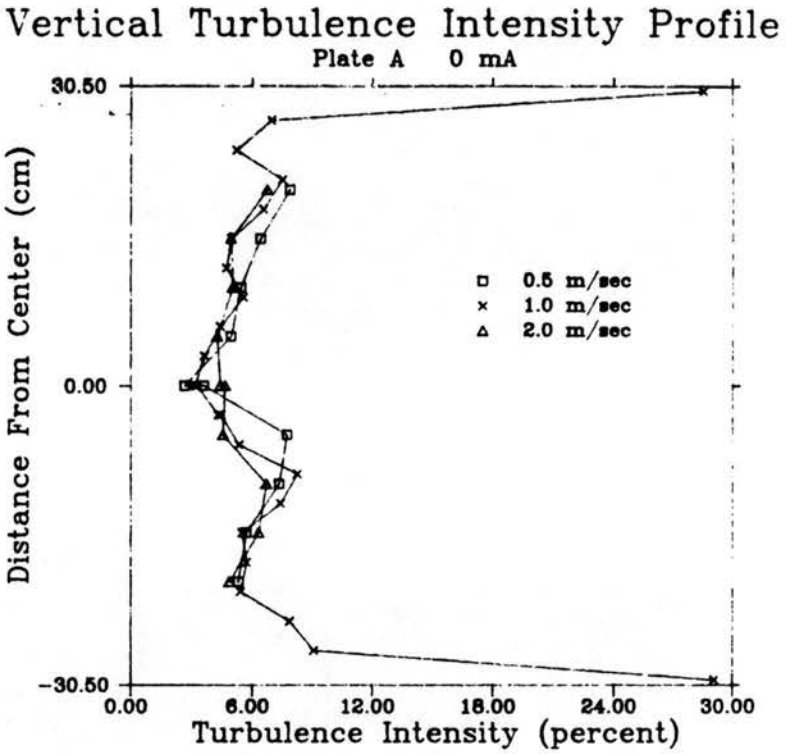

Figure 4.9. Vertical turbulence intensity profiles at 0 mA in plate A geometry.

corona discharge the tunnel flow is two-dimensional over 70% of the tunnel height for the wire-plate configuration. This is also reflected in the corresponding turbulence intensity profiles shown in Figure 4.5. For each bulk flow speed, the turbulence intensity profile is nearly identical, with the turbulence intensity being 5% throughout the center region and rising to approximately 23% at the floor and ceiling.

Figure 4.6 is a plot of the horizontal mean velocity profiles obtained for the half-channel planar configuration. The velocities are measured on the near side of the Plexiglas extension of the planar electrode and thus the horizontal profile shows only half of the entire tunnel width. The collector plate is located -36.5 mm and the barbed plate at +36.5 cm from the channel center. A larger boundary layer is detected near the center wall at the higher flow rates. This is most likely due to a more developed boundary layer caused by the planar electrode barbs protruding into the channel upstream of the measurement site. This is also reflected in the associated increases in turbulence intensity at the wall shown in the horizontal turbulence profile of Figure 4.7. The turbulence intensity rises more quickly to a maximum on the barbed side of the channel. This phenomenon is more pronounced at the 2.0 m/sec mean velocity where the maximum turbulence intensity near the barbed wall is 28% while the maximum for the flat wall is only 24%. The centerline turbulence is 5% for the 2 m/sec velocity and drops to less than 3% for the 0.5 m/sec mean flow speed.

The vertical profiles for the half-channel configuration are presented in Figures 4.8 and 4.9. The vertical profiles are also obtained on the near side of the Plexiglas extender walls. Nearly uniform mean flow is observed throughout the middle 70% of the channel

height at bulk velocities of 0.5 and 1.0 m/sec and over 50% of the tunnel height for the 2.0 m/sec flow rate. The associated vertical turbulence intensity profiles in Figure 4.9 show an average turbulence intensity of 6% throughout the center 70% of the channel although all curves vary from as little as 3% near the center to as much as 8% within the center section. In general, the velocity profiles for the half-channel planar geometry are not as uniform as those of the full-channel wire electrode geometry. The velocity variations may be a result of slight variations in barb length along the plate or may be due to a disturbance generated by the leading edge of the extender wall.

It is evident that bulk velocity has almost no effect on the turbulence intensity for the range of mean flow velocities investigated here. Also, the tunnel is essentially two-dimensional in the absence of a corona discharge, despite the fact that the tunnel has only a 4 to 1 aspect ratio. Full scale precipitators are truly two-dimensional with flow aspect ratios as high as 40 to 1.

4.2.2 Flow Visualization with Corona

Flow patterns for the wire-plate design and for full-channel planar electrode (plate D) are examined by introducing an aerosol into the tunnel and illuminating it with a laser light sheet. Two laser sheet orientations are used, one horizontal along the flow passage and the other vertical, perpendicular to the mean flow. The low power of the laser does not permit reliable photographs to be taken, thus none are presented. The following descriptions are based on direct observation and on video images. As the voltage is raised and more current is drawn visualization becomes difficult because more of the

aerosol begins to precipitate. For this reason, most observations are carried out at a current level close to the corona onset (approximately 20 kV). Gas velocity during these experiments is approximately 0.5 m/sec.

In the case of the wire-plate configuration, visualization in the vertical plane of the leading wire shows a general flow away from the wire when the precipitator voltage is introduced. The flow appears stronger in some locations, perhaps indicating the presence of a corona tuft. There is an obvious increase in turbulent mixing when the precipitator begins to draw current. In the horizontal plane, a definite increase in turbulence and a flow away from each wire is visible. This phenomenon is consistent up and down the length of each wire. A steady, circulating return flow between the wires is not clearly discernable, although there appears to be large scale motion in the region between the wires. Perhaps the return flow is difficult to see because of the influence of the electric field on the aerosols. When particles are being carried toward the collector plate by the gas, the electric body force acts in the same direction and enhances the motion. When the gas flow is attempting to carry the particles away from the wall, however, the electric body force acts against it. In addition, many of the particles are precipitated at the walls.

The planar electrode (plate D) is examined using a vertical sheet at the first row of barbs. Distinct jets are distinguishable originating from each barb and flowing toward the collector plate. When the sheet is positioned midway between the first two rows of barbs, the same jets are visible, beginning a slight distance from the planar electrode, at the point where they intersect the laser sheet. Similar jets are not observed for barbs in the interior of the plate.

This may be a result of a lack of particles due to precipitation or to a weak corona discharge in the interior. The horizontal sheet reveals two large secondary flows, one at the leading edge and the other at the trailing edge of the planar electrode. The flows are presumably due to the strong corona discharge through the barbs at the edges of the plate and a modification in the electric field at the Plexiglas side walls.

4.2.3 Mean Velocity Profiles With Corona

The effect of a corona discharge on the mean velocity profiles is shown in Figures 4.10 through 4.21. Velocity profiles for both the wire-plate geometry and the half-channel planar geometry are measured to check for tunnel two-dimensionality under the influence of the corona discharge. Both horizontal and vertical profiles of streamwise mean velocity are shown for bulk gas speeds of 0.5, 1.0, and 2.0 m/sec at precipitator currents levels of 0, 0.75, and 5.3 mA. Reynolds numbers for the three gas velocities are 4500, 9000, and 18,000 for the wire-plate geometry and 2250, 4500, and 9000 for the half-channel planar geometry, based on duct width. The electric number varies with current level, geometry, and gas speed as shown in Table 4.1.

Horizontal mean velocity profiles for the standard wire-plate precipitator at gas speeds of 0.5, 1.0 and 2.0 m/sec are shown in Figures 4.10 through 4.12, respectively. The data indicate that the electrical discharge has an insignificant effect on the mean velocity. The corona discharge does appear to have an effect on the mixing as shown by a slight flattening of the curves. The higher velocities are distributed closer to the walls, resulting in velocity profiles that are essentially constant for 90% of the tunnel width. In addition,

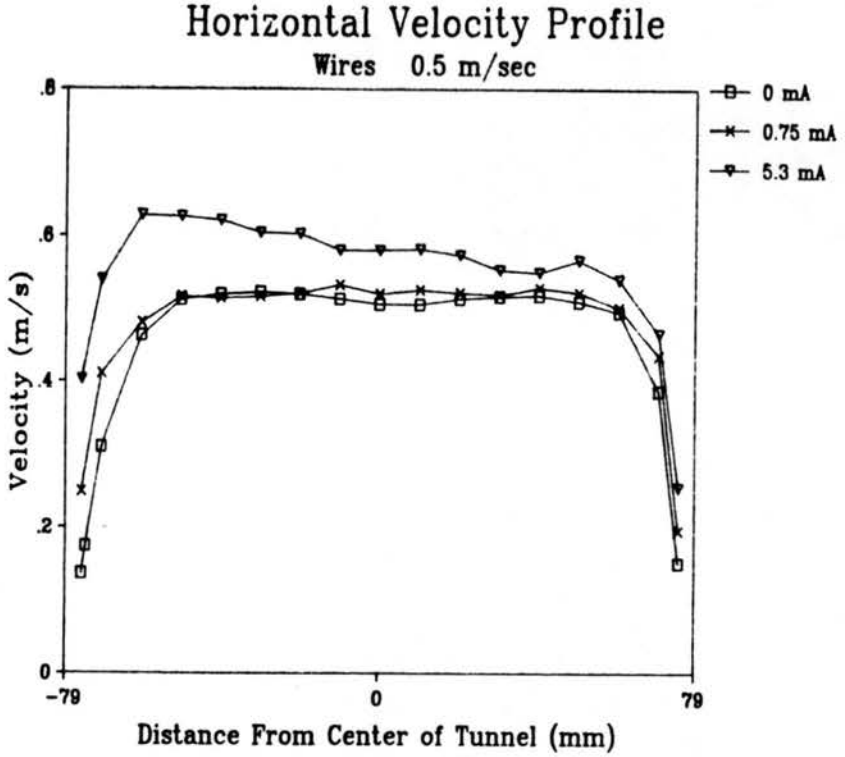

Figure 4.10. Horizontal mean velocity profiles with current in wire-plate geometry at 0.5 m/s.

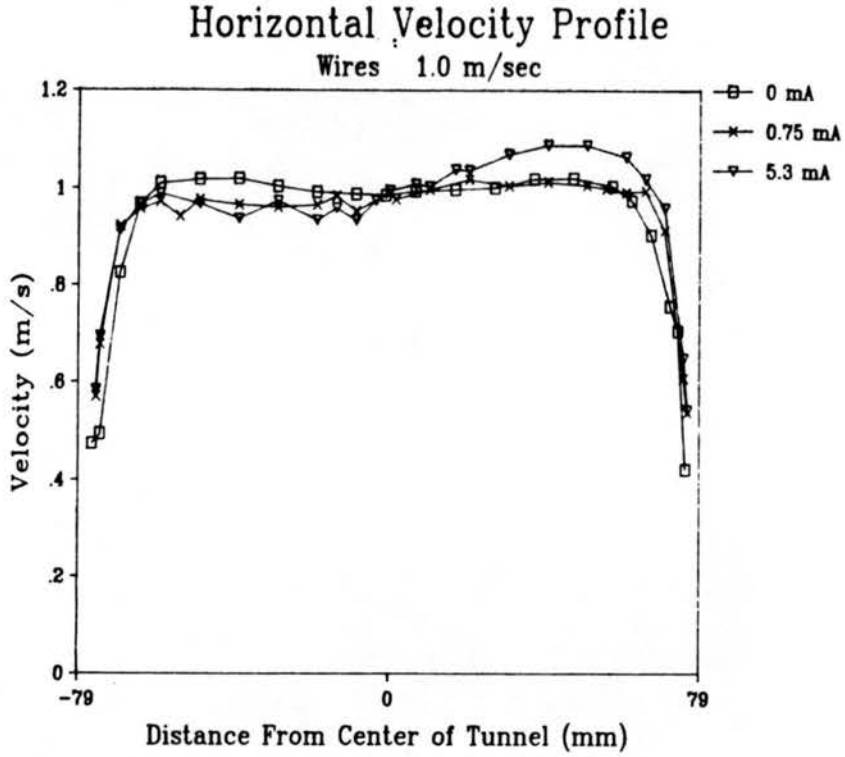

Figure 4.11. Horizontal mean velocity profiles with current in wire-plate geometry at 1.0 m/s.

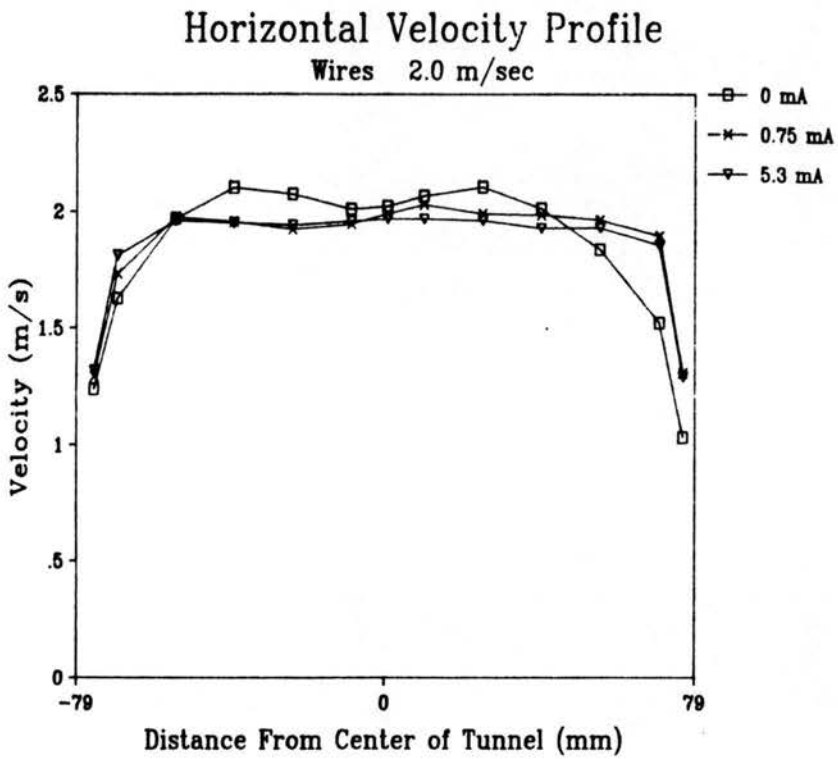

Figure 4.12. Horizontal mean velocity profiles with current in wire-plate geometry at 2.0 m/s.

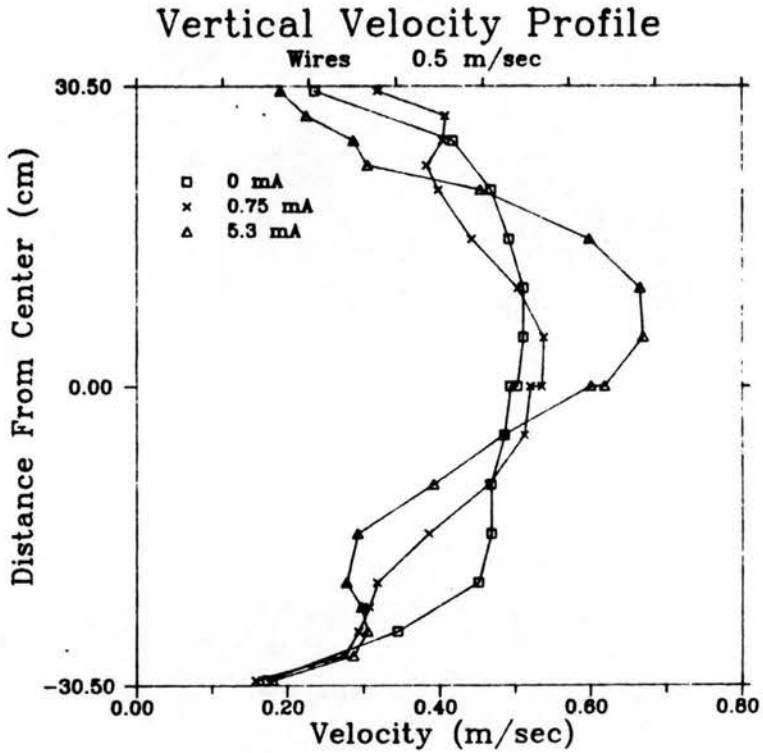

Figure 4.13. Vertical mean velocity profiles with current in wire-plate geometry at 0.5 m/s.

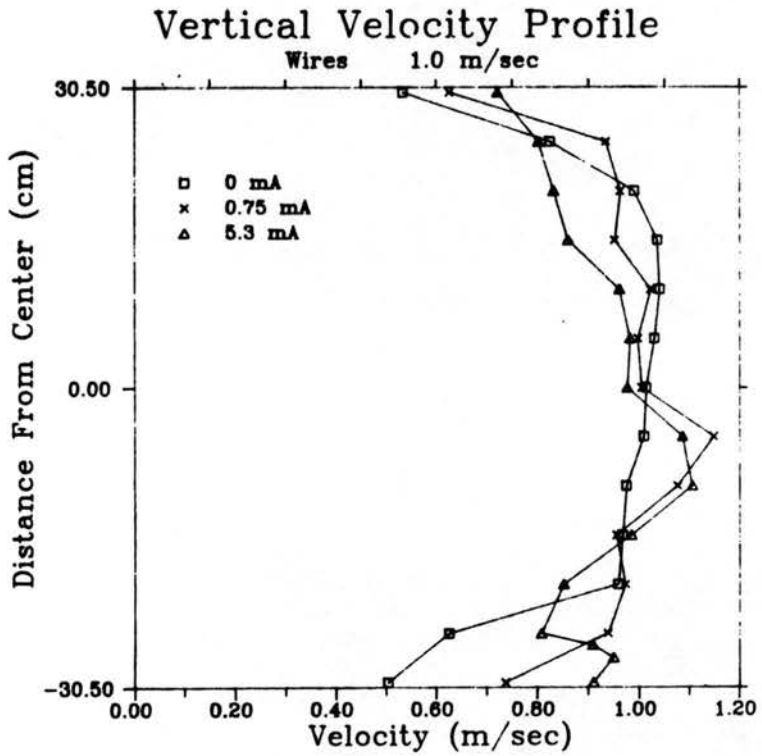

Figure 4.14. Vertical mean velocity profiles with current in wire-plate geometry at 1.0 m/s.

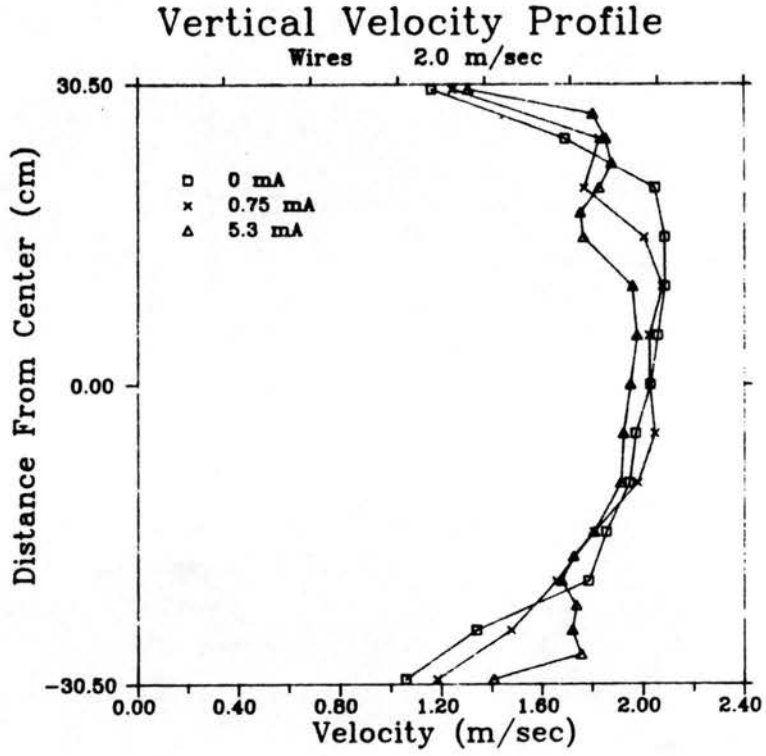

Figure 4.15. Vertical mean velocity profiles with current in wire-plate geometry at 2.0 m/s.

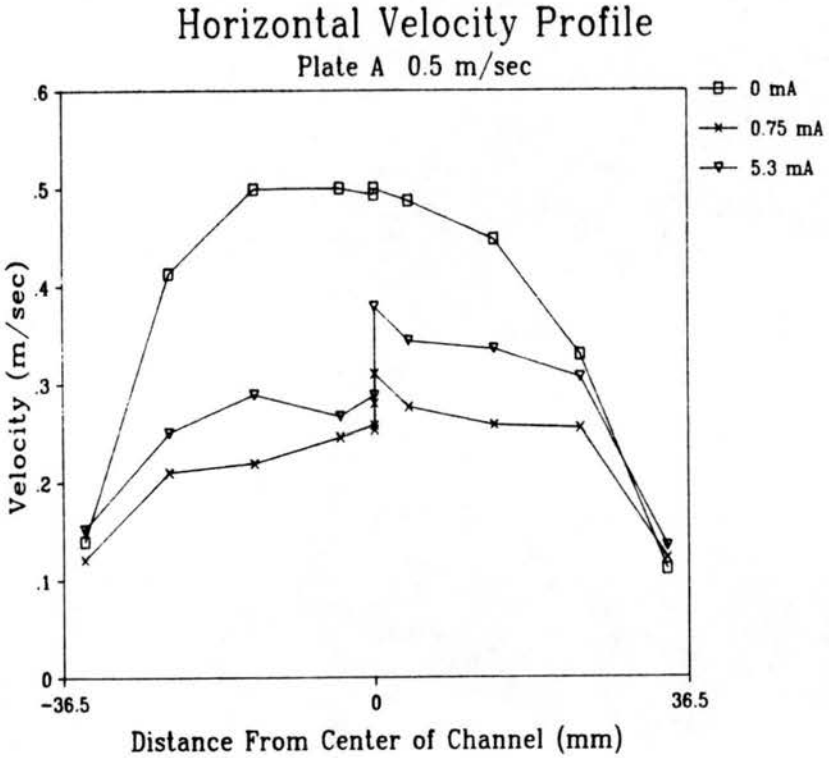

Figure 4.16. Horizontal mean velocity profiles with current in plate A geometry at 0.5 m/s.

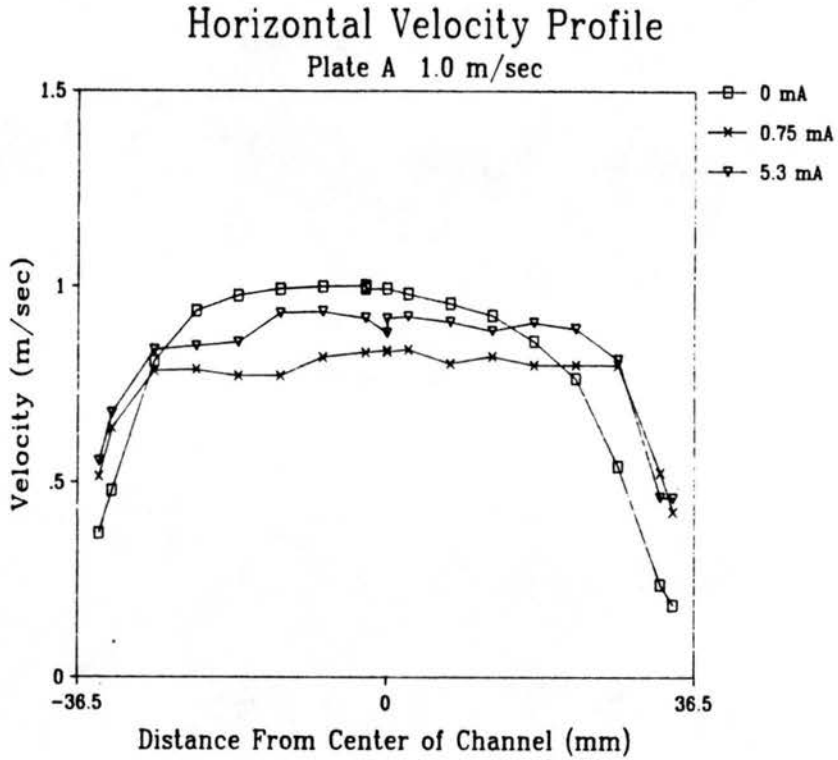

Figure 4.17. Horizontal mean velocity profiles with current in plate A geometry at 1.0 m/s.

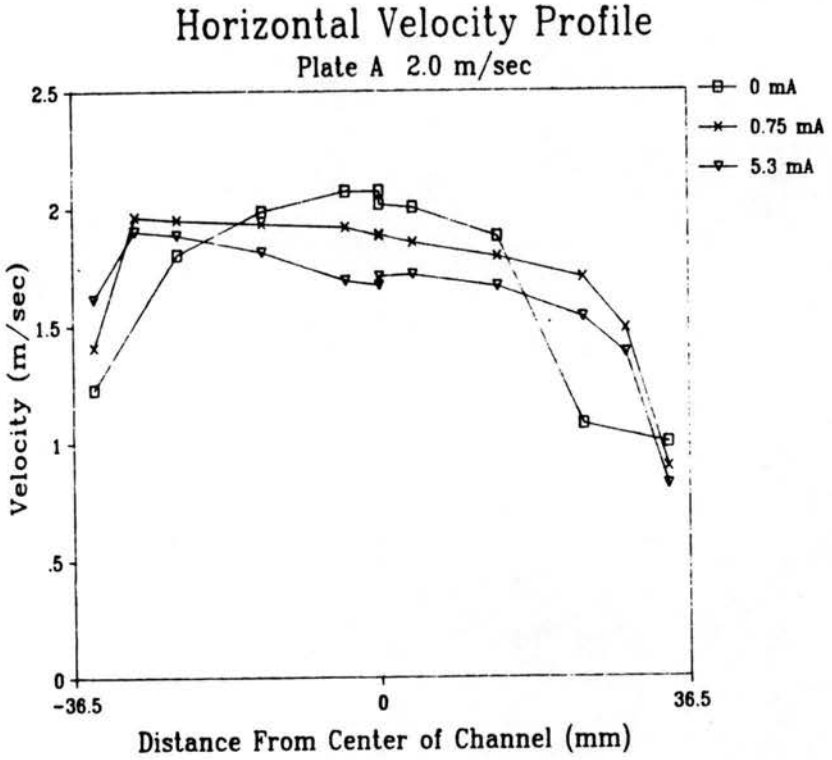

Figure 4.18. Horizontal mean velocity profiles with current in plate A geometry at 2.0 m/s.

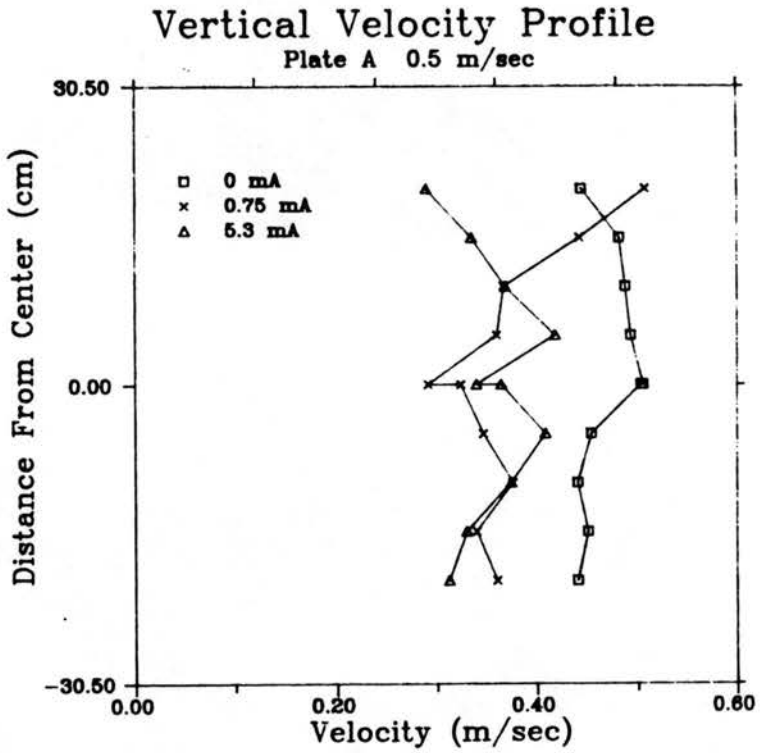

Figure 4.19. Vertical mean velocity profiles with current in plate A geometry at 0.5 m/s.

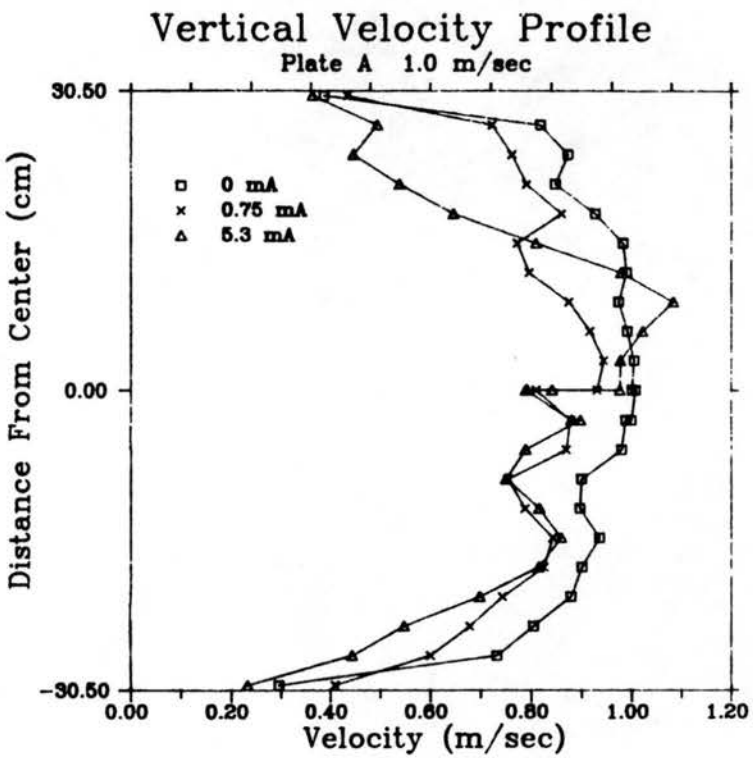

Figure 4.20. Vertical mean velocity profiles with current in plate A geometry at 1.0 m/s.

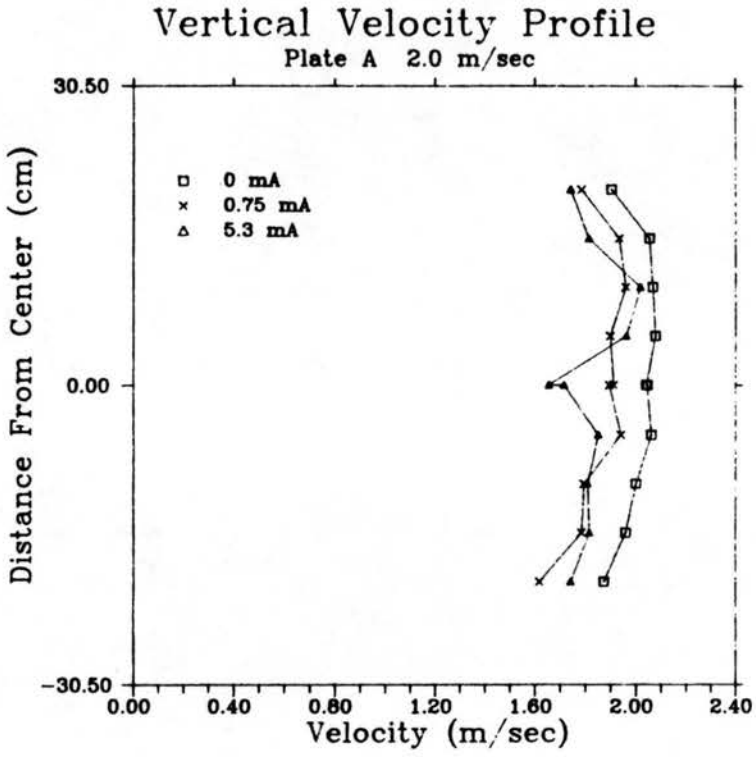

Figure 4.21. Vertical mean velocity profiles with current in plate A geometry at 2.0 m/s.

Table 4.1. Calculation of Dimensionless Electric Number, $F = [IL/\beta A\rho U^2]$

		For wire electrodes and half-channel planar electrodes:			For full-channel planar electrode (plate D):		
		Current (mA)			Current (mA)		
		0	.75	5.3	0	.375	.75
Gas	.5	.00	.92	6.52	.00	1.85	3.69
Velocity	1.0	.00	.23	1.63	.00	.46	.92
(m/sec)	2.0	.00	.06	.41	.00	.12	.23

Values based on the following:

L - Electrode to collector plate spacing
(.0762 m (3 in.) for half-channel geometry)
(.1524 m (6 in.) for full-channel geometry)
A - Collector plate area
(1.115 m^2 (24 in. by 36 in. times 2) for half-channel)
(0.557 m^2 (24 in. by 36 in.) for full-channel)
β - Negative ion mobility
(2.1E-4 $m^2/V \cdot sec$)
ρ - Gas (air) density
(1.058 Kg/m^3)
I - Total current
(as above (*.001 to convert to Amps))
U - Gas velocity
(as above)

the velocity deficit observed behind the wires in the no-voltage situation is no longer present when the precipitator voltage is applied.

At a mean velocity of 0.5 m/sec (Figure 4.10), there is an apparent rise in the velocity at 5.3 mA, but this is most likely due to an unstable fan velocity. In addition, the 5.3 mA curve on the 1.0 m/sec plot (Figure 4.11) shows a higher velocity on one side of the tunnel. This may be caused by an inconsistency in the corona discharge pattern (current density), with the mean flow favoring areas having a lower current density and cross flow. This would be the case if the discharge wires are not precisely centered in the tunnel.

Figures 4.13 through 4.15 are the mean velocity vertical profiles for the wire-plate geometry. The nonuniformity in the vertical profiles with a corona discharge for both the wire and planar electrodes suggests that the discharge is responsible for secondary flow patterns in both geometries. This is especially true for higher current levels at the lower gas speeds. The reason for this is revealed by examining the dimensionless electric number, equation 2.11. For the half-channel geometry the only values of the electric number greater than one are those for a current level of 5.3 mA at gas velocities of 0.5 and 1.0 m/sec, which are 6.52 and 1.63, respectively. Thus these are the only cases in which electric body force is greater than that of the inertial forces.

An interesting phenomenon is that of the velocities greatly increasing near the wall at the higher precipitator voltages. This is particularly evident in the 5.3 mA curve at 2.0 m/sec, shown in Figure 4.15. This arises most likely as a result of the large circulating secondary flow set up due to the presence of the Plexiglas top and bottom of the tunnel. This is observed in the flow visualization using the vertical laser sheet. Similar secondary flow patterns were observed by Leonard et al. (1981, 1983) in a Plexiglas-walled model precipitator.

Profiles for the half-channel plate-plate precipitator, shown in Figures 4.16 through 4.21, demonstrate characteristics similar to those evident in the analogous wire-plate channel curves. The 0.5 m/sec data displays a disturbing feature, however. The entire velocity curve drops for both the horizontal and vertical profile at higher precipitator discharges. This would seem to indicate an overall reduction in the bulk flow rate. One explanation for this is

that probe leakage occurred during the measurements, resulting in reduced apparent velocities. However, a check for high voltage influence on the probe in this configuration was made with the results showing that the precipitator voltage has no influence on the bridge voltage readings.

As in the wire-plate geometry the horizontal velocity profiles for the planar electrode are flattened at increased current levels, thus indicating greater turbulent mixing. The horizontal profiles at 2.0 m/sec exhibit a definite boundary layer on the electrode side of the channel in the no current condition. With the current on, the profile is slanted, with velocities of 2.0 m/sec on the side of the channel nearest the ground plate. On the other side of the channel, the velocity decreases steadily to 1.6 m/sec before dropping off sharply in the boundary layer on the electrode side of the channel.

The characteristics of the vertical mean velocity profiles for the half-channel planar geometry are strikingly similar to those of the wire-plate geometry at gas speeds of 1.0 to 2.0 m/sec. Large excursions in the profiles exist at higher current levels, particularly at low velocities. Once again, this is attributed to high electric numbers.

4.2.4 Turbulence Intensity Profiles with Corona

The magnitude of the electrically generated turbulence is a function of both the dimensionless electric number (eq. 2.11), which varies for a given geometry only with current and gas speed in this study, and the electrode geometry. Figures 4.22 through 4.33 are horizontal and vertical turbulence intensity profiles for the wire electrodes and plate electrode A.

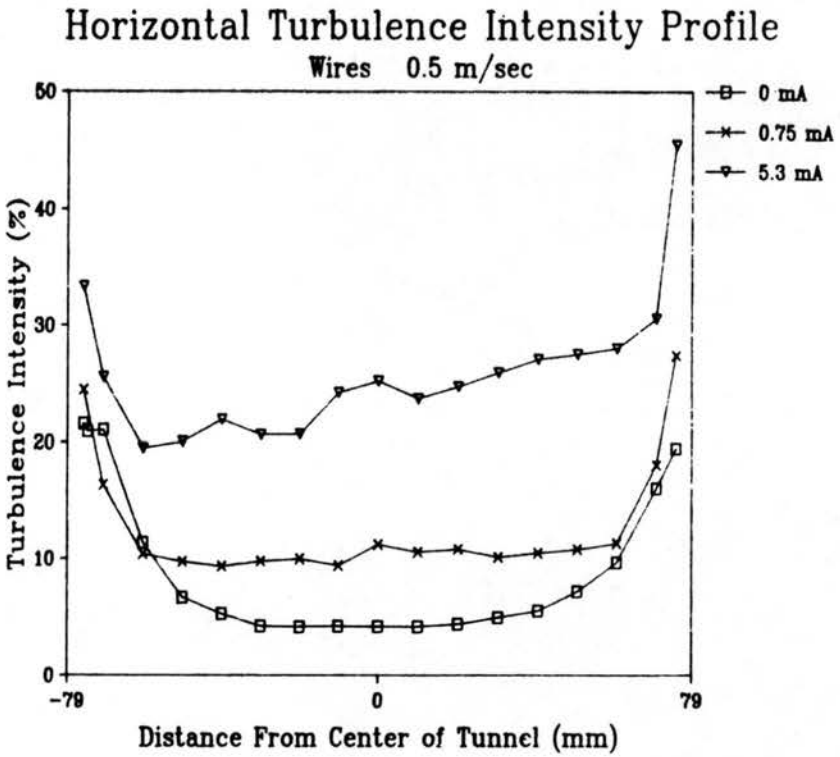

Figure 4.22. Horizontal turbulence intensity profiles with current in wire-plate geometry at 0.5 m/s.

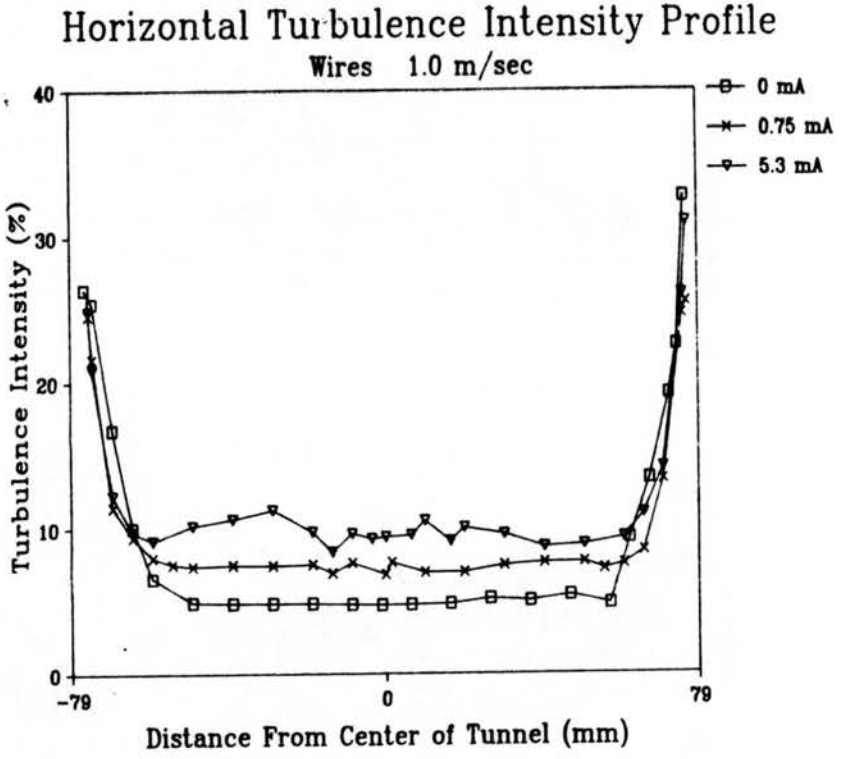

Figure 4.23. Horizontal turbulence intensity profiles with current in wire-plate geometry at 1.0 m/s.

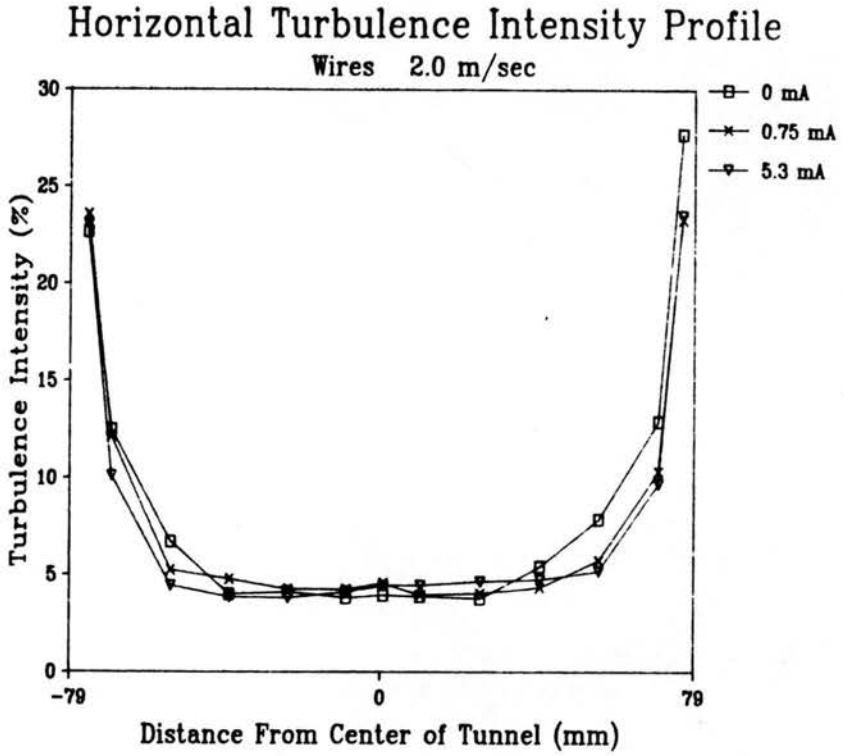

Figure 4.24. Horizontal turbulence intensity profiles with current in wire-plate geometry at 2.0 m/s.

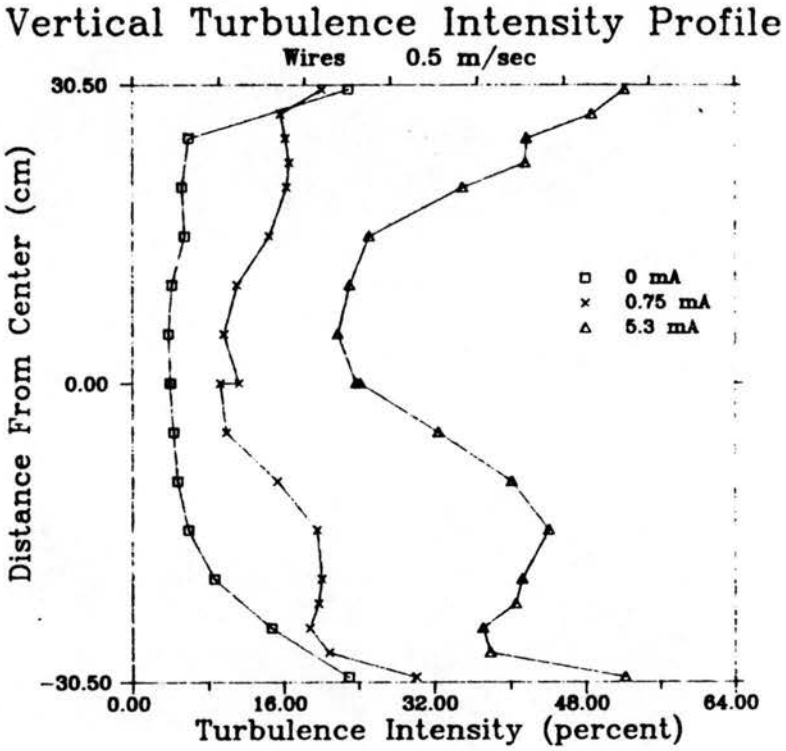

Figure 4.25. Vertical turbulence intensity profiles with current in wire-plate geometry at 0.5 m/s.

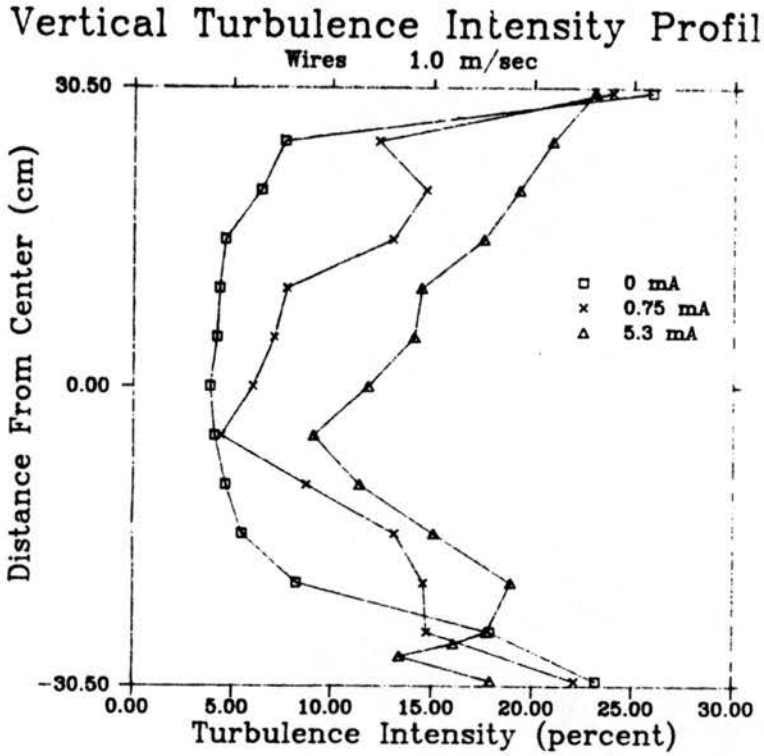

Figure 4.26. Vertical turbulence intensity profiles with current in wire-plate geometry at 1.0 m/s.

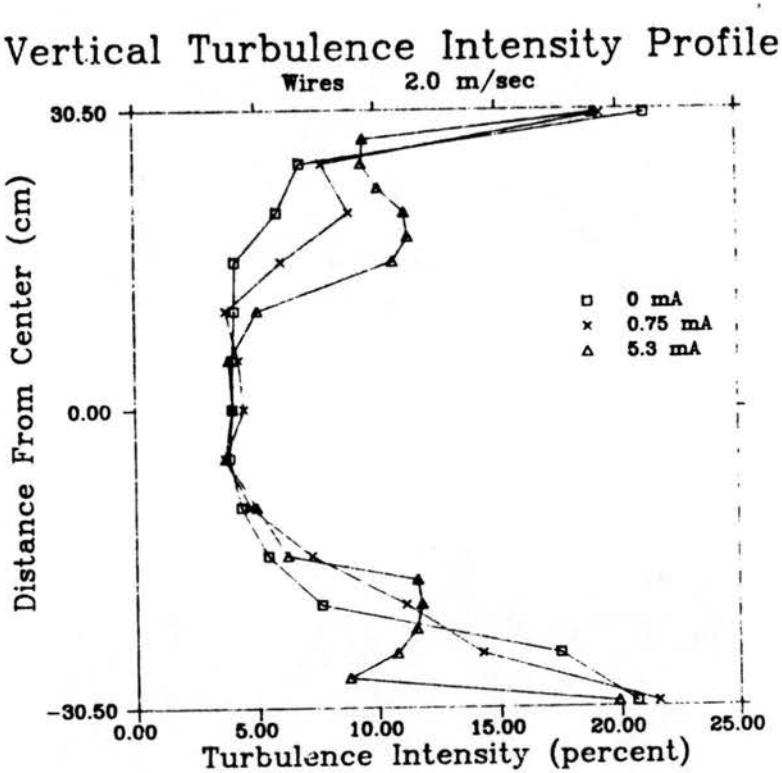

Figure 4.27. Vertical turbulence intensity profiles with current in wire-plate geometry at 2.0 m/s.

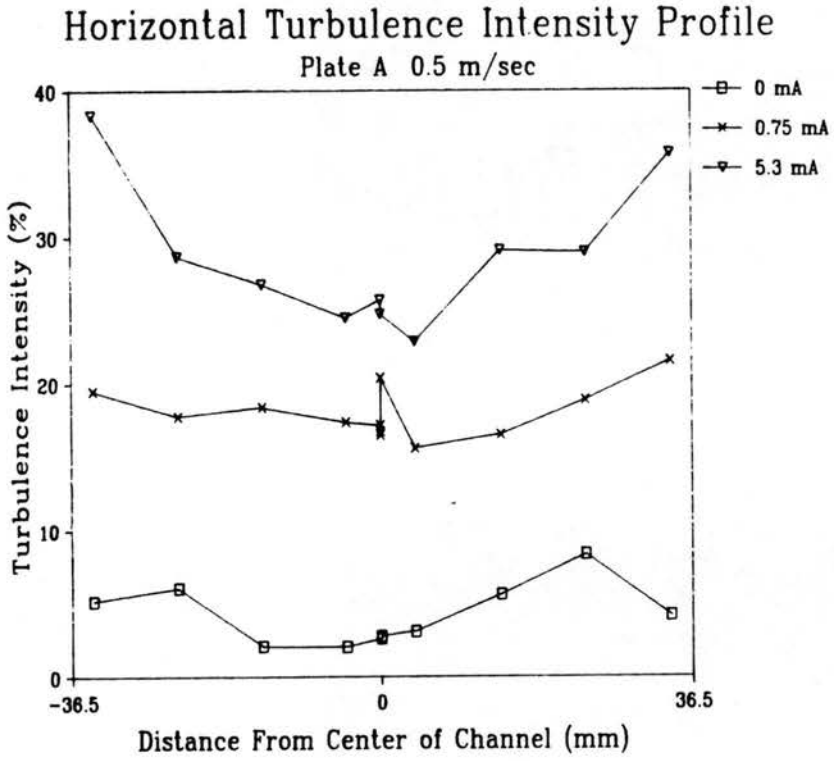

Figure 4.28. Horizontal turbulence intensity profiles with current in plate A geometry at 0.5 m/s.

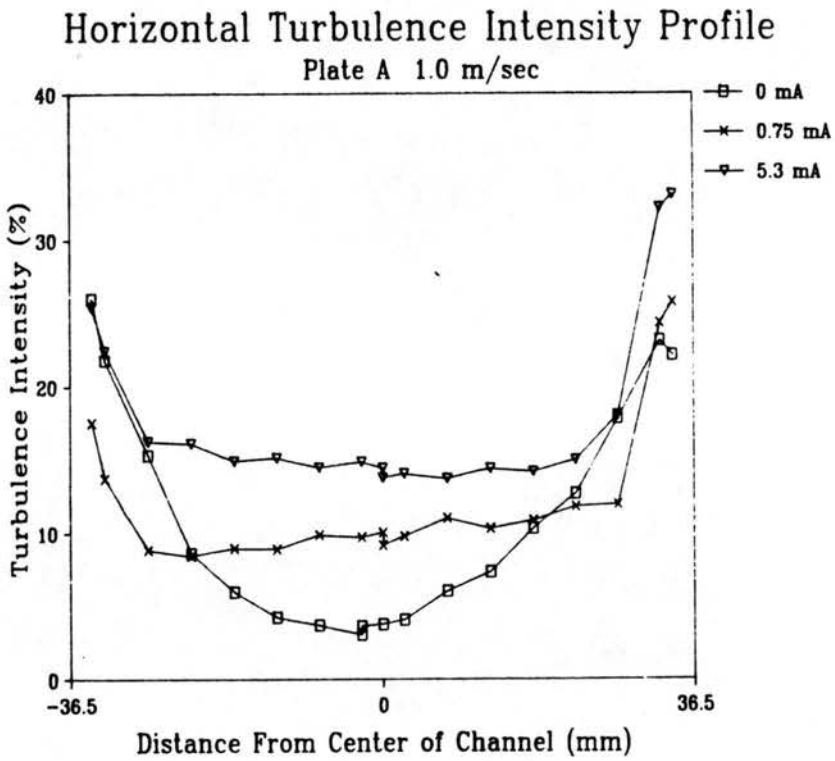

Figure 4.29. Horizontal turbulence intensity profiles with current in plate A geometry at 1.0 m/s.

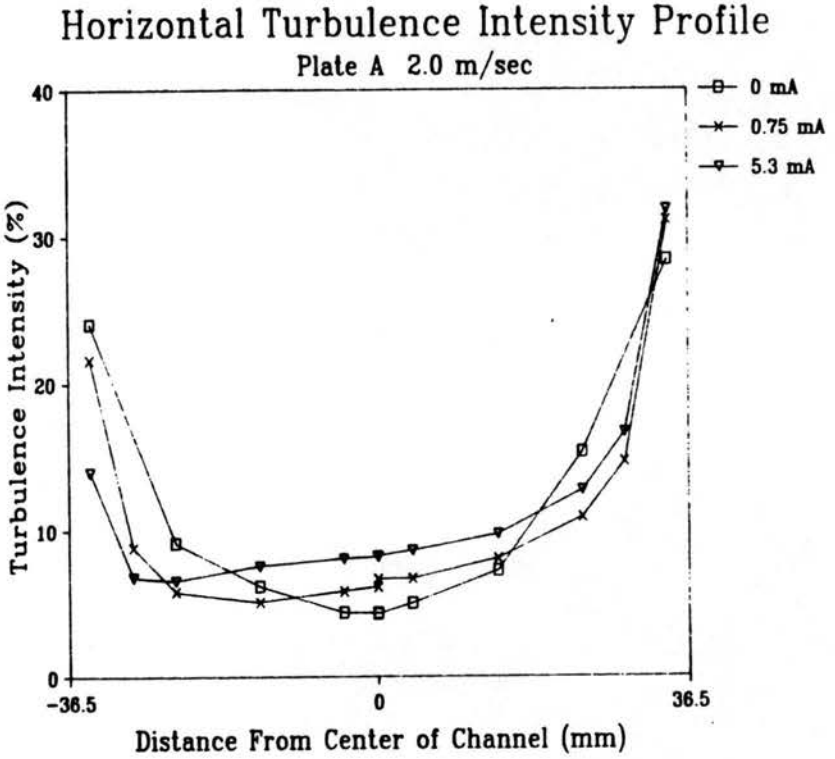

Figure 4.30. Horizontal turbulence intensity profiles with current in plate A geometry at 2.0 m/s.

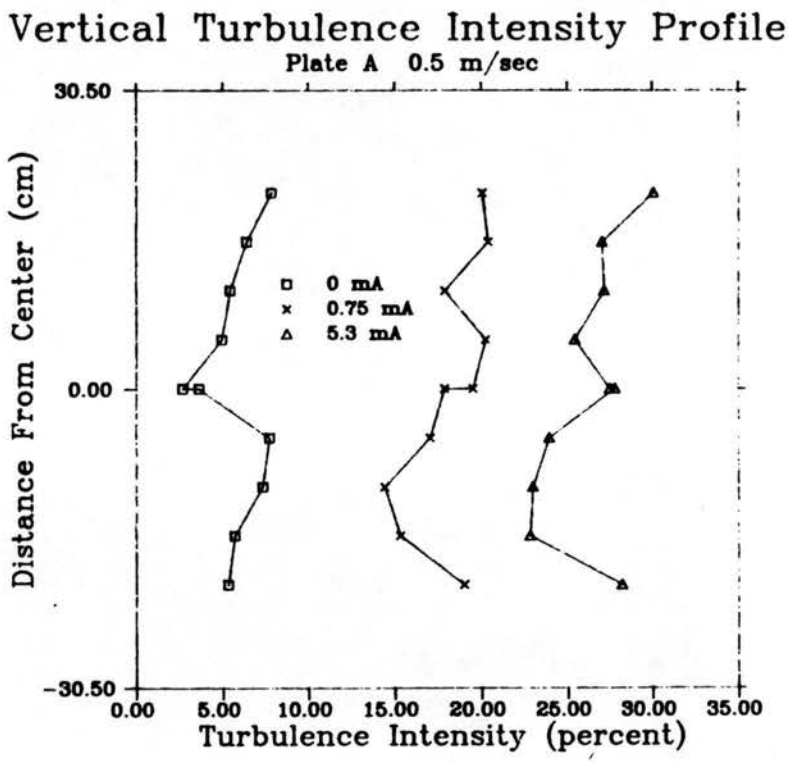

Figure 4.31. Vertical turbulence intensity profiles with current in plate A geometry at 0.5 m/s.

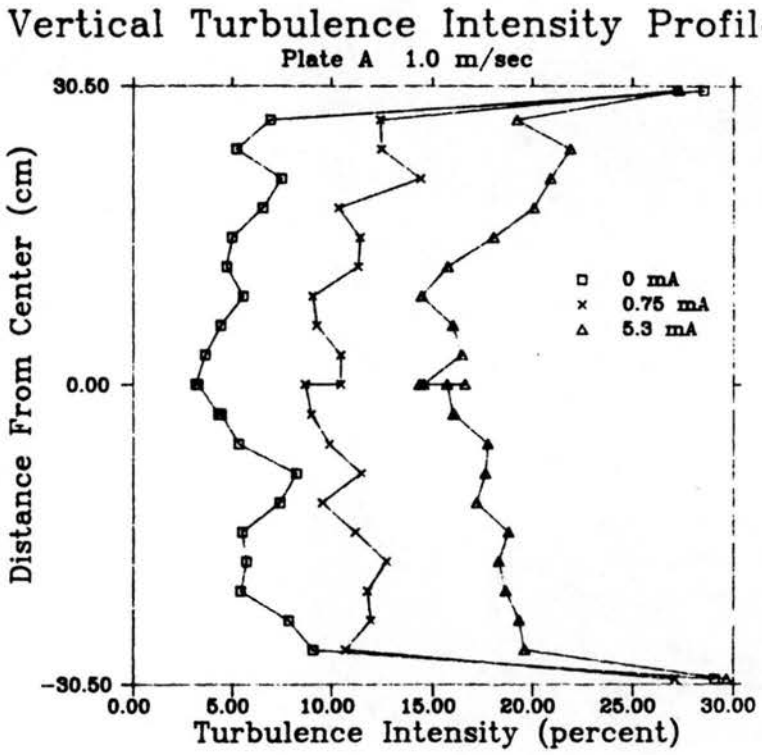

Figure 4.32. Vertical turbulence intensity profiles with current in plate A geometry at 1.0 m/s.

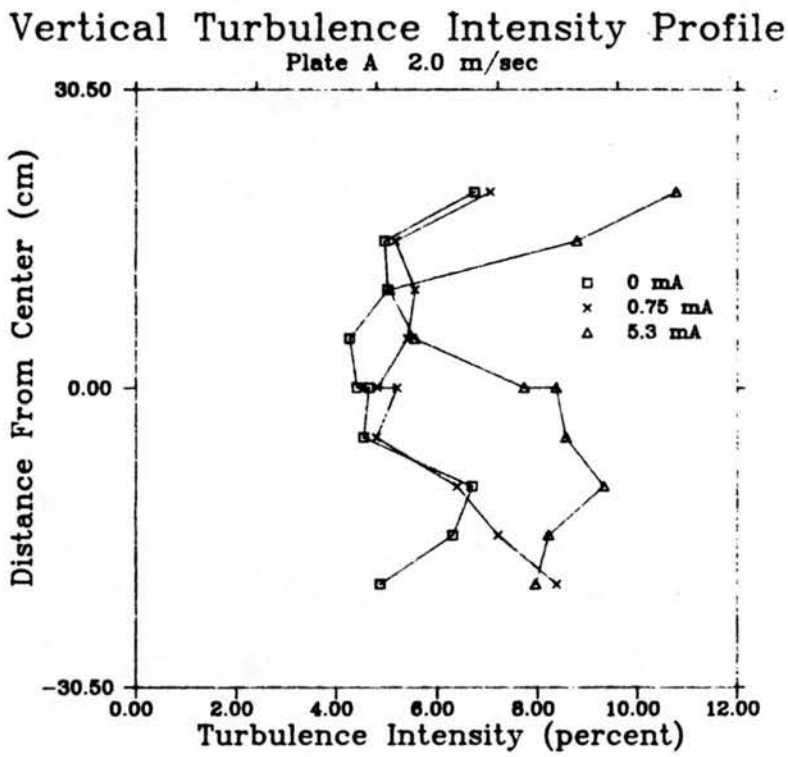

Figure 4.33. Vertical turbulence intensity profiles with current in plate A geometry at 2.0 m/s.

In the wire-plate precipitator, the corona discharge causes an increase in turbulence intensity over the background aerodynamic turbulence at gas speeds of 0.5 and 1.0 m/sec. As precipitator amperage is increased, the turbulence generated is increased. The effect is more pronounced at lower gas speeds. In fact, at 2.0 m/sec the corona discharge has no significant effect on the turbulence level.

As shown in Figure 4.22, at a bulk gas speed of 0.5 m/sec the turbulence intensity at the center of the tunnel in the wire-plate geometry increases from 5% in the no-current situation to over 20% with a discharge current of 5.3 mA. When the bulk velocity is doubled, the jump in turbulence intensity is much less, from 5% to 10% as shown in Figure 4.23. At a bulk velocity of 2.0 m/sec the horizontal turbulence intensity profile exhibits no change at increased current levels with the exception of a flattening of the profile, indicating greater mixing and a shrinkage of the boundary layer. This is easily explained in terms of the electric number. Close examination reveals that as gas velocity increases, the electric effect on the flow due to a given amount of current is less. As the current through the electrodes increases, the electric body force increases and thus more turbulence is generated in the flow. As the bulk flow velocity is increased, the effect of the electrically generated turbulence is decreased. The electric number for the wire electrodes at a gas velocity of 0.5 m/sec and a discharge of 5.3 mA is 6.52, as shown in Table 4.1. When the bulk gas velocity is increased to 2.0 m/sec the electric number drops to 0.41.

The vertical turbulence intensity profiles for the wire plate geometry are shown in Figures 4.25 through 4.27. Comparison with the

corresponding vertical mean velocity profiles (Figures 4.13 through 4.15) reveals that the turbulence intensity is highly mean velocity dominated. Large excursions in the curves corresponding closely to those in the velocity profiles are observed in the turbulence intensity profiles.

Turbulent intensity profiles for the barbed plate electrode are plotted in Figures 4.28 through 4.33. The planar electrode generally produces more turbulence than does the wire electrode configuration. At a bulk gas speed of 1.0 m/sec, the aerodynamic turbulence at the center of the horizontal profile (Figure 4.28) is less than 5%. At a current level of 5.3 mA in the planar electrode geometry, the centerline turbulence intensity increases to over 15% as compared to 10% in the wire-plate geometry. At higher gas velocities, increased current results in a flattening and raising of the turbulence intensity profile. As the electric number suggests, the electrical effects diminish as mean velocity is increased. At 1.0 m/sec, the turbulence intensity at the centerline increases to 15% at a current level of 5.3 mA over a base aerodynamic turbulence of 5%. At 2.0 m/sec the turbulence intensity increases to only 10% at the same current level.

The vertical turbulence intensity profiles for plate A, shown in Figures 4.31 through 4.33, show the same large-scale fluctuations observed in the wire-plate profiles. At a bulk velocity of 2.0 m/sec, the turbulence intensity ranges from 4% to 10% within the center 70% of the tunnel. In addition, the profiles are consistent with the planar geometry horizontal turbulence intensity profiles in that there is a greater turbulence increase due to the electric body force than there is in the wire-plate geometry. The large increase at a gas

speed of 0.5 m/sec appears to be velocity dominated. The velocity along the profiles consistently drops as current is increased, as observed in Figures 4.16 and 4.19.

4.2.5 Centerline Turbulence Intensity

The difference in turbulence production by the five discharge electrodes is easily seen in the plots of turbulence intensity as function of current density shown in Figures 4.34 through 4.41. As observed in the turbulence intensity profiles presented earlier, electrical turbulence production is a strong function of gas velocity. As gas velocity increases, turbulence generation decreases. This is true for all geometries, but note that the planar geometries show an increase in turbulence at 2.0 m/sec but the wire-plate geometry does not. This is particularly evident when examining Figures 4.39 through 4.41, which include all electrodes.

Turbulence intensity rises most rapidly with current density at current densities below 0.25 mA/m^2 for all electrodes. Figure 3.39 shows that at a gas velocity of 0.5 m/sec, the turbulence intensities measured for plates A, C, and D continue the rapid rise until a current density of 1.0 mA/m^2 is reached. At this point, the turbulence intensity is 30% for plate D and 20% for plates A and C. Beyond a current density of 1.0 mA/m^2 the rise in the turbulence intensity curves is more gradual (and almost non-existent at the 2.0 m/sec flow rate).

In general, the planar electrodes produce more turbulence than do the wire electrodes, although in some situations the levels of turbulence generated are not entirely different. For instance, at a bulk gas velocity of 0.5 m/sec (Figure 3.39), plates A and B produce

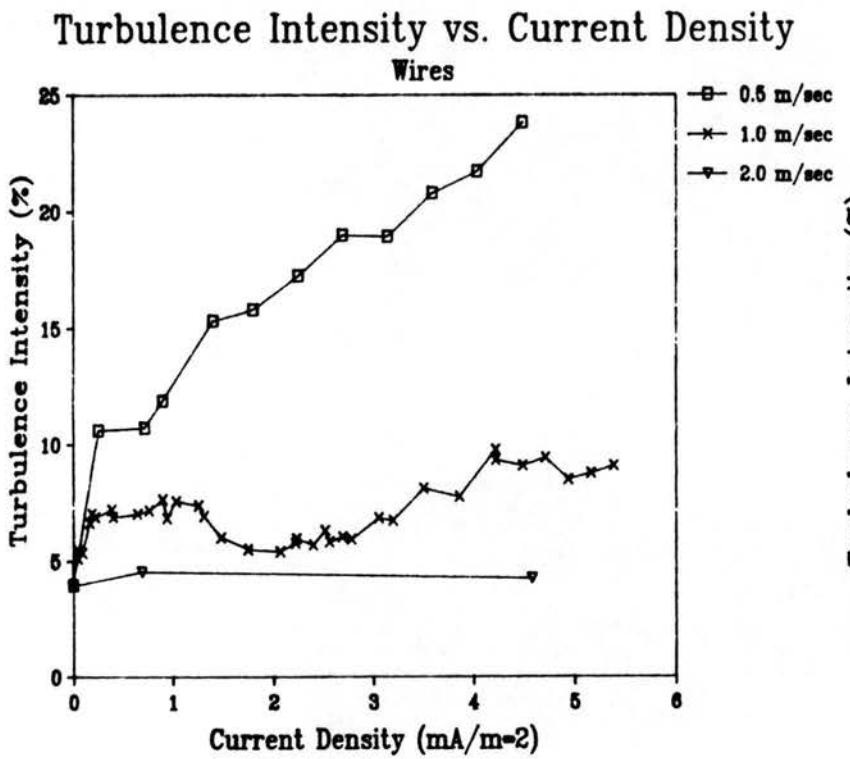

Figure 4.34. Plot of midpoint turbulence intensity as a function of current density in wire-plate geometry.

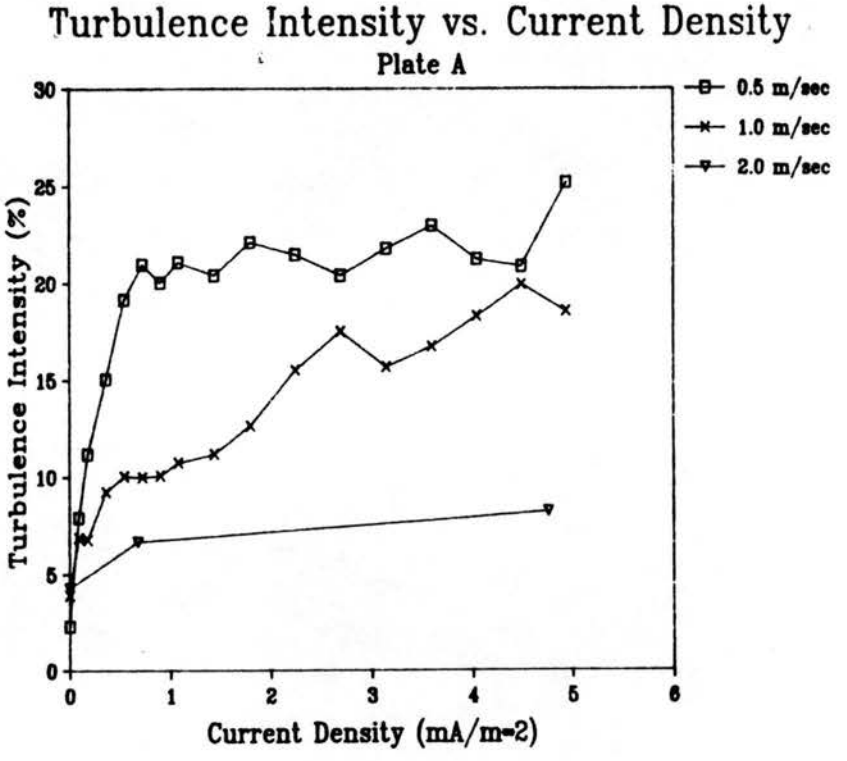

Figure 4.35. Plot of midpoint turbulence intensity as a function of current density in plate A geometry.

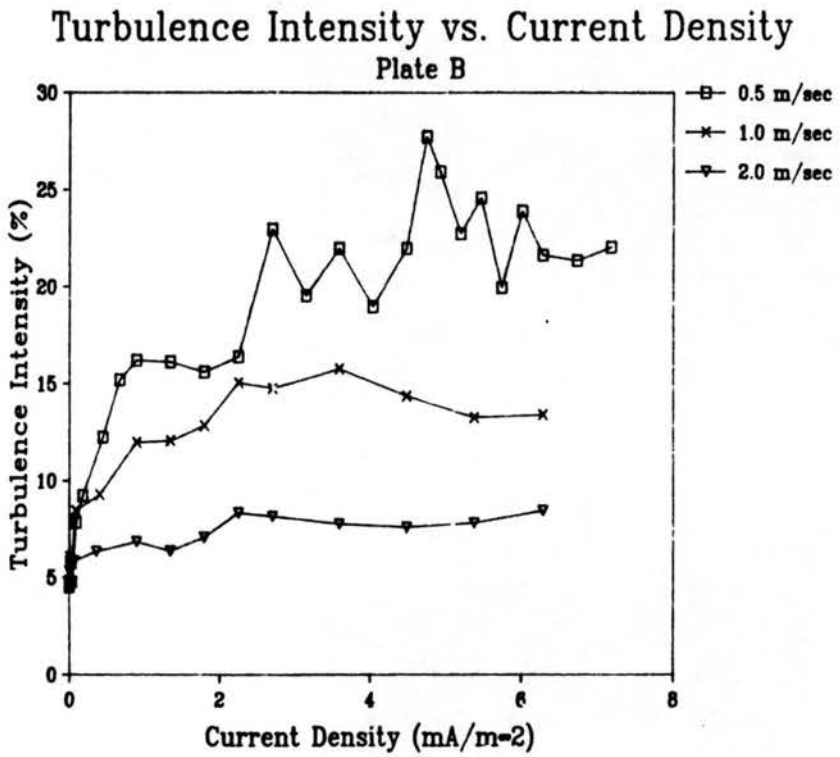

Figure 4.36. Plot of midpoint turbulence intensity as a function of current density in plate B geometry.

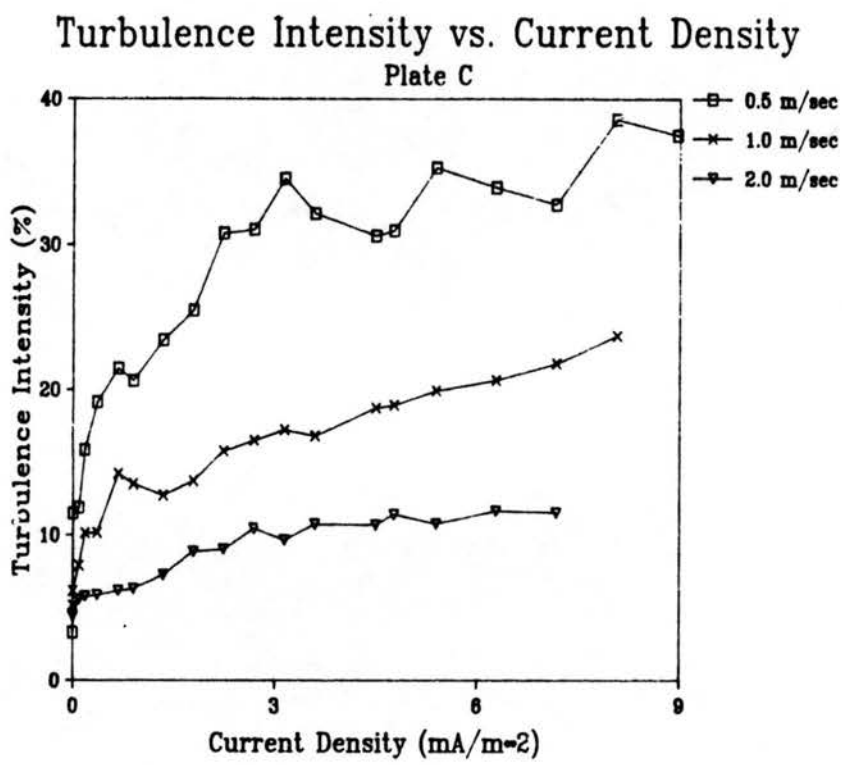

Figure 4.37. Plot of midpoint turbulence intensity as a function of current density in plate C geometry.

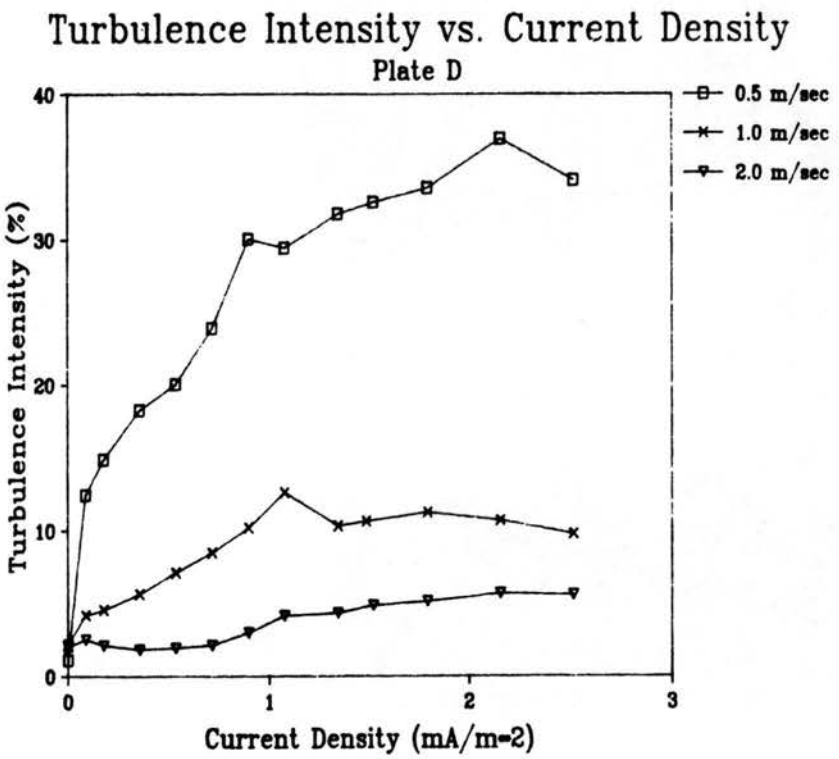

Figure 4.38. Plot of midpoint turbulence intensity as a function of current density in plate D geometry.

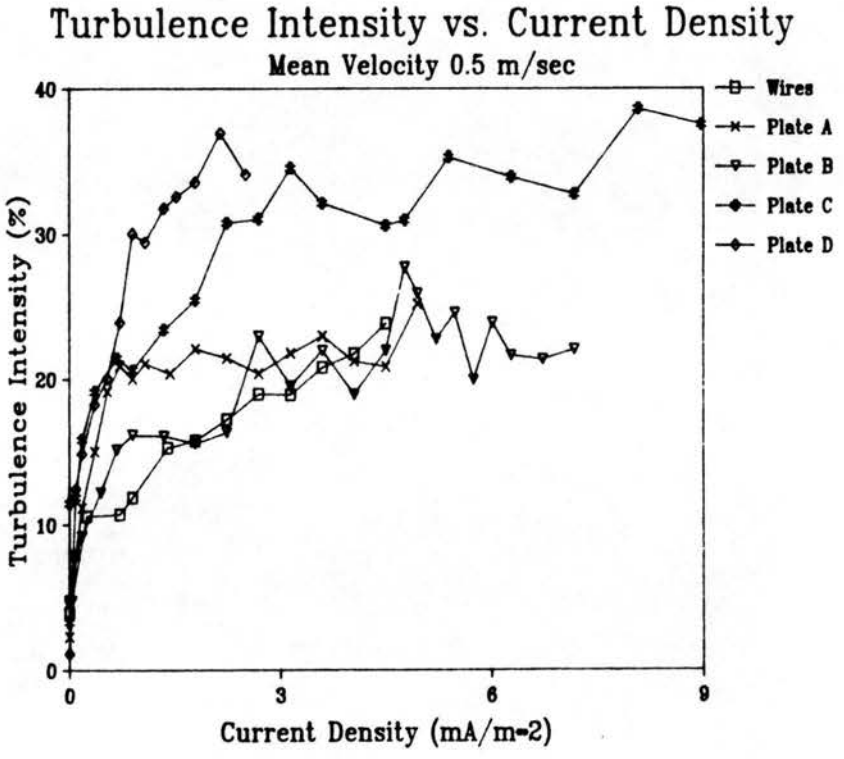

Figure 4.39. Plot of midpoint turbulence intensity as a function of current density in all geometries at 0.5 m/s.

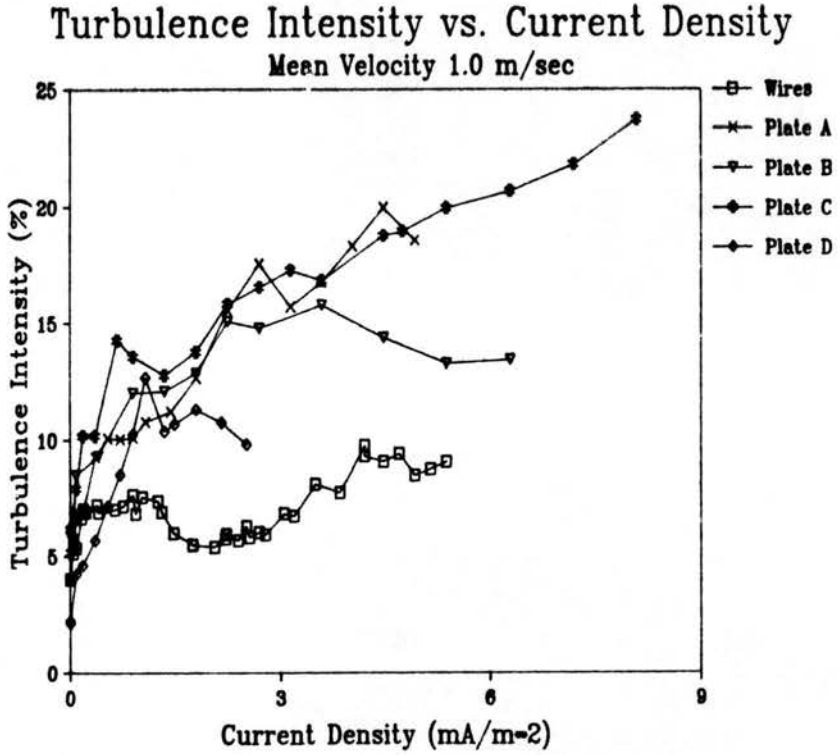

Figure 4.40. Plot of midpoint turbulence intensity as a function of current density in all geometries at 1.0 m/s.

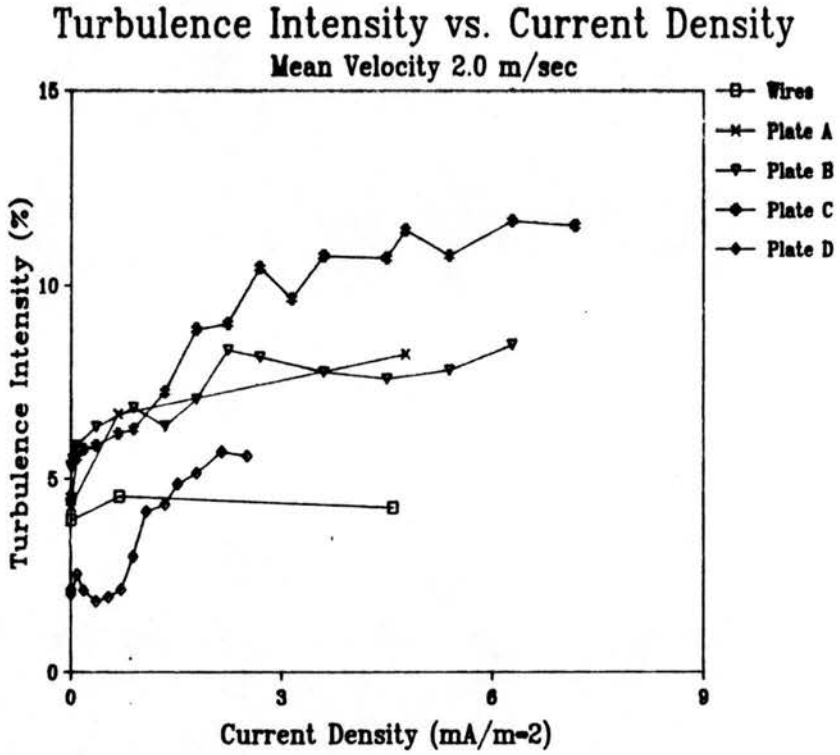

Figure 4.41. Plot of midpoint turbulence intensity as a function of current density in all geometries at 2.0 m/s.

close to the same level of turbulence as the wires beyond a current density of 3 mA/m^2. The turbulence intensity appears to stabilize near 20%.

At 2.0 m/sec, shown in Figure 3.41, the turbulence generated by both the wire electrodes and plate D falls within the same range, below 5%. Plate C produces at least as much turbulence as all other electrodes for almost all current densities at each of the three tested gas speeds. The only case in which this does not hold true is at a bulk velocity of 0.5 m/sec. Plate D maintains a turbulence intensity above 30% for current densities between 1 and 3 mA/m^2 while the turbulence intensity for plate C remains below 30%. Both plates generate an increase in turbulence of nearly 10% as the current density rises from 1 to 3 mA/m^2, however.

The turbulence generated by plate D appears to be a stronger function of bulk gas velocity than it is for any other electrode. Although turbulence production generally increases with current density, the peak level for plate D at 0.5 m/sec is 37% while it is only 5% at a bulk velocity of 2.0 m/sec.

A final note is that that the turbulence intensity curve for the wire electrodes at 1.0 m/sec actually drops between 1.5 mA/m^2 and 3.5 mA/m^2. This also occurs in the plate D curve at 2.0 m/sec (Figure 4.41) for current densities between 0.5 and 1.0 mA/m^2. The reason for this phenomenon is not clear.

4.2.6 Probability Density Functions

Probability density functions of the fluctuating portion of the streamwise velocity are presented in Figures 4.42 through 4.56. These plots provide an additional visual presentation of the magnitude of

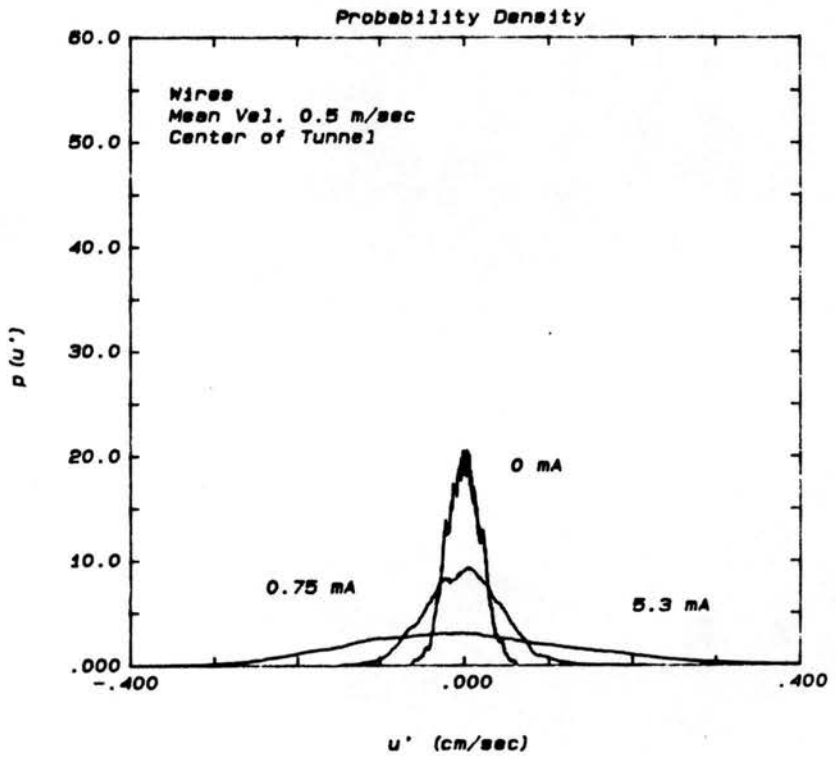

Figure 4.42. Probability density functions in wire-plate geometry at 0.5 m/s.

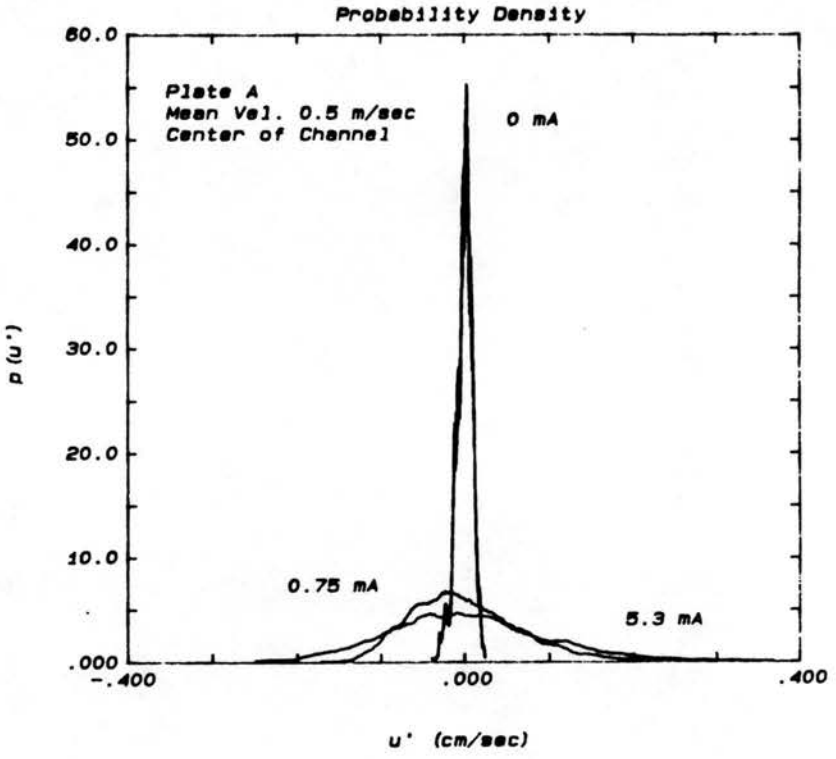

Figure 4.43. Probability density functions in plate A geometry at 0.5 m/s.

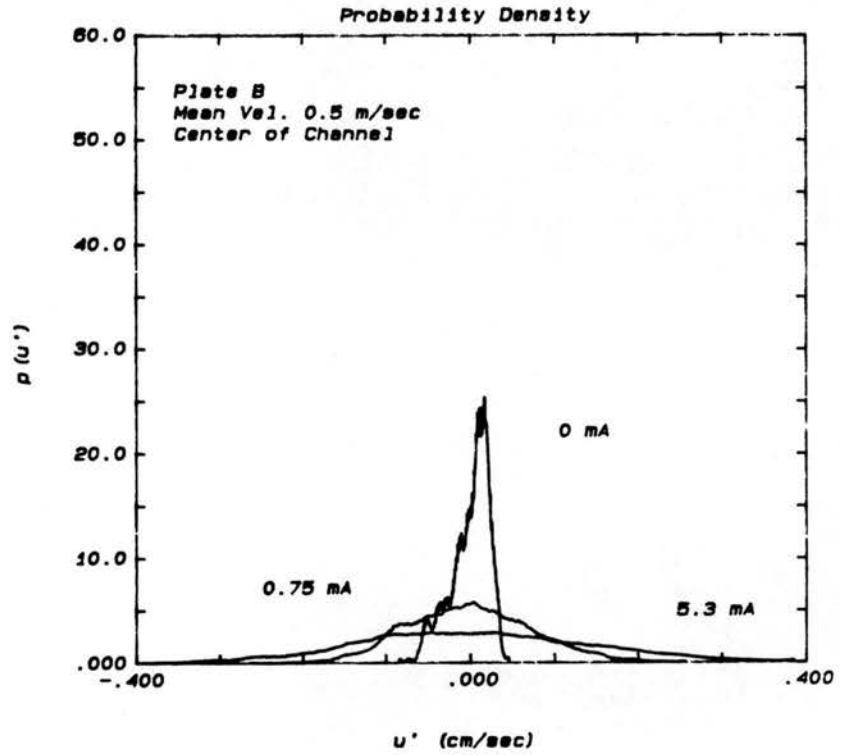

Figure 4.44. Probability density functions in plate B geometry at 0.5 m/s.

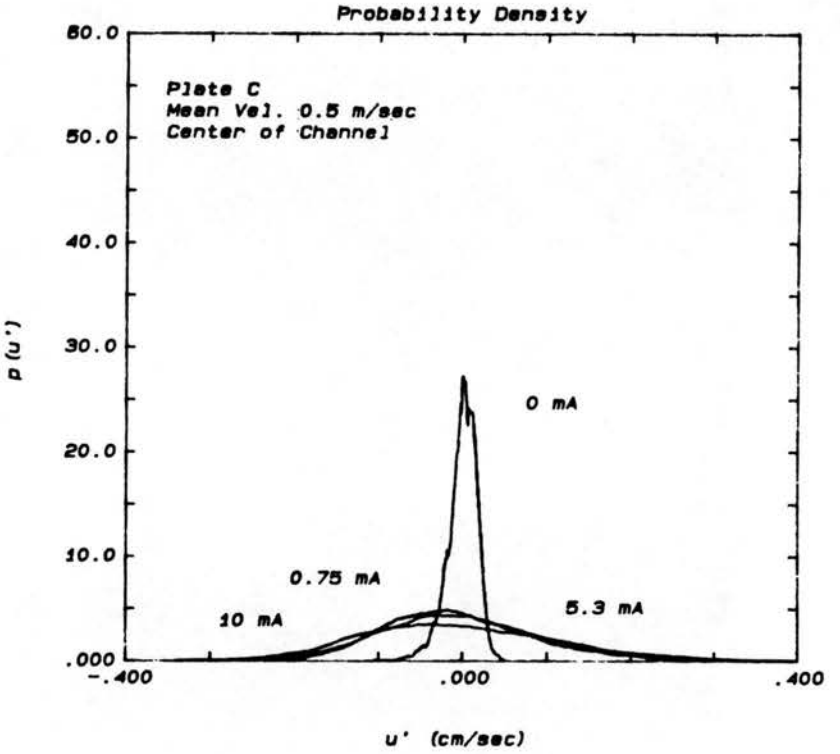

Figure 4.45. Probability density functions in plate C geometry at 0.5 m/s.

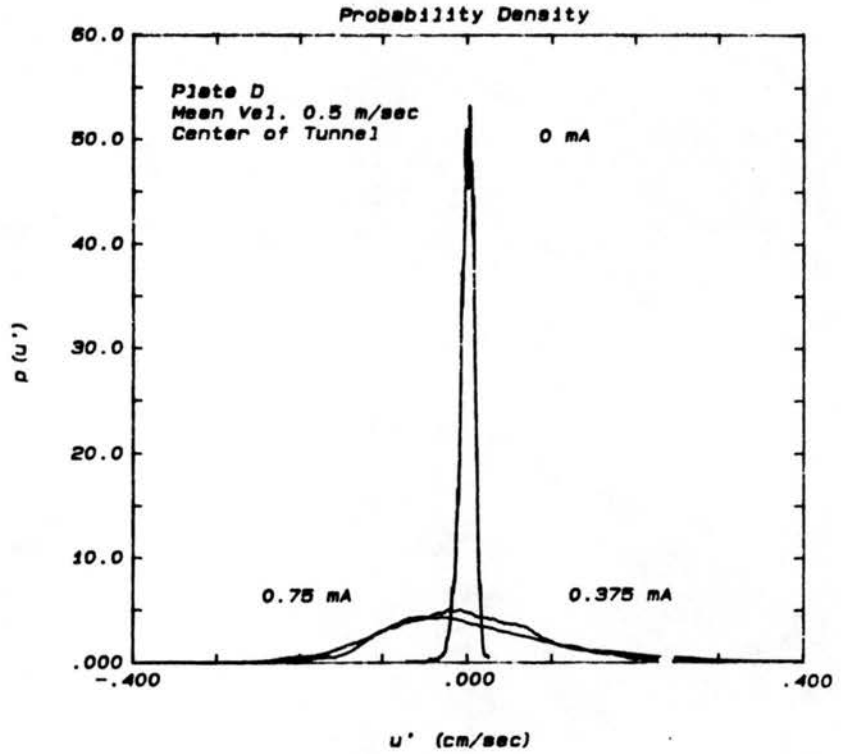

Figure 4.46. Probability density functions in plate D geometry at 0.5 m/s.

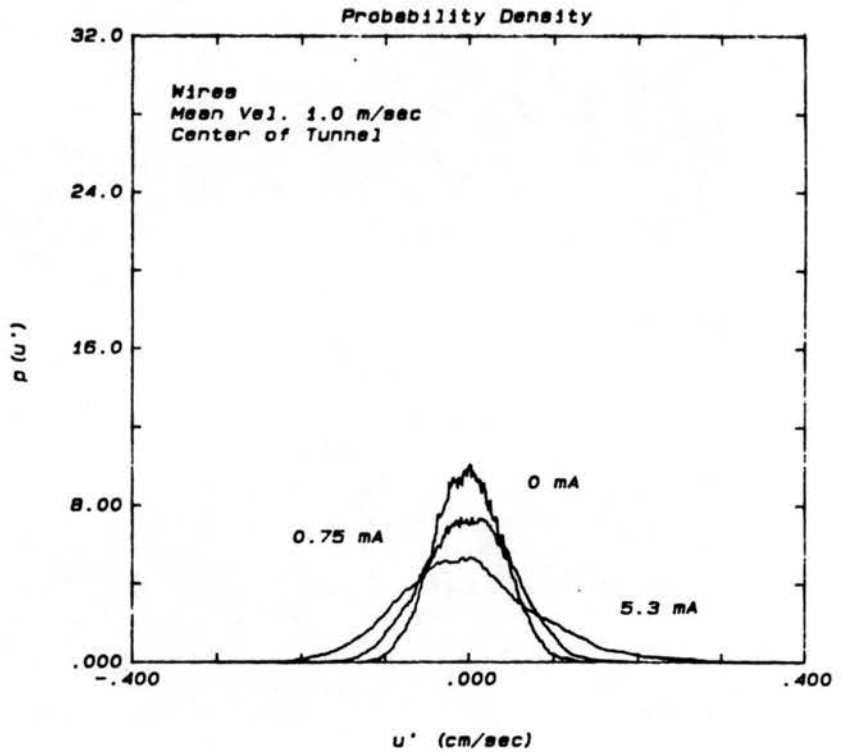

Figure 4.47. Probability density functions in wire-plate geometry at 1.0 m/s.

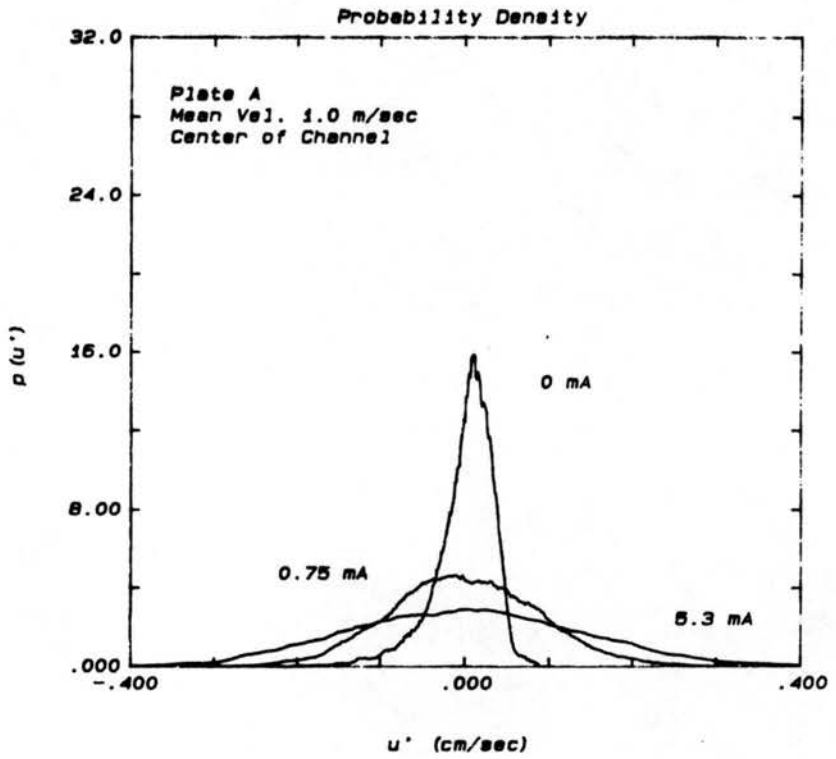

Figure 4.48. Probability density functions in plate A geometry at 1.0 m/s.

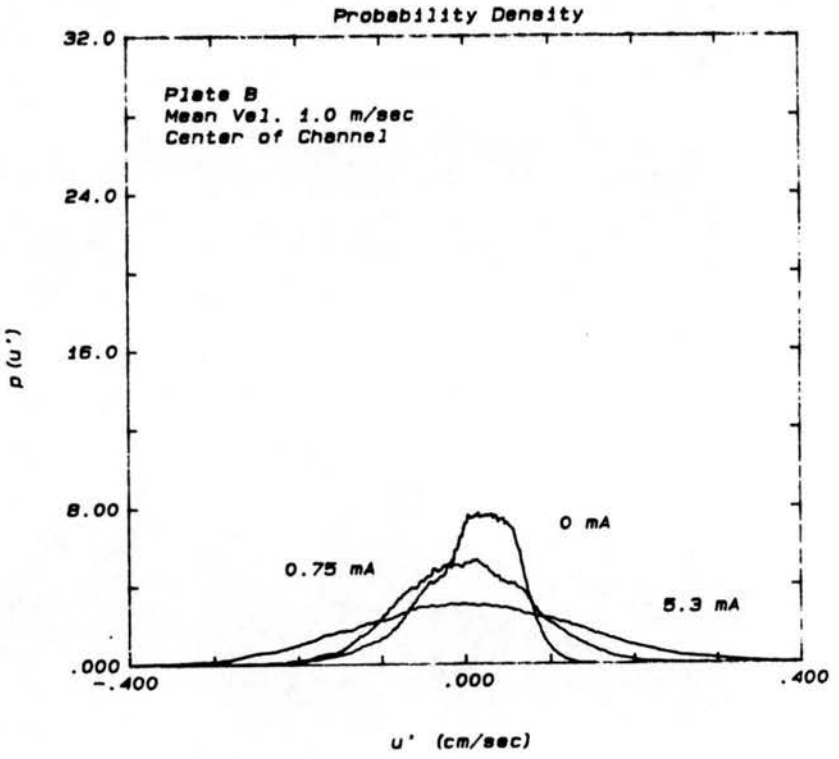

Figure 4.49. Probability density functions in plate B geometry at 1.0 m/s.

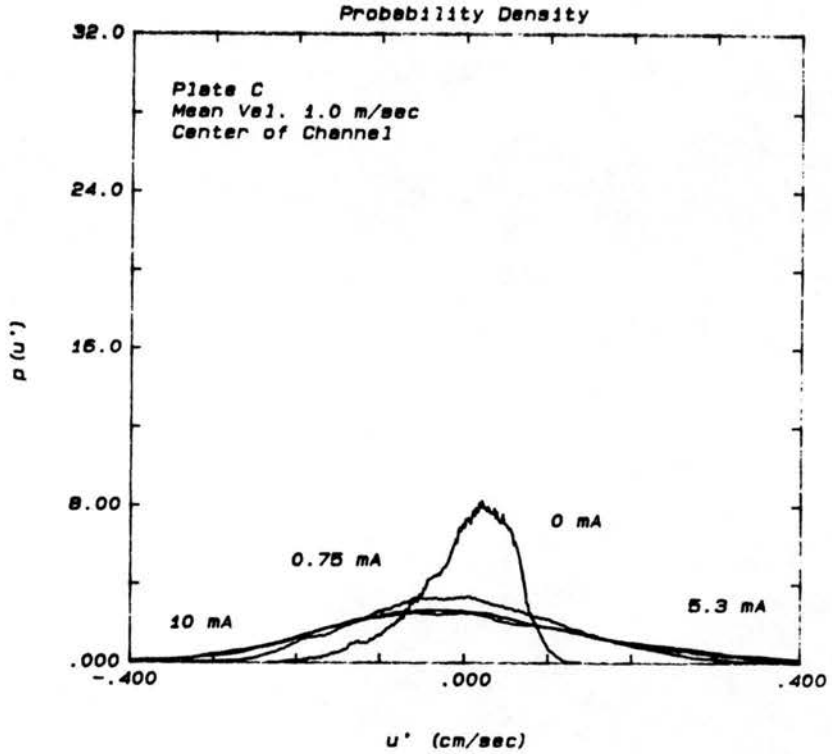

Figure 4.50. Probability density functions in plate C geometry at 1.0 m/s.

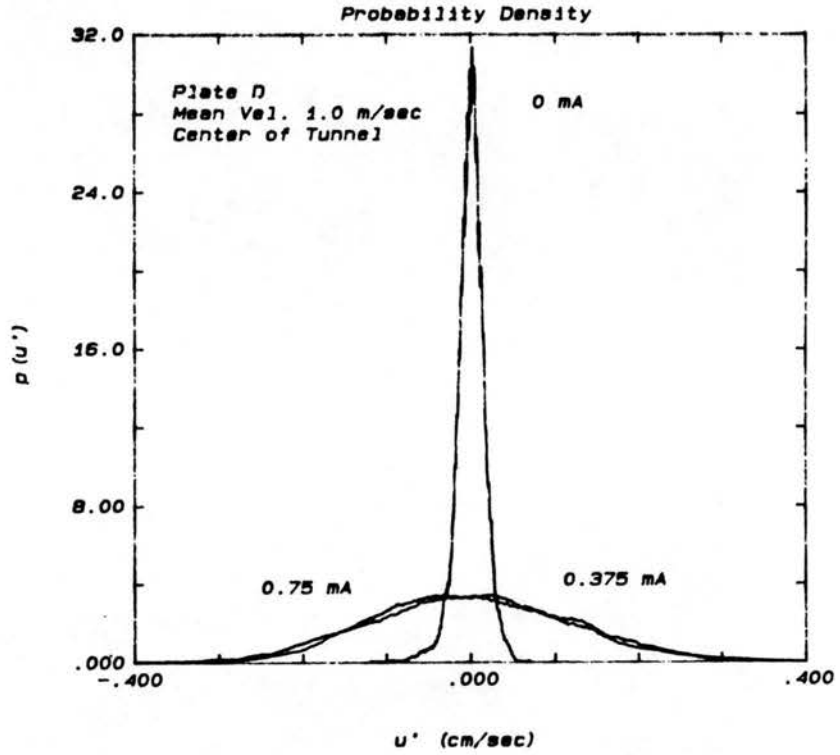

Figure 4.51. Probability density functions in plate D geometry at 1.0 m/s.

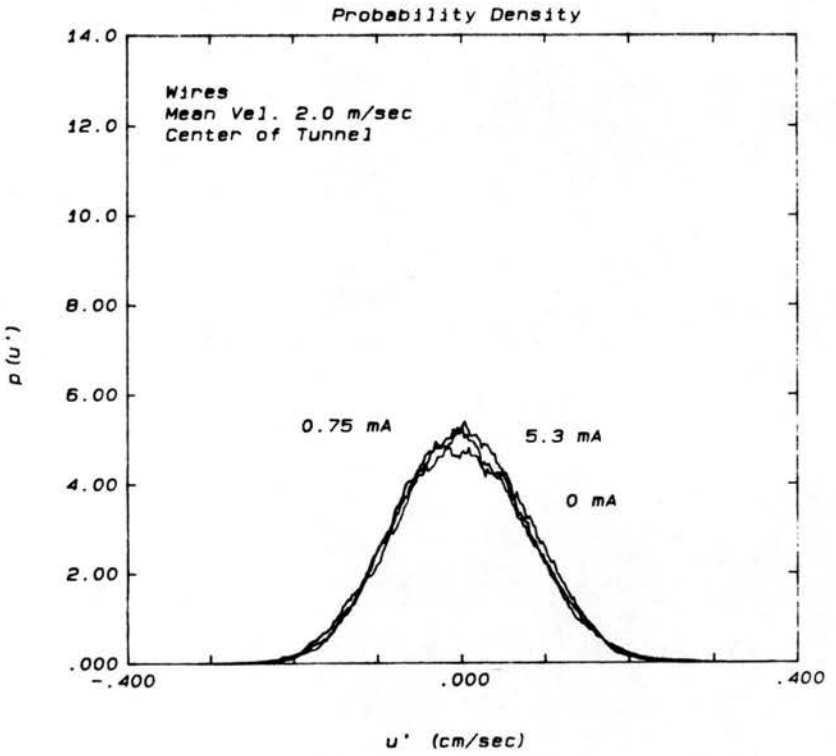

Figure 4.52. Probability density functions in wire-plate geometry at 2.0 m/s.

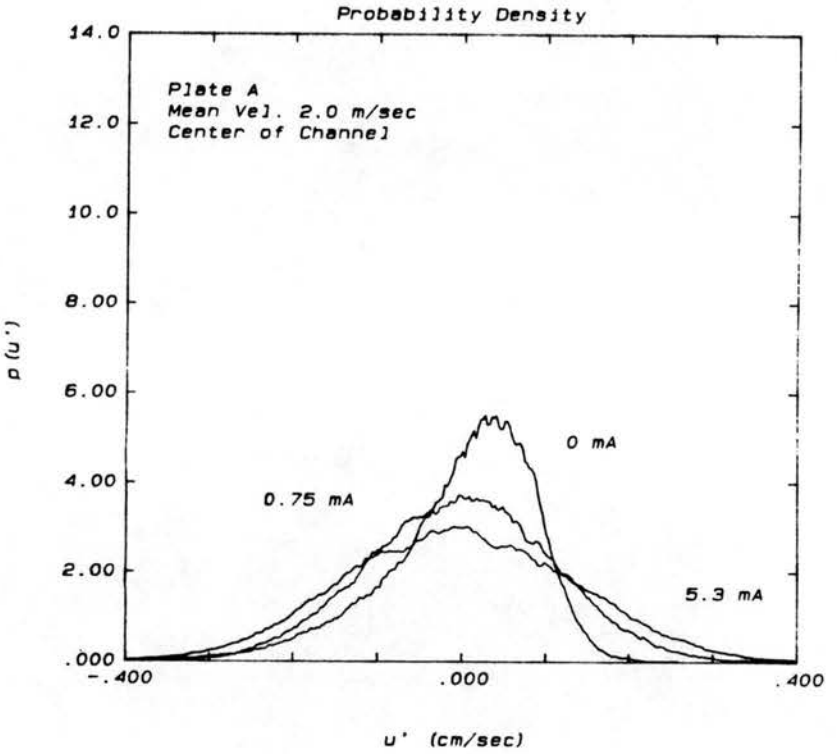

Figure 4.53. Probability density functions in plate A geometry at 2.0 m/s.

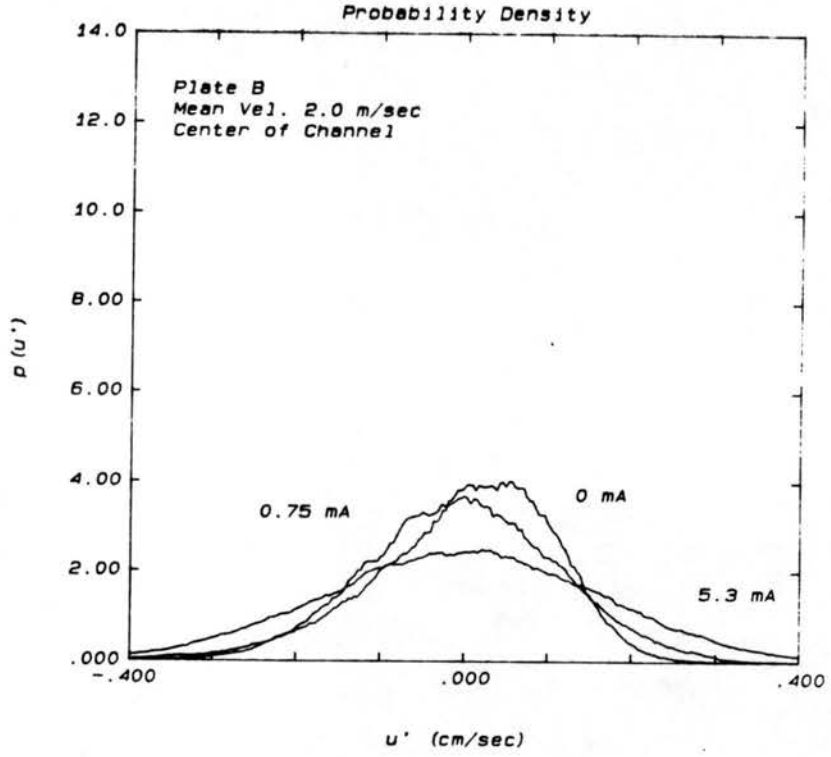

Figure 4.54. Probability density functions in plate B geometry at 2.0 m/s.

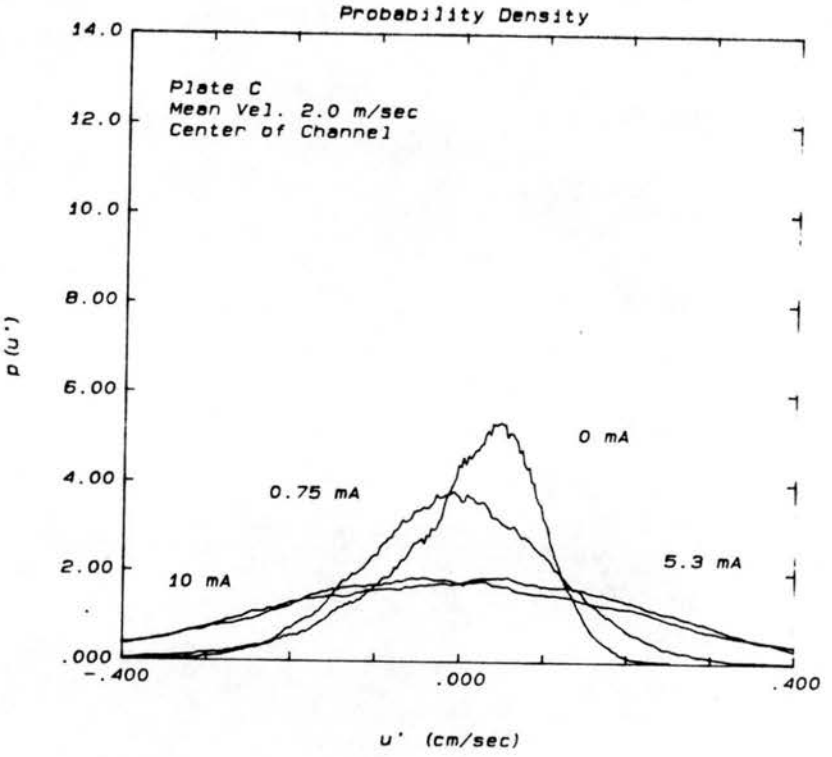

Figure 4.55. Probability density functions in plate C geometry at 2.0 m/s.

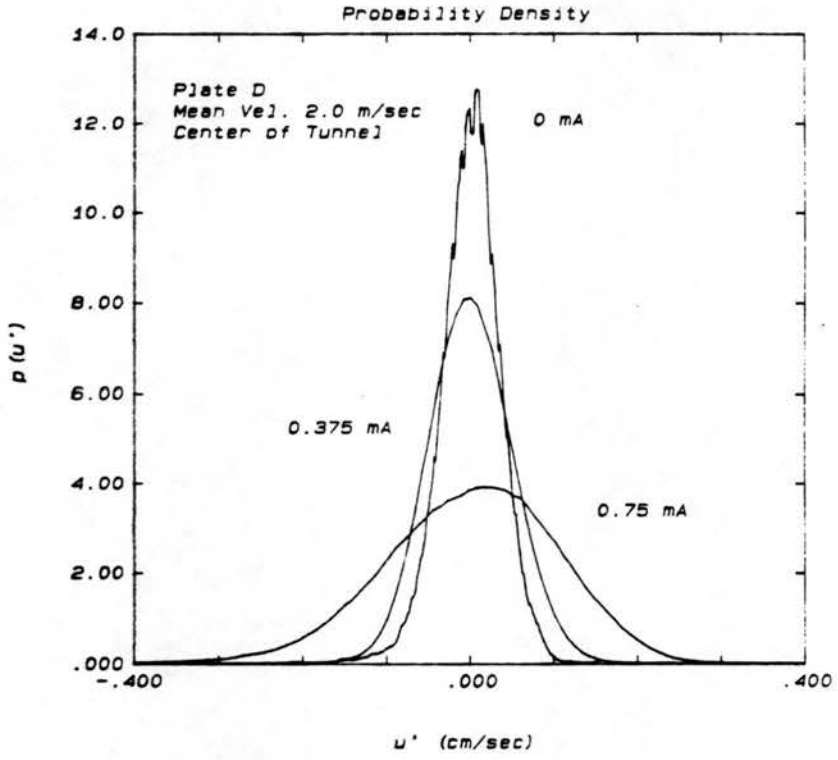

Figure 4.56. Probability density functions in plate D geometry at 2.0 m/s.

the turbulence in the precipitator. The width of the curve is a measure of turbulence production.

In examining Figures 4.42 through 4.46, which are the plots for a velocity of 0.5 m/sec, note that the no-current probability curves for both plate A and plate D are half as wide as those of the other electrodes, indicating much less turbulence. In the case of plate D this is most likely due to the fact that there is a wide channel with no obstruction in the center, as there is in the case of the wire electrodes. The measurements for all electrodes are made directly in the center of the channel (either full or half). For the wire electrodes this means that the measurements are made directly downstream of the wires themselves, which create a wake that could generate enough turbulence to widen the PDF curve somewhat. It is not clear why plate A also has a narrow no-current PDF, the fact that the barbs on plate A were aligned, while the barbs on plates B and C were offset (see Figure 3.7) may play a role.

Most noticeable beyond the no-current characteristics is that precipitator current appears to have a more gradual effect on PDF shape for the wire electrodes at low velocities than it does for the planar electrodes at low velocities. All "power on" PDF curves for the planar electrodes fall nearly on top of all other "power on" curves for that electrode. The trend reverses as bulk velocity increases, however. At 2.0 m/sec, initiating and increasing the precipitator current has no effect on the wire electrode PDF curve whatsoever. It does however create a marked effect in the planar electrode curves, particularly the full channel configuration of plate D as shown in Figure 4.56. This is particularly striking when it is noted that, due to a lack of available high voltage power, the highest

attainable current across the plate D configuration is just over 0.75 mA.

In general, the PDF curves agree very closely with the turbulence intensity plots presented earlier. For large electric numbers the width of the PDF, and thus the turbulence level is large. As the electric number is lowered, the width of the PDF and the turbulence intensity decrease.

A final note about the PDF curves is that there is a small skewness in some of the curves, particularly for plate A, B, and C. The indication is that there are occasional large scale excursions in the negative sense of the fluctuating velocity. This indicates that there is an intermittent flow phenomenon or secondary flow pattern creating an occasional velocity deficit at the hot-film probe. This is most probably a large scale circulation similar to that observed with the laser light sheet.

4.2.7 Power Spectra as a Function of Current

Figures 4.57 through 4.71 are power spectra of the fluctuating velocity measured at the channel center point. Each plot shows the power spectra for a particular electrode at several precipitator current levels and a given bulk gas velocity (0.5, 1.0, or 2.0 m/sec). The power spectrum is useful in determining the character or structure of a turbulent flow. Turbulent motion is generally characterized by a range of eddy sizes. The large scale eddies, which are responsible for the majority of the mixing and particle dispersion, are usually on the same order of magnitude as a bounding physical or characteristic dimension. The power spectrum, essentially a fourier transform of the time series fluctuating velocity of the flow, gives the frequency

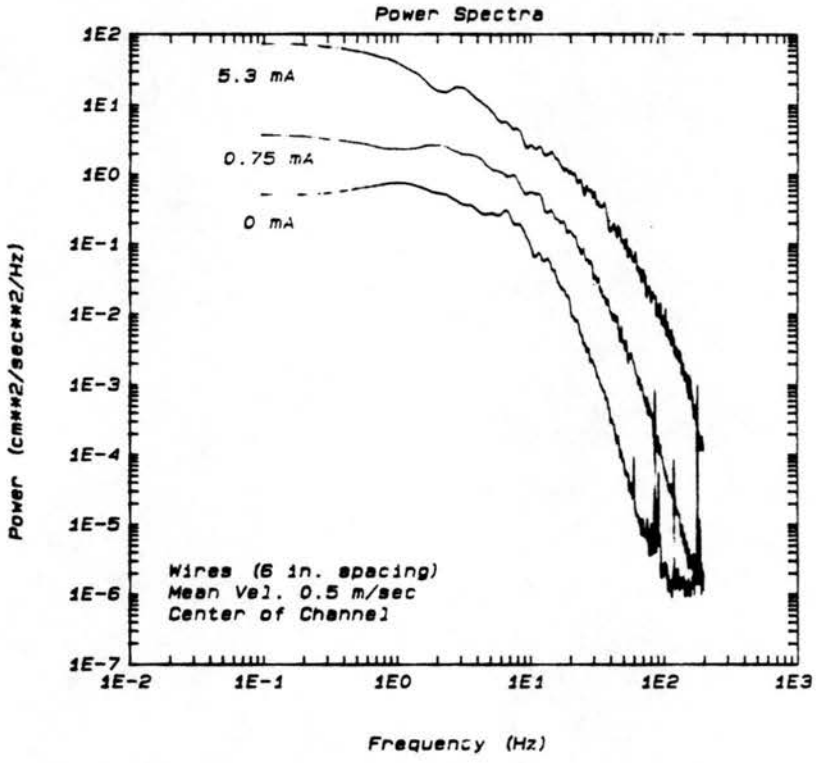

Figure 4.57. Power spectra in wire-plate geometry at 0.5 m/s.

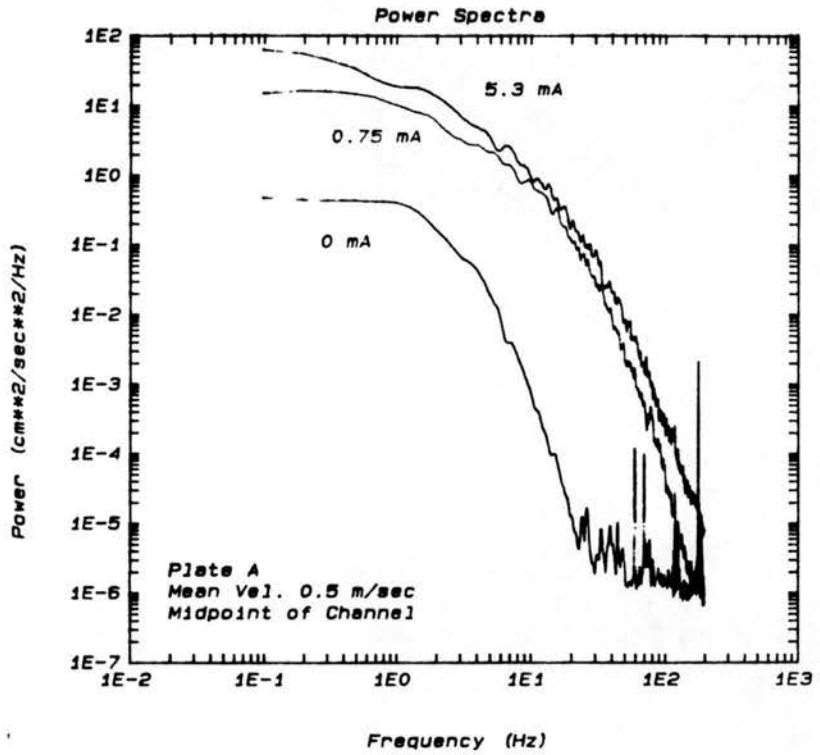

Figure 4.58. Power spectra in plate A geometry at 0.5 m/s.

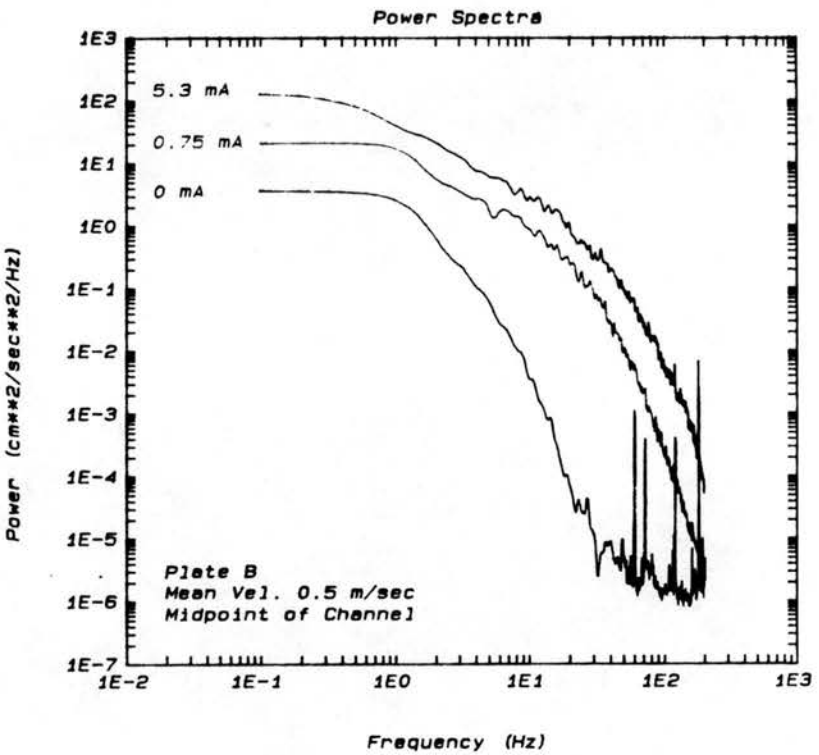

Figure 4.59. Power spectra in plate B geometry at 0.5 m/s.

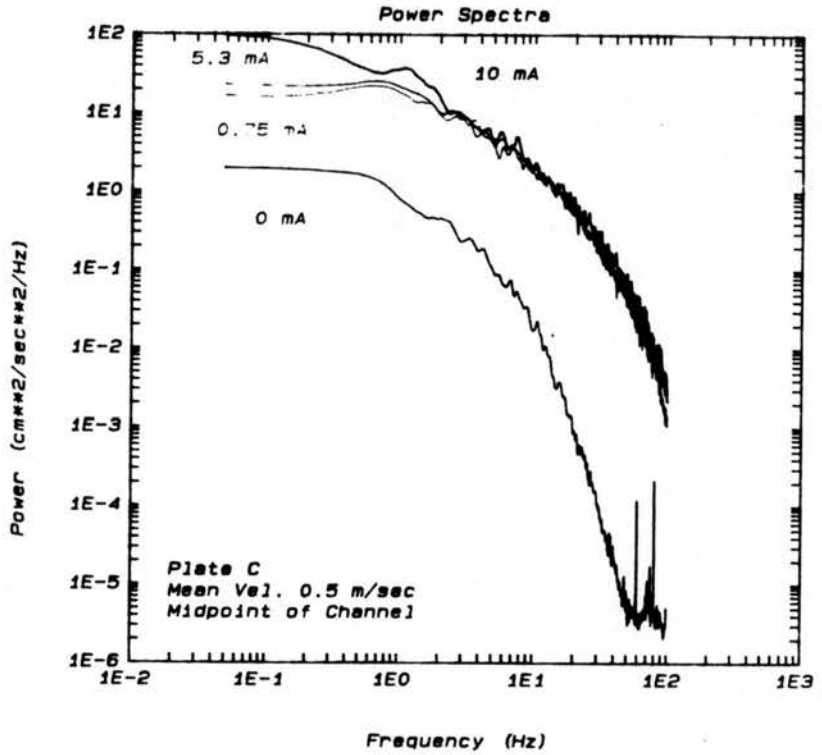

Figure 4.60. Power spectra in plate C geometry at 0.5 m/s.

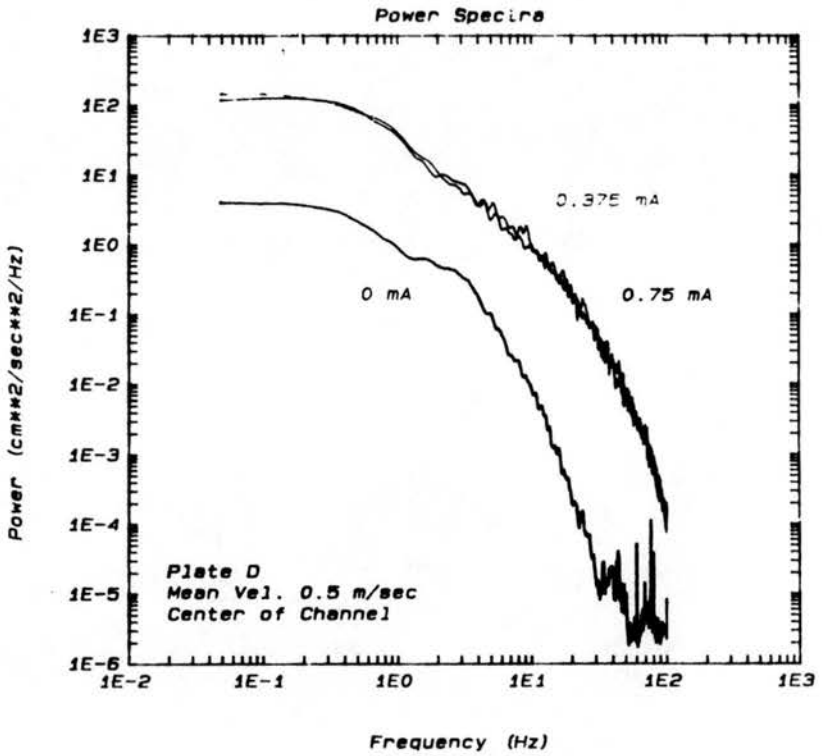

Figure 4.61. Power spectra in plate D geometry at 0.5 m/s.

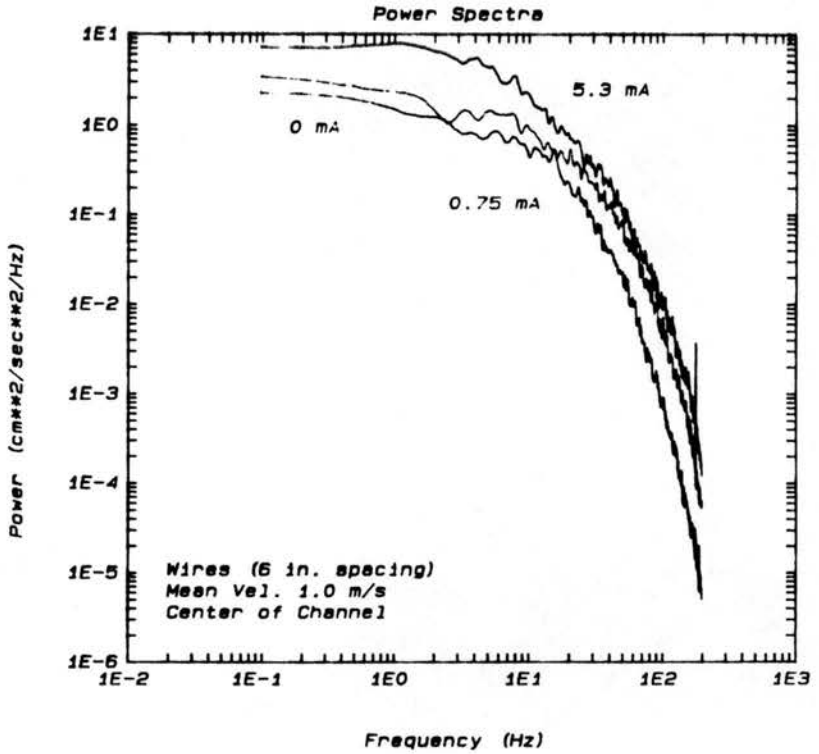

Figure 4.62. Power spectra in wire-plate geometry at 1.0 m/s.

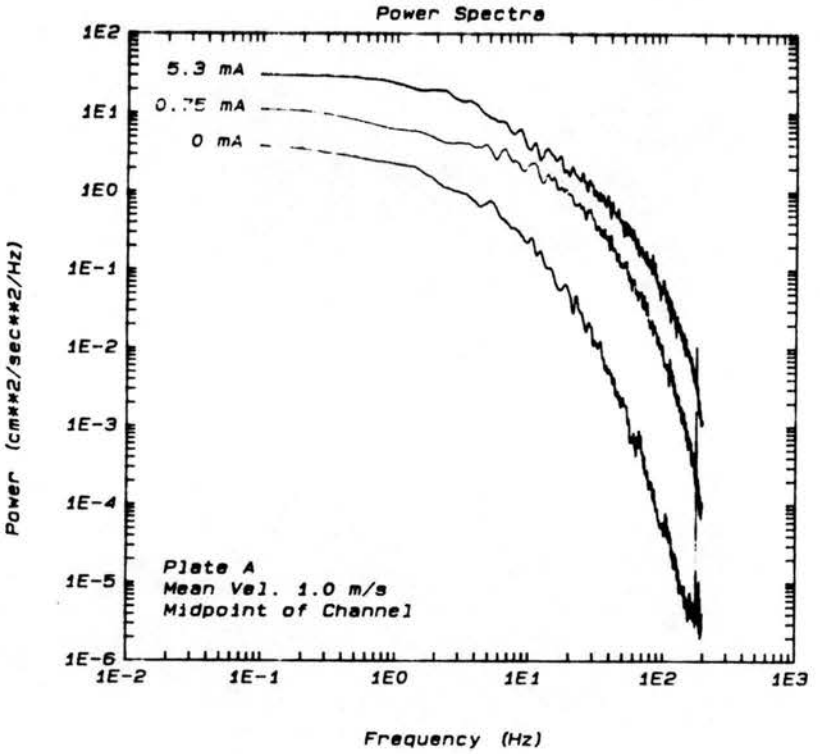

Figure 4.63. Power spectra in plate A geometry at 1.0 m/s.

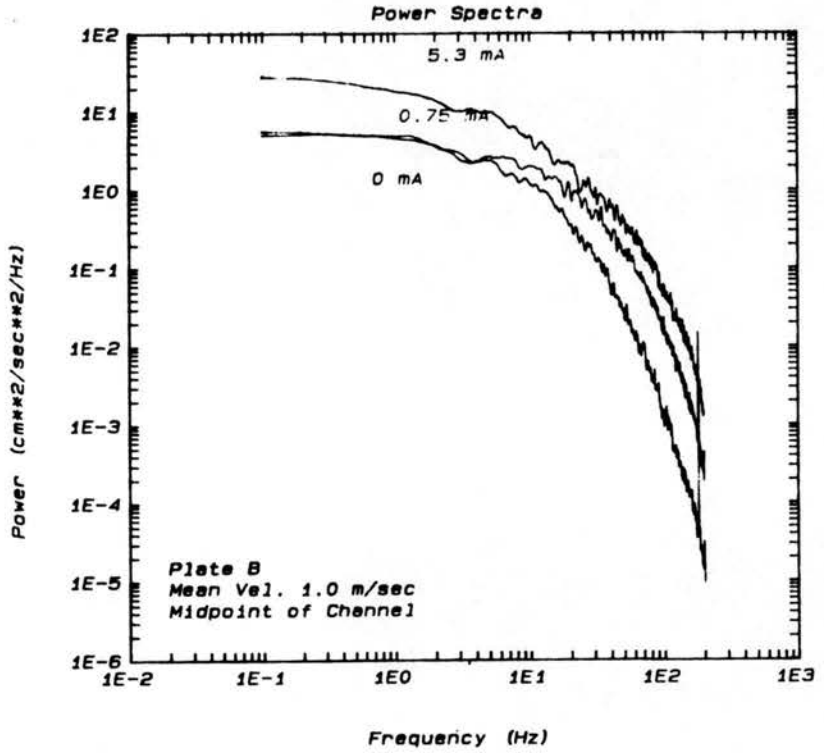

Figure 4.64. Power spectra in plate B geometry at 1.0 m/s.

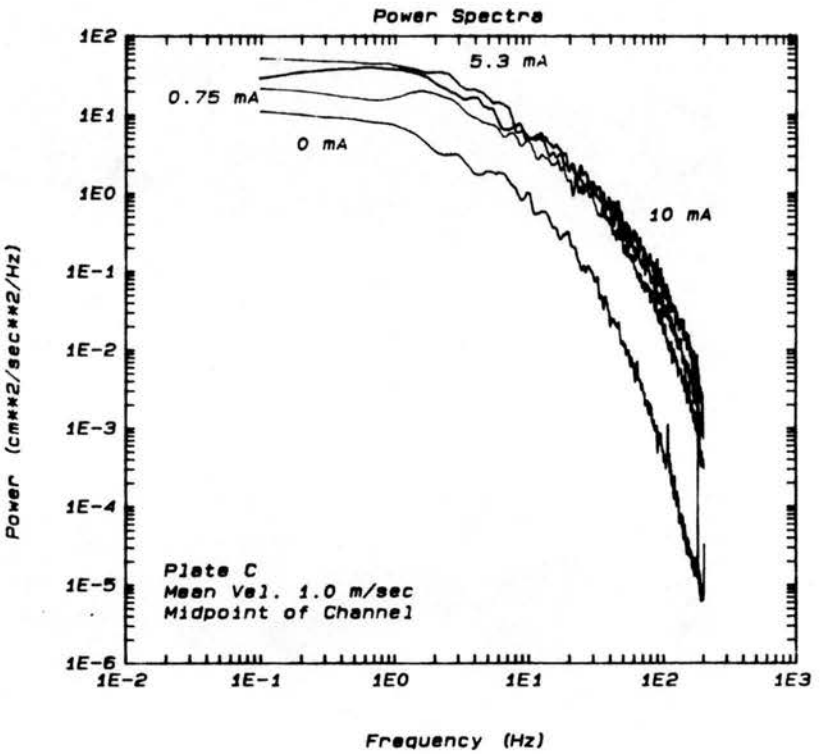

Figure 4.65. Power spectra in plate C geometry at 1.0 m/s.

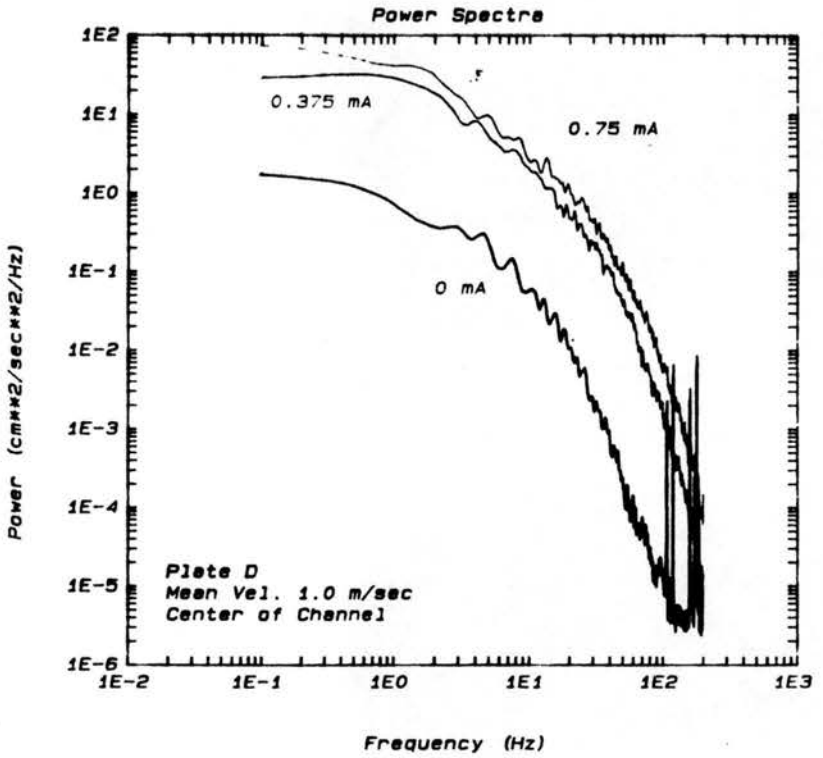

Figure 4.66. Power spectra in plate D geometry at 1.0 m/s.

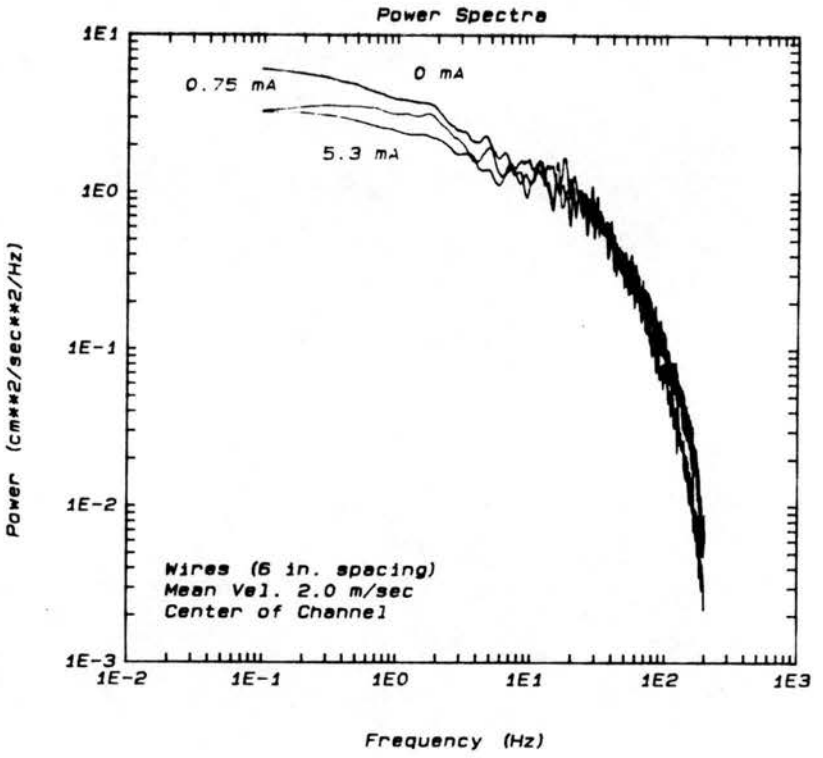

Figure 4.67. Power spectra in wire-plate geometry at 2.0 m/s.

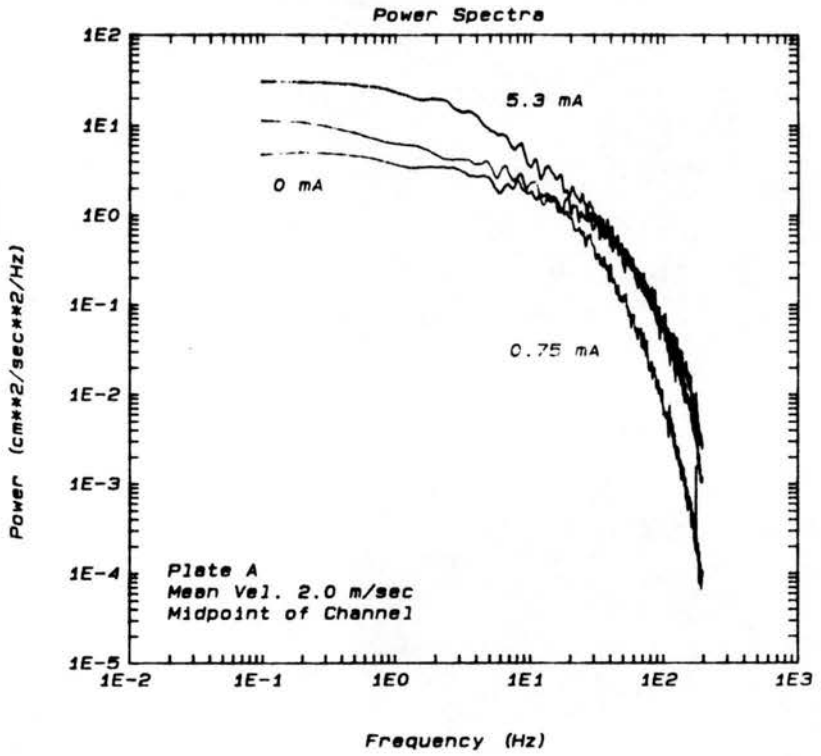

Figure 4.68. Power spectra in plate A geometry at 2.0 m/s.

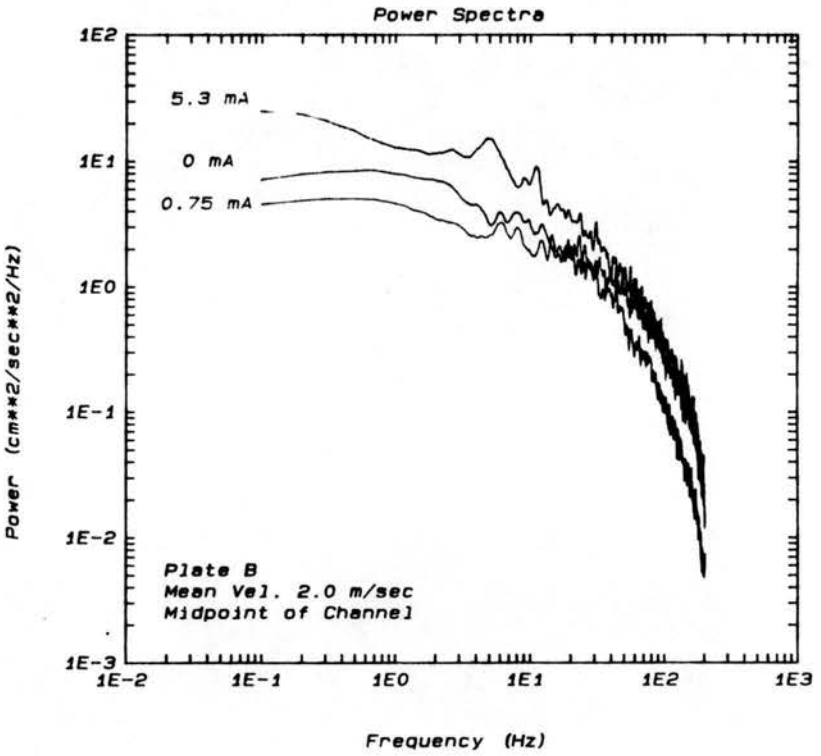

Figure 4.69. Power spectra in plate B geometry at 2.0 m/s.

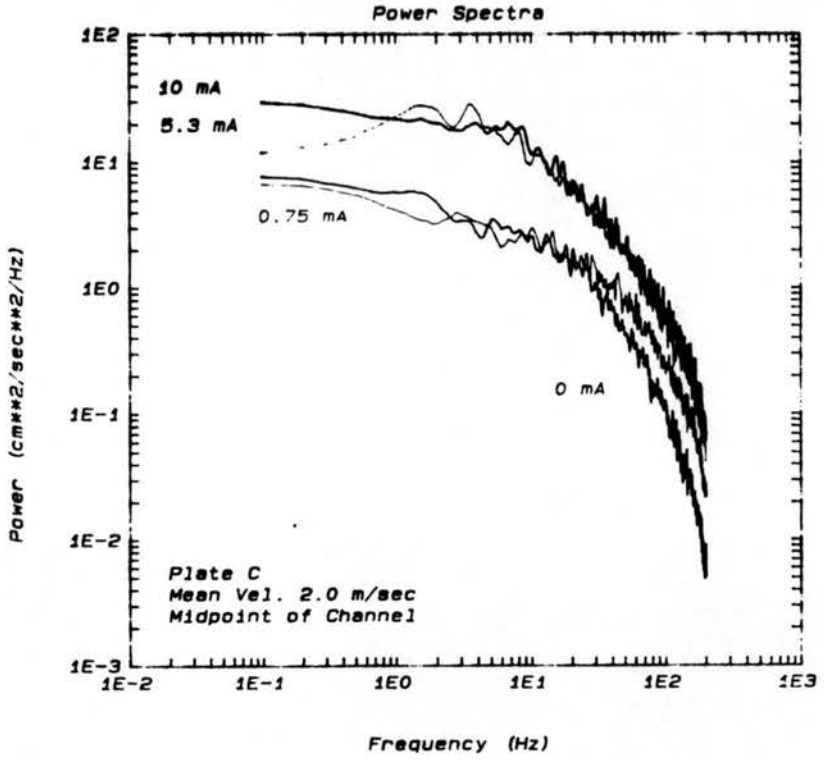

Figure 4.70. Power spectra in plate C geometry at 2.0 m/s.

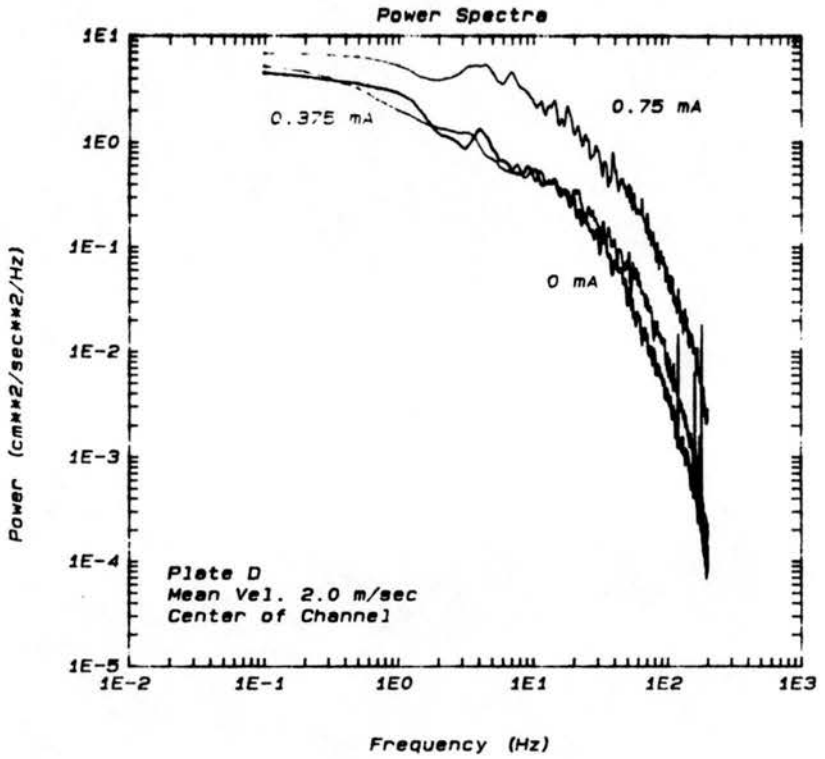

Figure 4.71. Power spectra in plate D geometry at 2.0 m/s.

distribution of the mean square fluctuations in that flow. Large scale eddies are represented as low frequency fluctuations, while the smaller eddies show up as high frequencies. Thus, the power spectrum serves as a tool in determining the character of the turbulence being studied.

Examination of all power spectra plots yields the general observation that there is always an increase in total power (and thus turbulence) for an increase in current. The corona discharge creates additional energy at all frequency levels with no apparent preferred frequency or eddy size. The increase in power is always more significant at low frequencies than at higher frequencies, indicating that the electric body force produces relatively large scale turbulence. The usual one-dimensional spectrum of turbulence exhibits more low frequency power than high frequency power, some of which is due to aliasing. The power generation due to an increase in precipitator current does not significantly change the shape of the spectrum, it merely elevates it. The spectrum elevation is generally visually proportional on the log scale, and is therefore most significant at lower current levels, particularly at gas speeds of 0.5 and 1.0 m/sec.

Aside from the general observations, there are a few particular comments to be made about these curves. At bulk gas speeds of 0.5 and 1.0 m/sec, spectra for the wire-plate geometry as well as plates A and B are further elevated for each increase in precipitator current, as shown in Figures 4.57 through 4.69 and Figures 4.62 through 4.64. This is not true for any electrode at a bulk velocity of 2.0 m/sec, nor is it true for plates C and D at any bulk velocity. The spectra for plates C and D are elevated substantially upon corona onset

(Figures 4.60, 4.61, 4.64, and 4.65) but are not elevated further at higher currents. The reason for this in the case of plate D may simply be a lack of high voltage power. The 1.0 kW supply used in these tests cannot generate the voltage needed to sustain a current level much greater than 0.75 mA for plate D. Thus, nothing is known about its characteristics at higher current levels. In the case of plate C, the reason for the lack of spectral power increase may be that the corona structure set up initially does not change substantially as the current is increased. That is, no new barbs develop a discharge as more current is allowed to flow. Rather, the previously discharging barbs carry more current and merely maintain the already existing secondary flow pattern.

4.2.8 Effect of Geometry on Power Spectra

Power Spectra for all electrodes at a given current density (0, 0.67, and 4.75 mA/m^2) and bulk gas velocity (0.5, 1.0, and 2.0 m/sec) are presented in Figures 4.72 through 4.80. These are the same curves plotted in the figures presented above (Figures 4.57 through 4.71), but presented so that the characteristics of electrodes may be more easily compared. The extra low frequency information in the curves for plates C and D in Figures 4.72, 4.75, and 4.78 was obtained by sampling at a lower rate (200 Hz) since the high frequency content of the spectra at 0.5 m/sec was simply noise.

Spectra in the absence of a corona discharge, Figures 4.72, 4.73, and 4.74, suggest that aerodynamic turbulence generated by the half-channel planar electrode geometry (plates A, B, and C) is generally greater then the full channel geometries (wire-plate and plate D). An

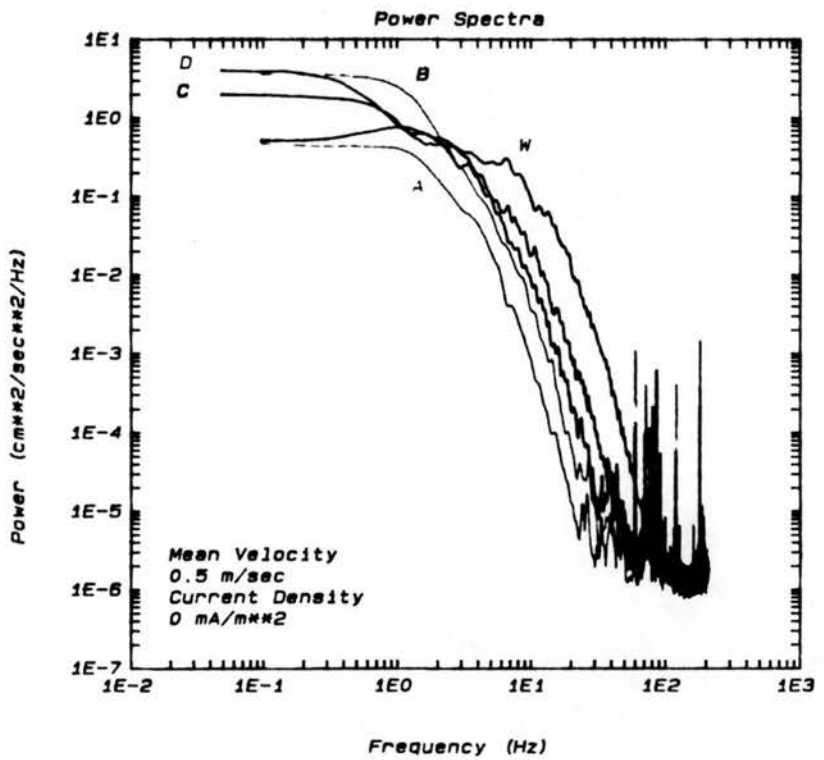

Figure 4.72. Power spectra at 0 mA/m^2 and 0.5 m/s of all electrode geometries.

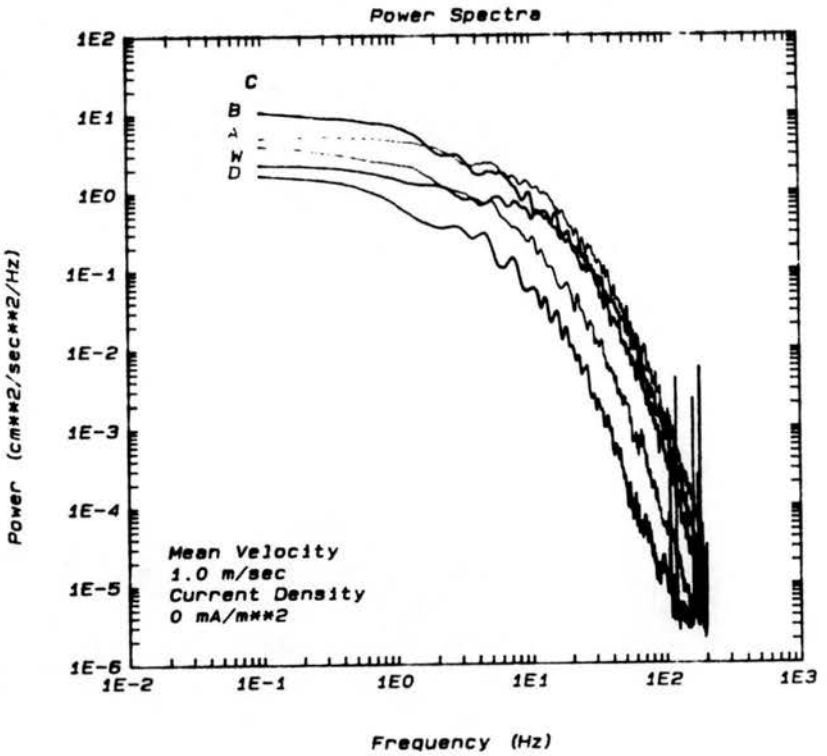

Figure 4.73. Power spectra at 0 mA/m^2 and 1.0 m/s of all electrode geometries.

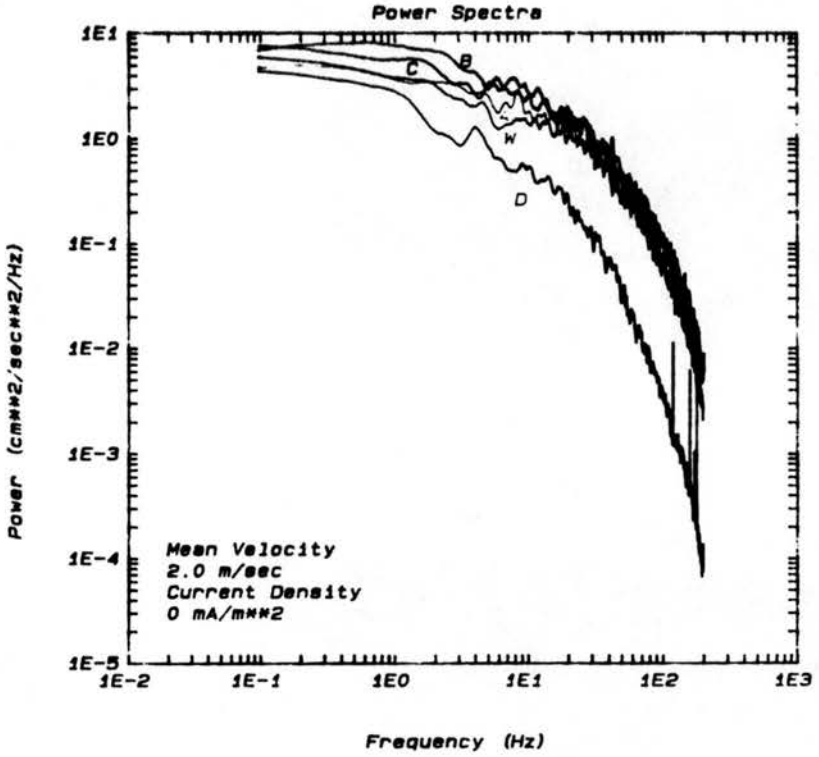

Figure 4.74. Power spectra at 0 mA/m^2 and 2.0 m/s of all electrode geometries.

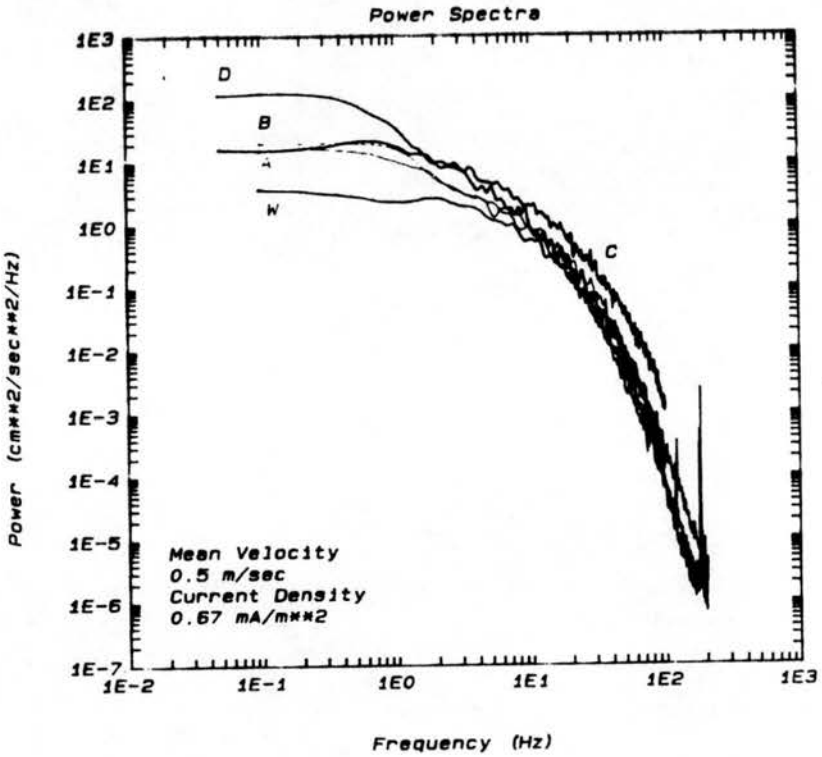

Figure 4.75. Power spectra at 0.67 mA/m^2 and 0.5 m/s of all electrode geometries.

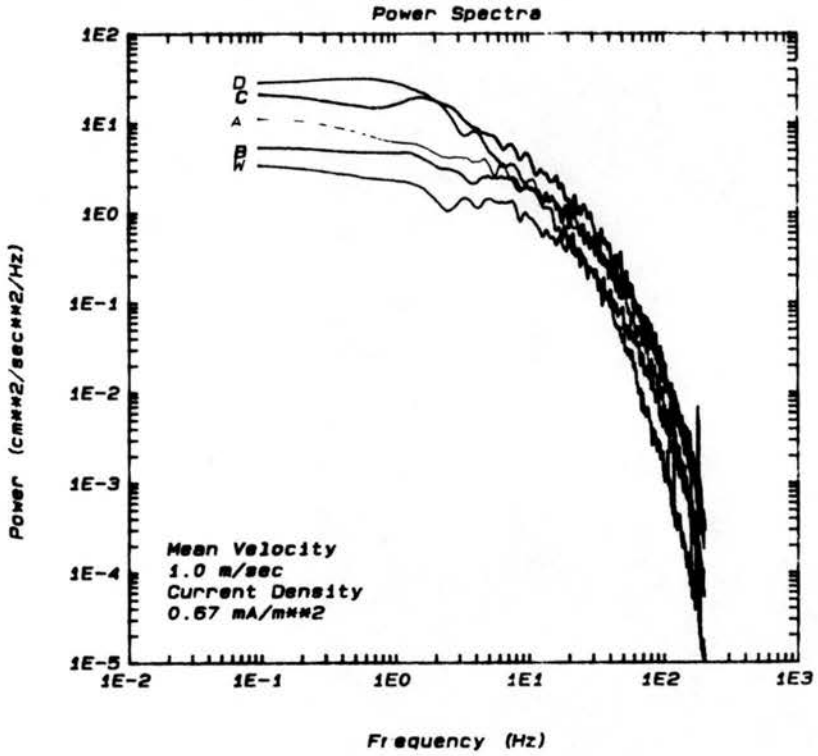

Figure 4.76. Power spectra at 0.67 mA/m^2 and 1.0 m/s of all electrode geometries.

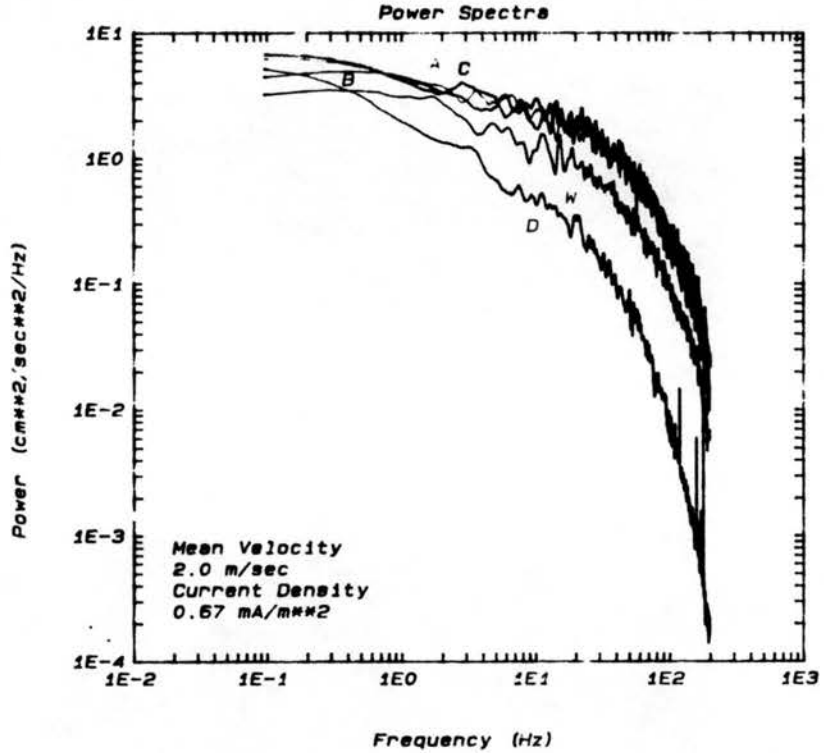

Figure 4.77. Power spectra at 0.67 mA/m^2 and 2.0 m/s of all electrode geometries.

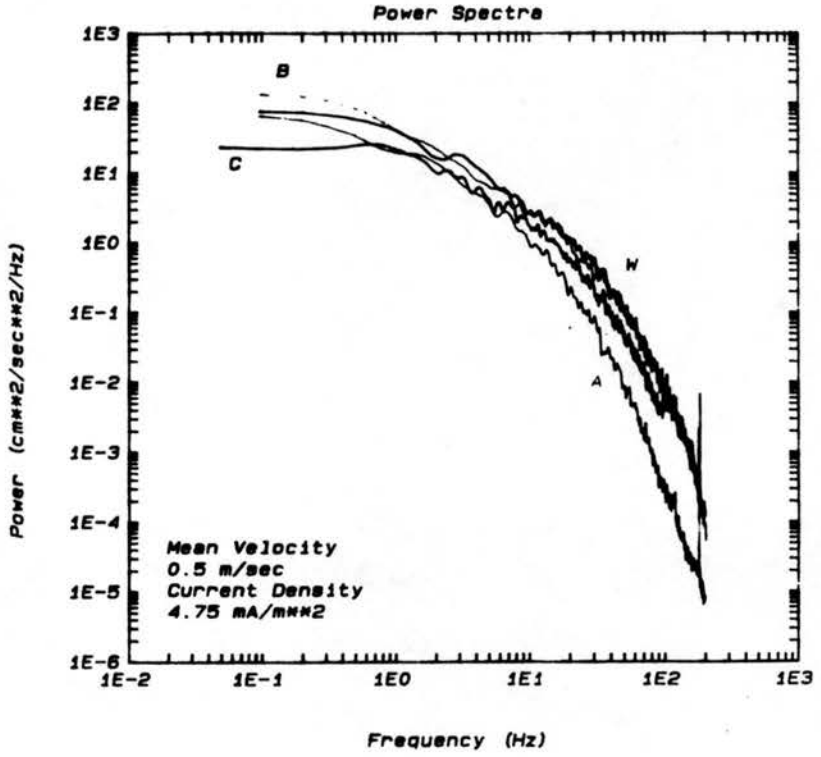

Figure 4.78. Power spectra at 4.75 mA/m^2 and 0.5 m/s of all electrode geometries.

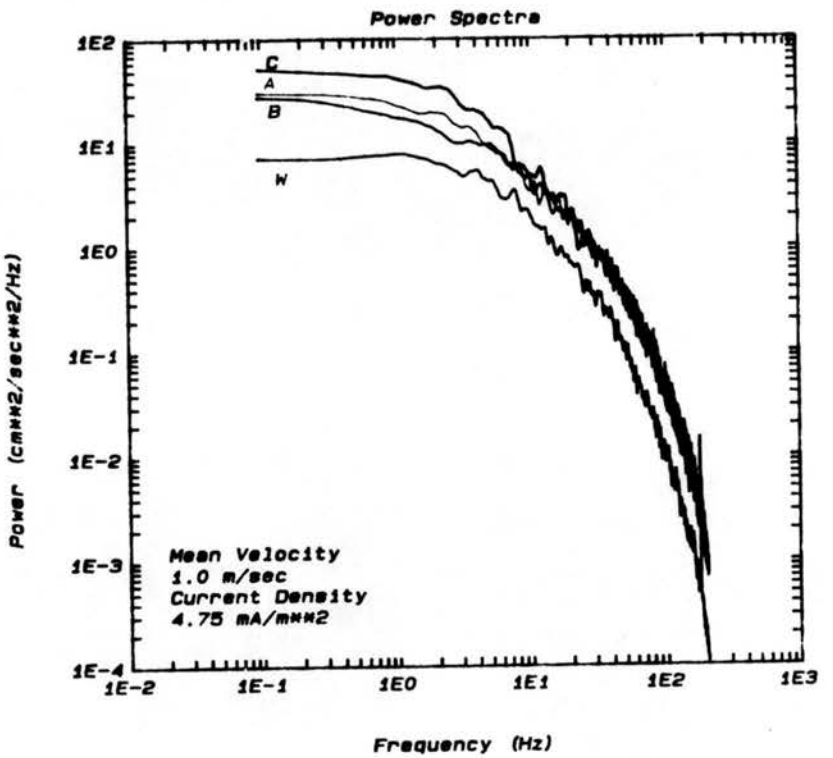

Figure 4.79. Power spectra at 4.75 mA/m^2 and 1.0 m/s of all electrode geometries.

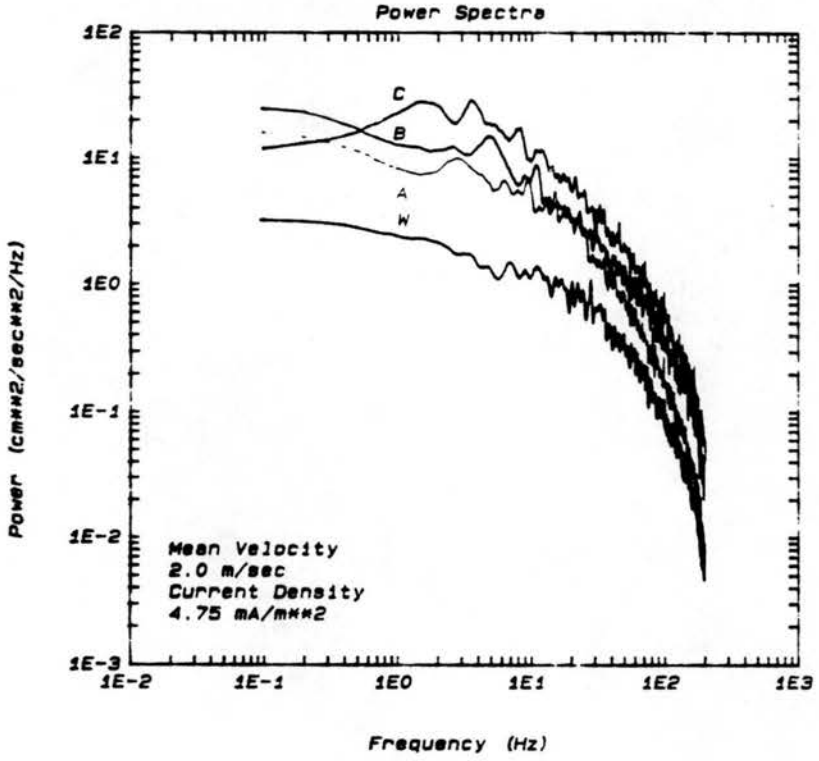

Figure 4.80. Power spectra at 4.75 mA/m^2 and 2.0 m/s of all electrode geometries.

exception to this, shown in Figure 4.72, is when at a bulk velocity of 0.5 m/sec, the plate A half-channel geometry produces less energy at all frequencies than any other geometry. Under the same conditions the wire-plate geometry appears to produce a much greater amount of high frequency energy. This effect is most likely caused by the hot-film probe being in the wake of the wires. At a bulk velocity of 1.0 m/sec (Figure 4.73) this effect is lessened and at 2.0 m/sec (Figure 4.74) it no longer persists.

Introduction of the corona discharge significantly changes the spectrum of each electrode, each to a different degree, as shown in Figures 4.75 through 4.77. At a current density of 0.67 mA/m^2 plate C produces a larger amount of energy than almost all other electrodes, particularly at higher frequencies. For the same electrical conditions, plate D in the full-channel configuration, produces a disproportionately large amount of low frequency energy at all gas velocities. A current density of 0.67 mA/m^2, plate D generates the most low frequency energy at a bulk gas velocity of 0.5 m/sec (Figure 4.75) and the least high frequency energy at a velocity of 2.0 m/sec, as shown in Figure 4.77. At a bulk velocity of 1.0 m/sec (Figure 4.76) plate D produces the most low frequency energy and the least high frequency energy. This effect is most likely a function of strong secondary flows observed with the laser light sheet at the leading and trailing edges of the plate. These large scale circulation zones are most likely caused by the presence of the Plexiglas wall at the upstream and downstream edges of the plate and are not representative of the EHD flow in the discharge region. For all flow velocities at a current density of 0.67 mA/m^2 the wire-plate

geometry generates the least amount of energy over the entire spectrum in almost all instances.

Figures 4.78, 4.79, and 4.80 are similar to Figures 4.75 through 4.77, but at a current density of 4.75 mA/m^2. Spectra for the full-channel geometry (plate D) are not plotted because the power supply used is not able to produce 4.75 mA/m^2 in the full-channel configuration. Once again these plots confirm the turbulence intensity measurements. The corona discharge planar geometries produce significantly high turbulence levels than does the wire discharge. This is particularly true at 2.0 m/sec. In this case the wire discharge produces no additional turbulence over that of the background flow whereas the plate discharge does have a marked effect on turbulence levels.

4.2.9 Normalized Power Spectra as a Function of Current

Figures 4.81 through 4.95 are the normalized power spectra of the fluctuating velocity measured at the channel centerline. These plots are identical to the spectra in Figures 4.57 through 4.71 except that each data point has been divided by the mean square velocity prior to plotting in order to normalize the curves to unit power. In this way, the magnitude of the induced turbulence is removed from the spectra and the spectral shapes are easily compared.

The data of Figures 4.81 through 4.95 indicate that the structure of turbulence is significantly changed by the electric body force only at low gas speeds (0.5 and 1.0 m/sec). The corona-on normalized spectra have more high frequency content than the no-current base case. This holds true for all electrode geometries but is most significant in the case of the planar electrodes. There is no

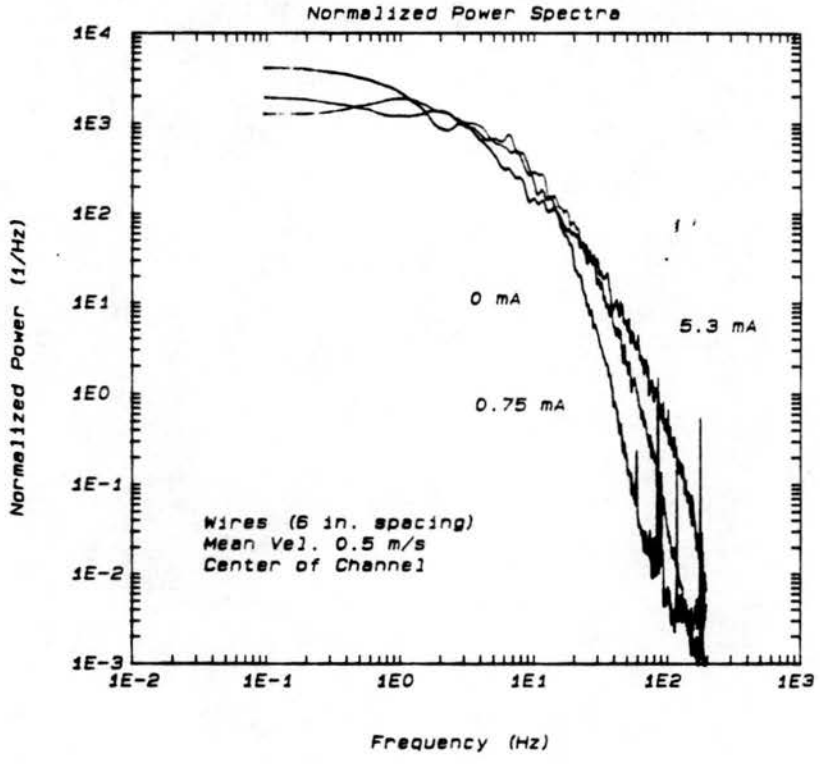

Figure 4.81. Normalized power spectra in wire-plate geometry at 0.5 m/s.

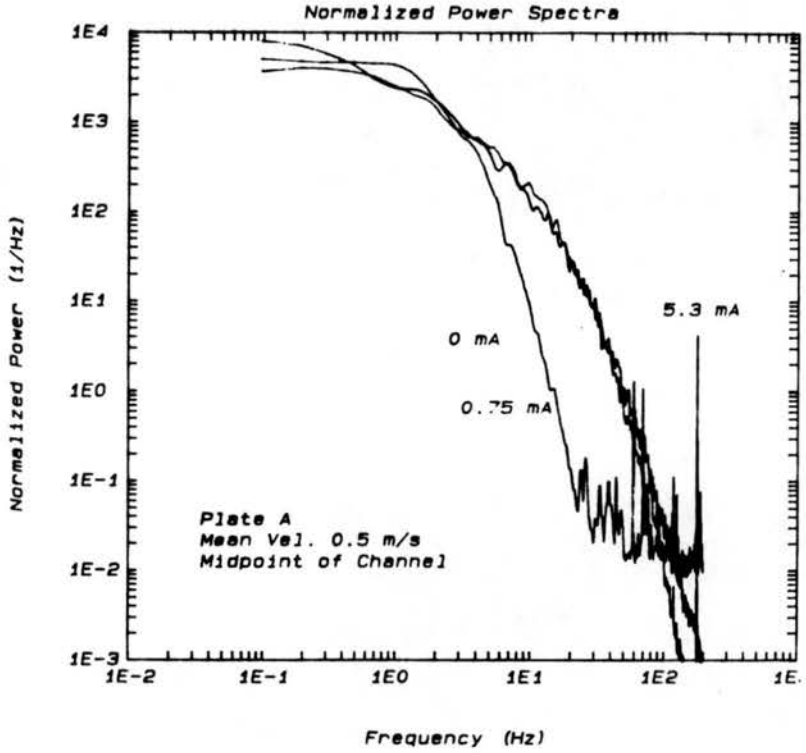

Figure 4.82. Normalized power spectra in plate A geometry at 0.5 m/s.

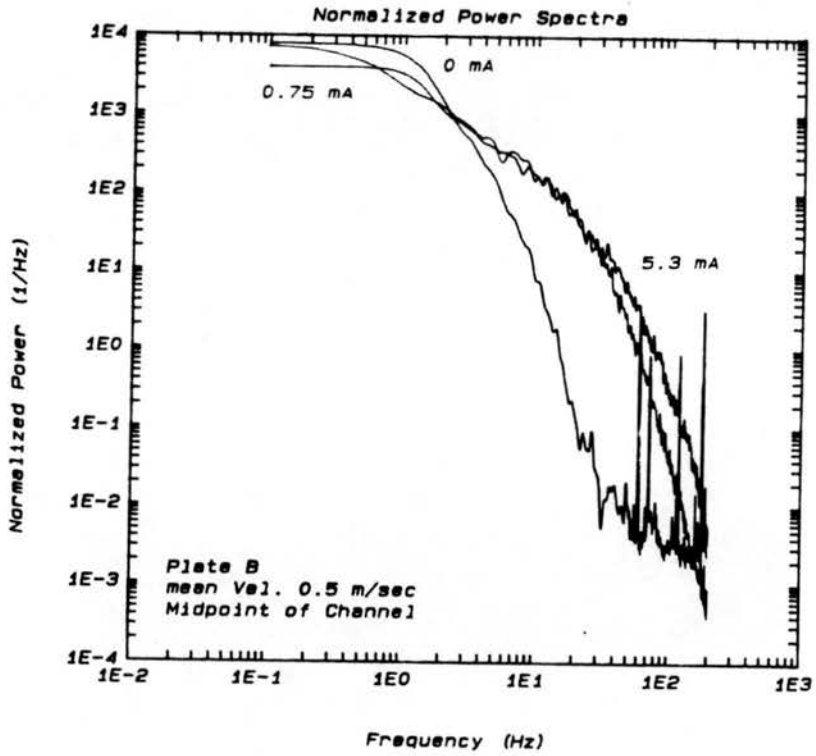

Figure 4.83. Normalized power spectra in plate B geometry at 0.5 m/s.

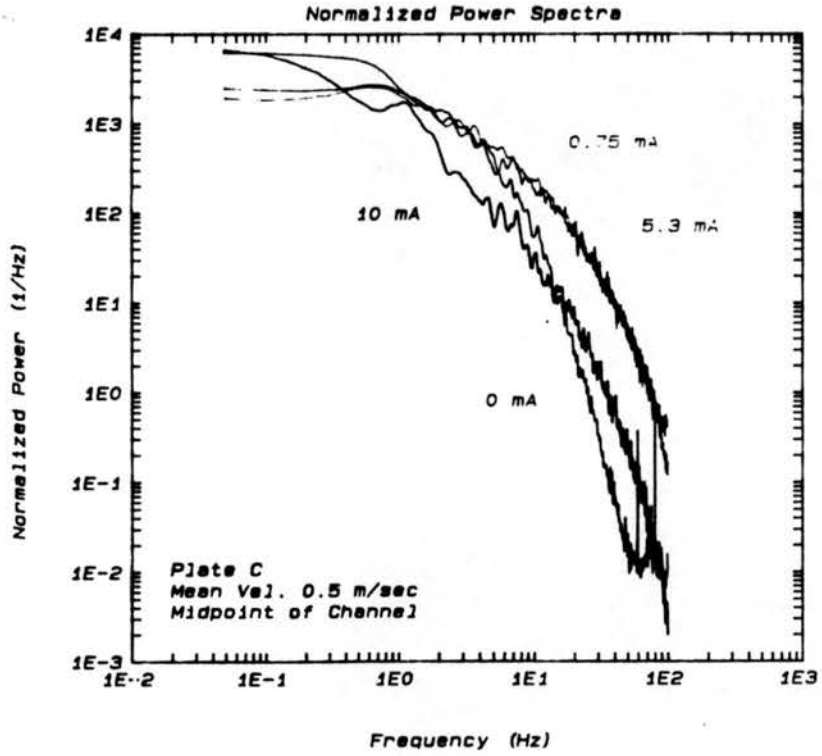

Figure 4.84. Normalized power spectra in plate C geometry at 0.5 m/s.

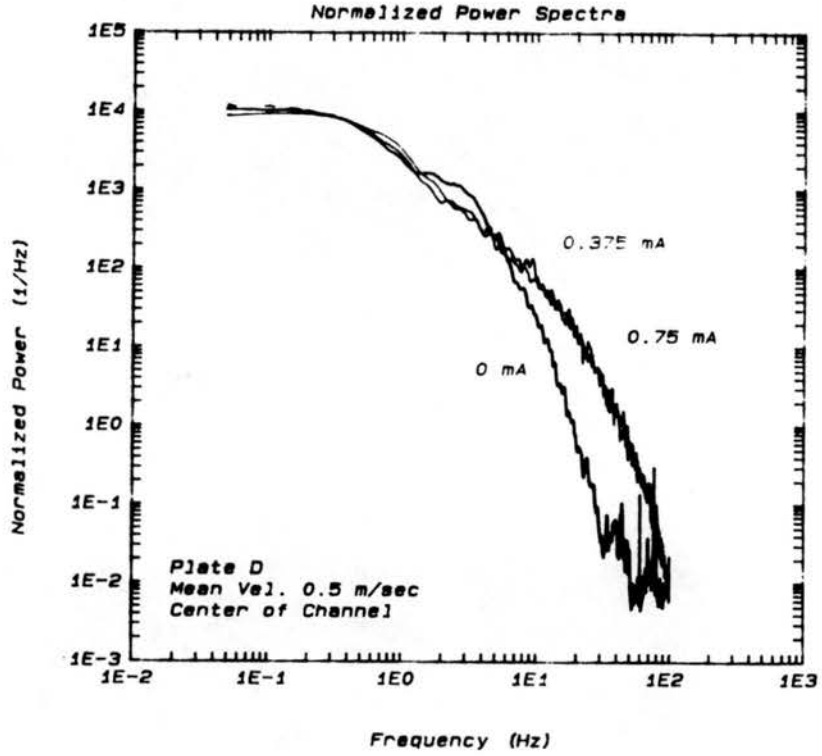

Figure 4.85. Normalized power spectra in plate D geometry at 0.5 m/s.

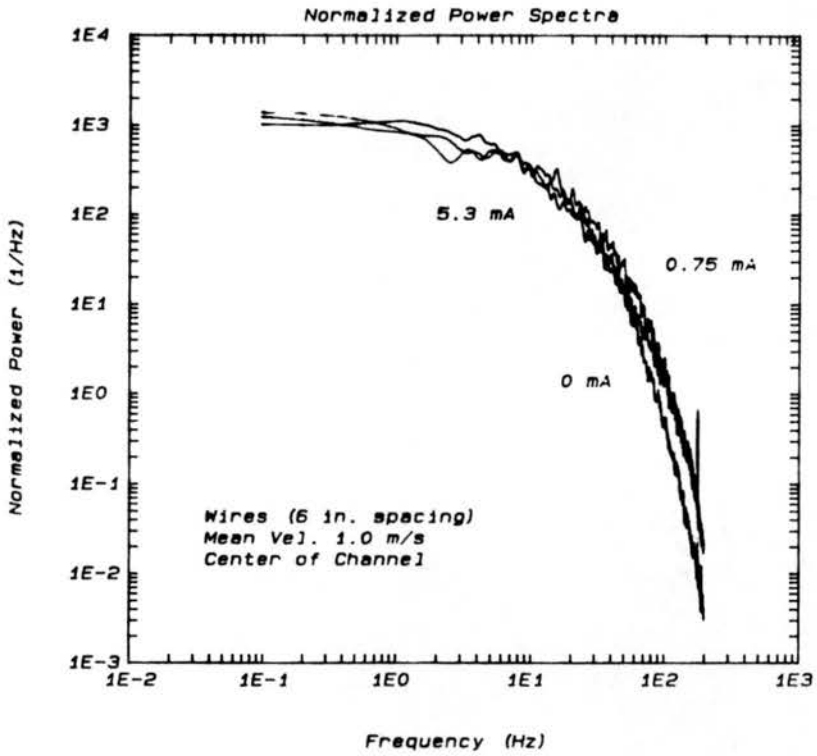

Figure 4.86. Normalized power spectra in wire-plate geometry at 1.0 m/s.

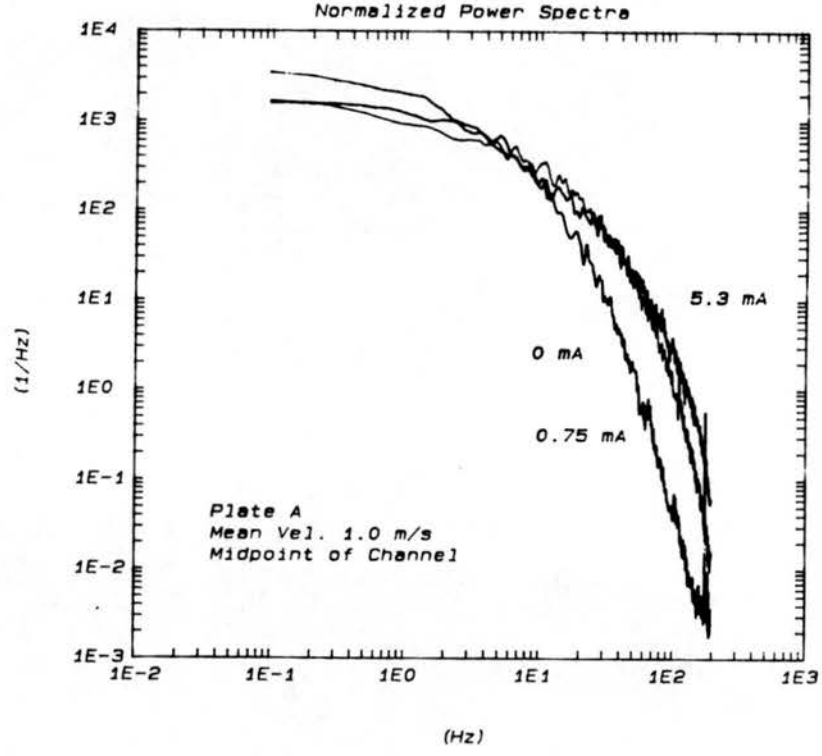

Figure 4.87. Normalized power spectra in plate A geometry at 1.0 m/s.

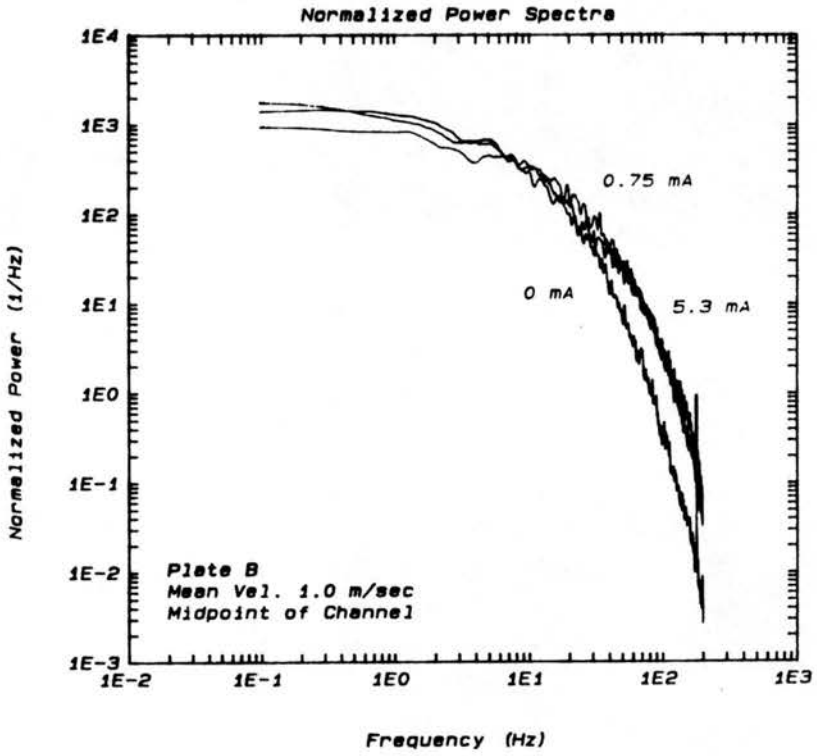

Figure 4.88. Normalized power spectra in plate B geometry at 1.0 m/s.

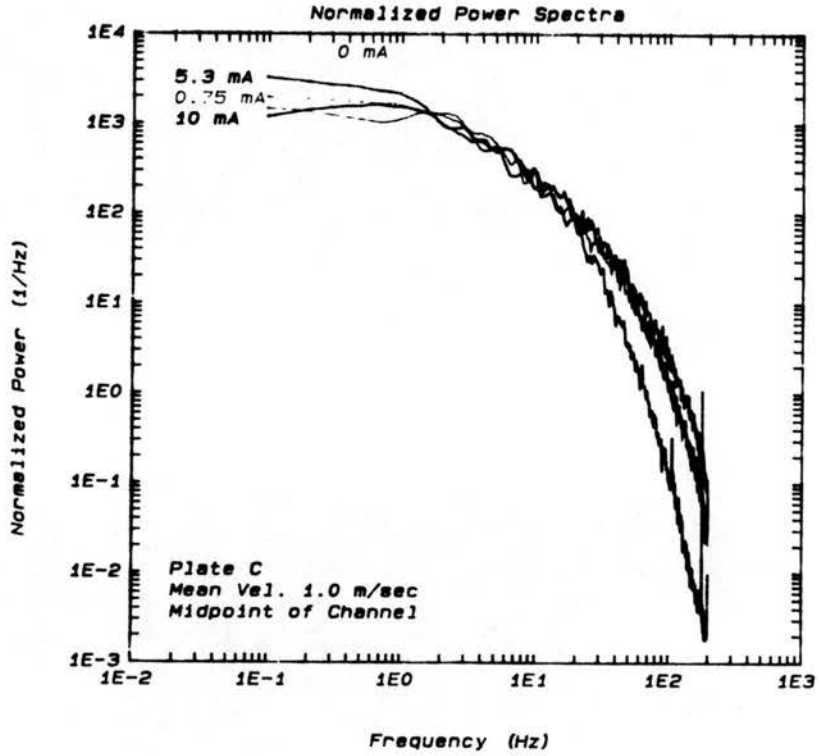

Figure 4.89. Normalized power spectra in plate C geometry at 1.0 m/s.

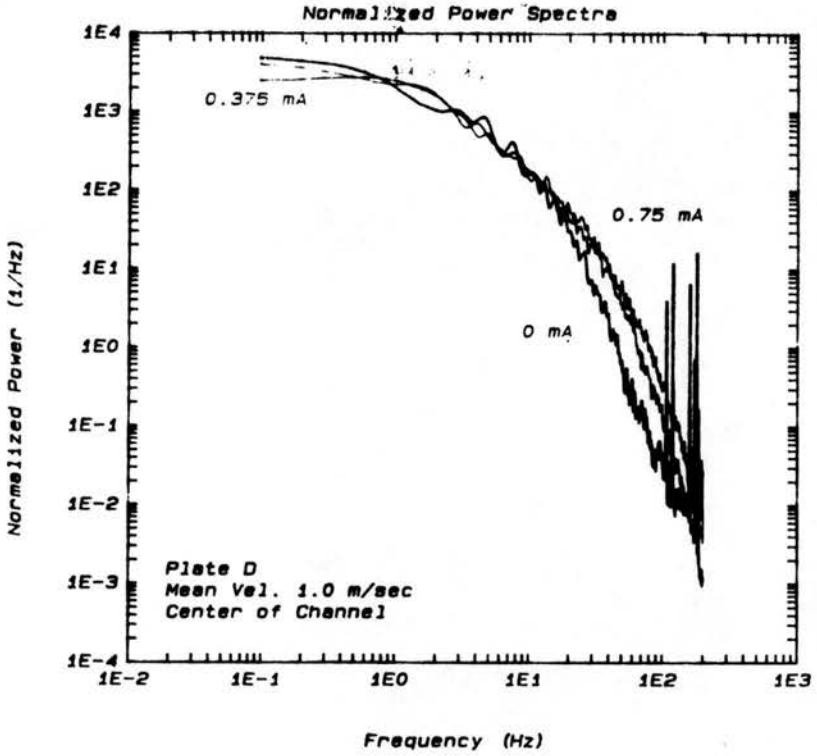

Figure 4.90. Normalized power spectra in plate D geometry at 1.0 m/s.

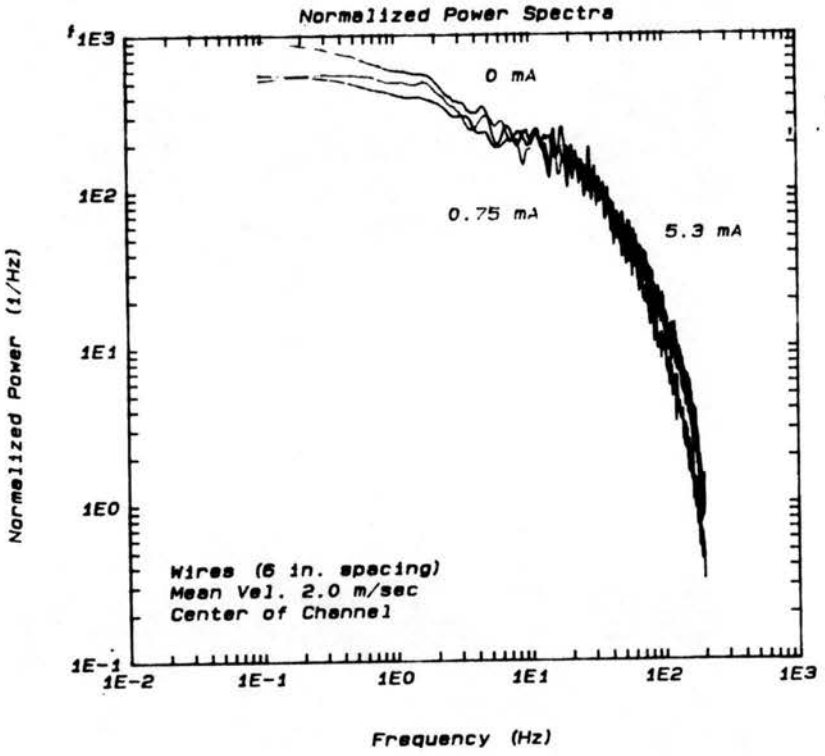

Figure 4.91. Normalized power spectra in wire-plate geometry at 2.0 m/s.

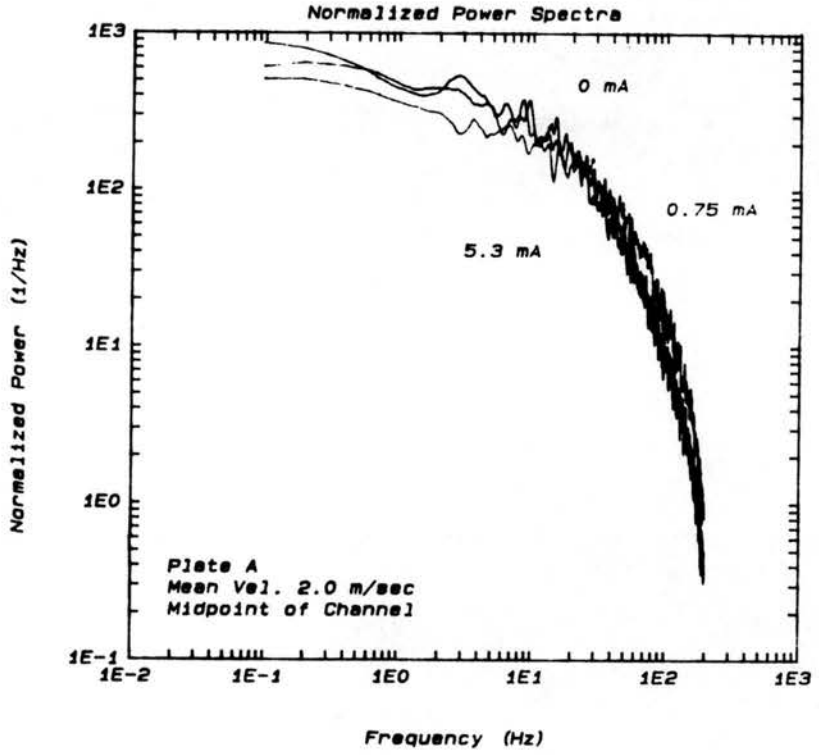

Figure 4.92. Normalized power spectra in plate A geometry at 2.0 m/s.

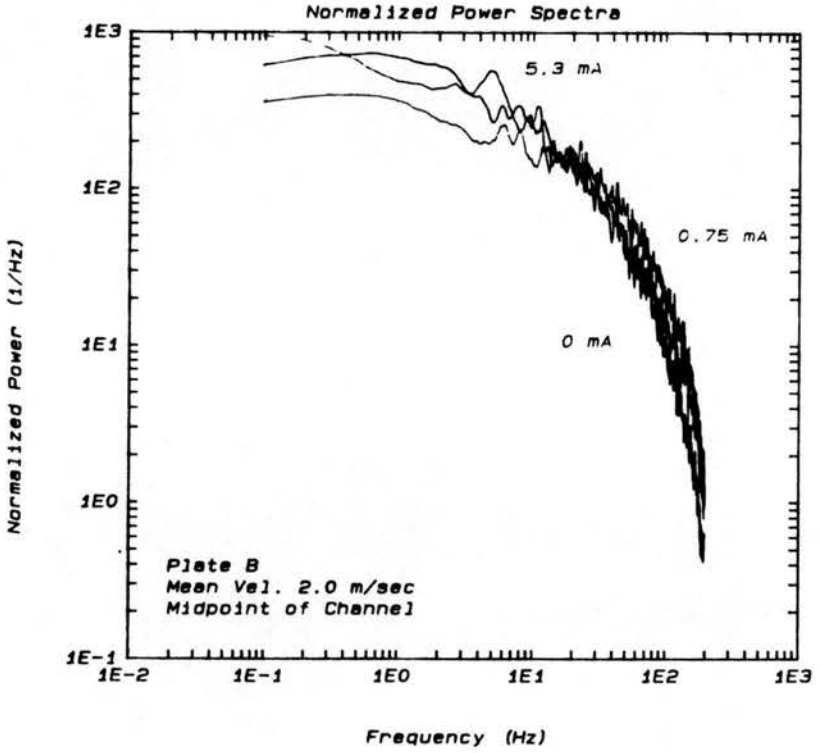

Figure 4.93. Normalized power spectra in plate B geometry at 2.0 m/s.

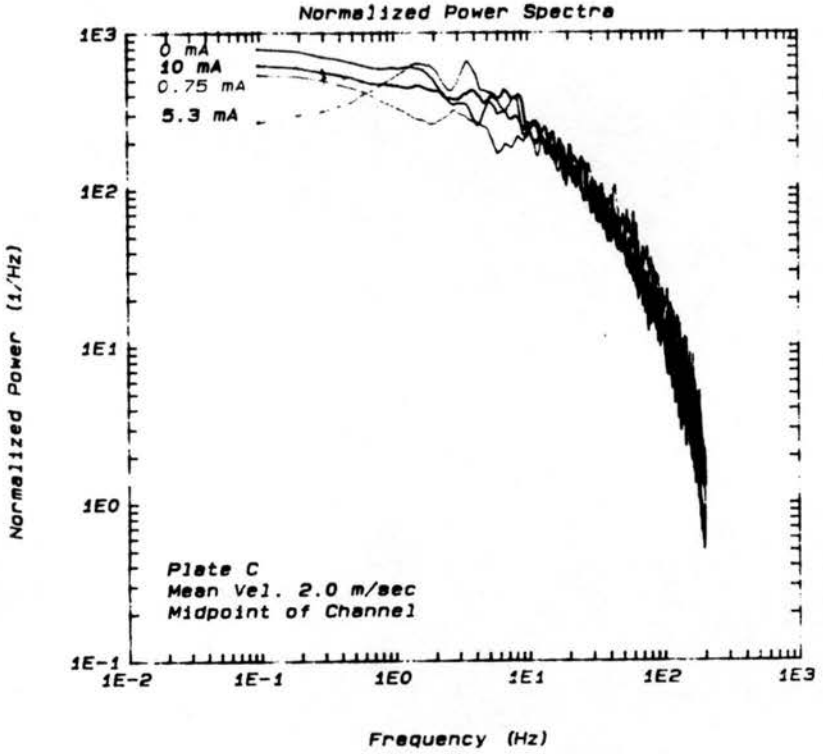

Figure 4.94. Normalized power spectra in plate C geometry at 2.0 m/s.

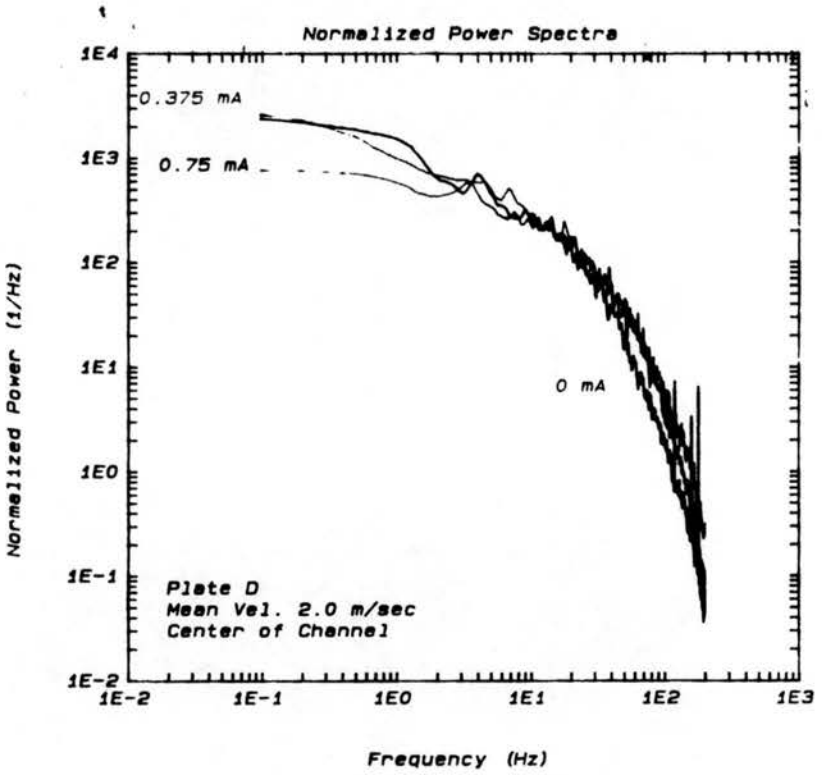

Figure 4.95. Normalized power spectra in plate D geometry at 2.0 m/s.

significant modification of the spectral shape due to current increase at 1.0 m/sec in the case of the wire electrodes shown in Figure 4.86, as compared to that of all planar electrodes, shown in Figures 4.87 through 4.90.

Figure 4.84 shows that at a gas speed of 0.5 m/sec the structure of turbulence produced by plate C changes significantly with an increase in current density. As compared to the no-current normalized spectrum, plate C produces a greater proportion of high frequency turbulence at 0.75 and 5.3 mA. At a current of 10 mA, however, the normalized spectral shape is once again similar to that of the no-current case. The reason for this phenomenon is unclear, but may be the result of a strong secondary flow not present at lower current levels. At a bulk gas velocity of 2.0 m/sec, no significant change in the structure of turbulence is created by corona discharge, as evidenced by Figures 4.91 through 4.95.

4.2.10 Effect of Geometry on Normalized Power Spectra

Figures 4.96 through 4.104 are plots of the normalized spectra grouped by gas speed. Geometry has no significant effect on spectral shape except that due to the wider channel of plate D. In this geometry, the low frequencies are favored both with and without a corona discharge.

4.2.11 Integral Length Scales

Turbulent motion is characterized by a wide range of eddy sizes, but it is the large scale motions which are primarily responsible for particulate mixing. The integral length scale (Eq. 3.16) is computed

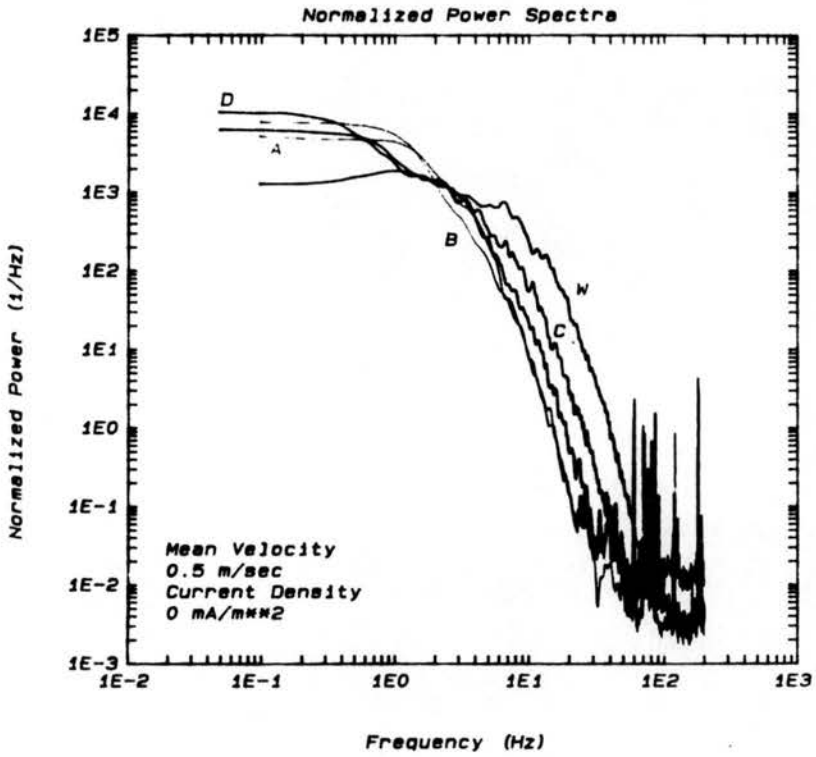

Figure 4.96. Normalized power spectra at 0 mA/m^2 and 0.5 m/s of all electrode geometries.

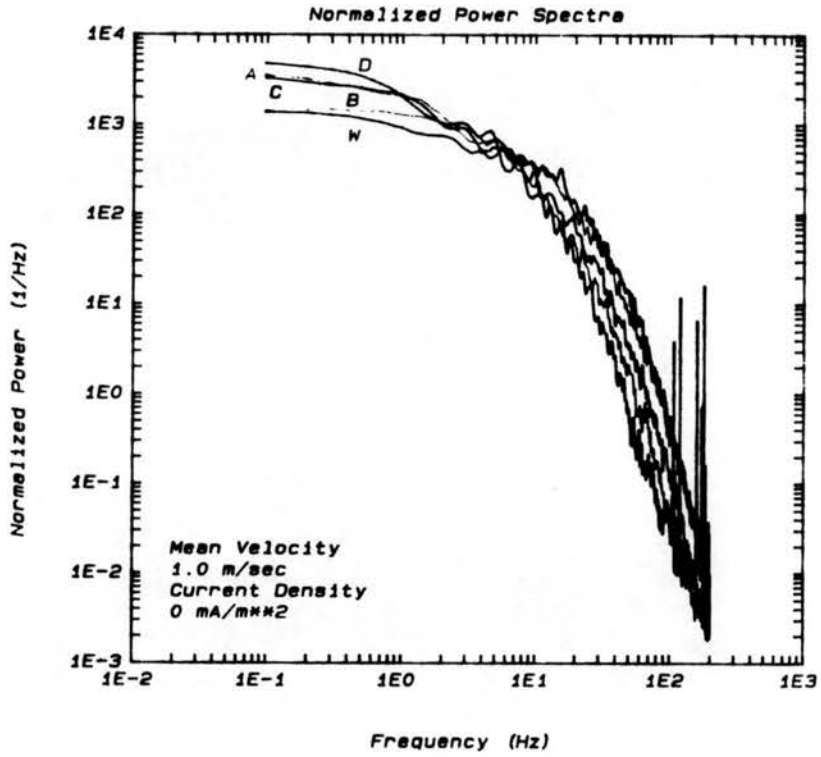

Figure 4.97. Normalized power spectra at 0 mA/m^2 and 1.0 m/s of all electrode geometries.

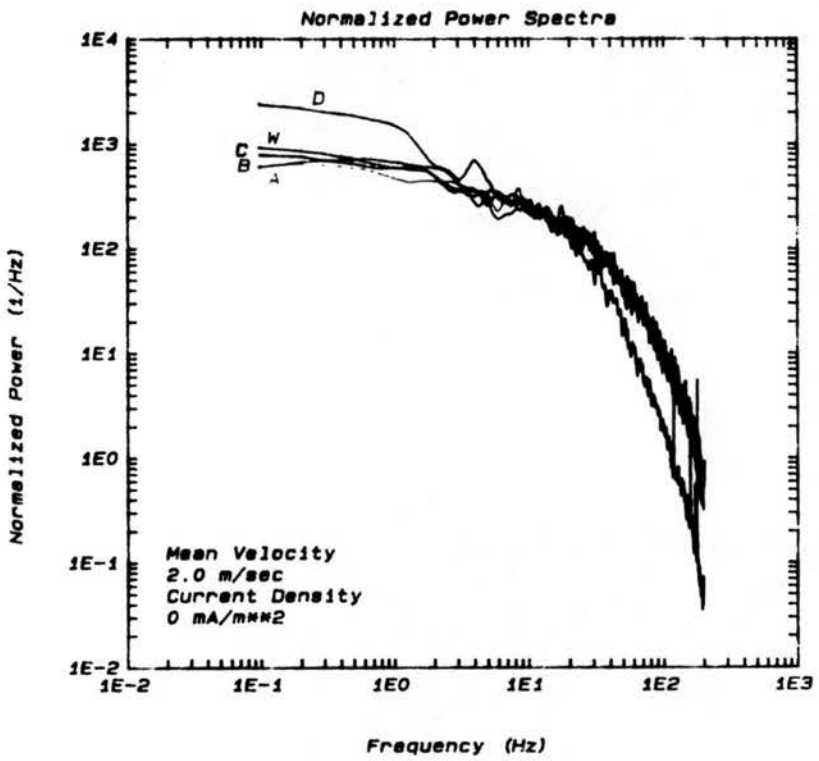

Figure 4.98. Normalized power spectra at 0 mA/m^2 and 2.0 m/s of all electrode geometries.

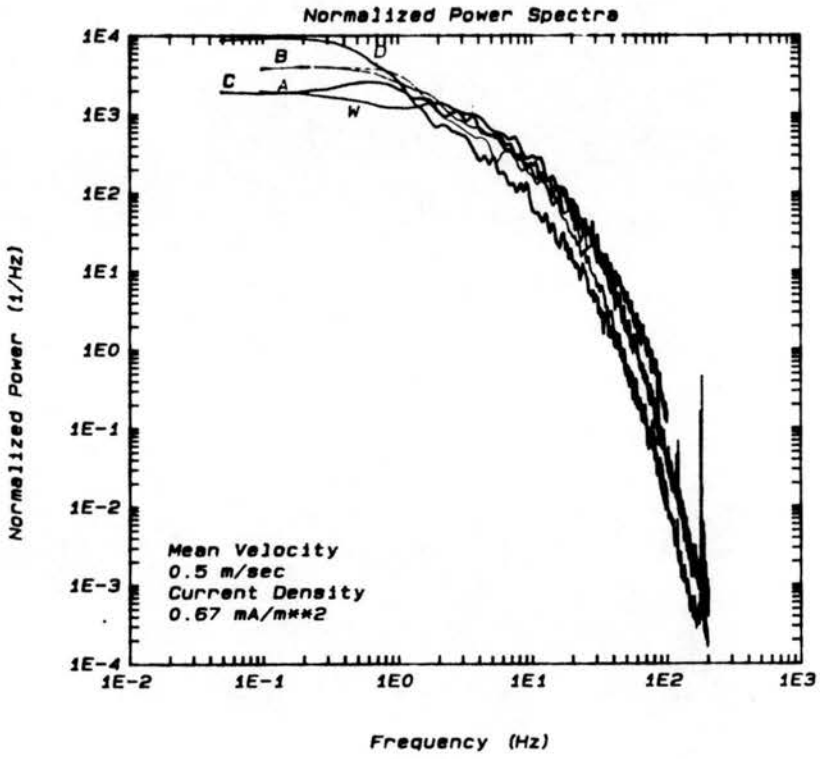

Figure 4.99. Normalized power spectra at 0.67 mA/m^2 and 0.5 m/s of all electrode geometries.

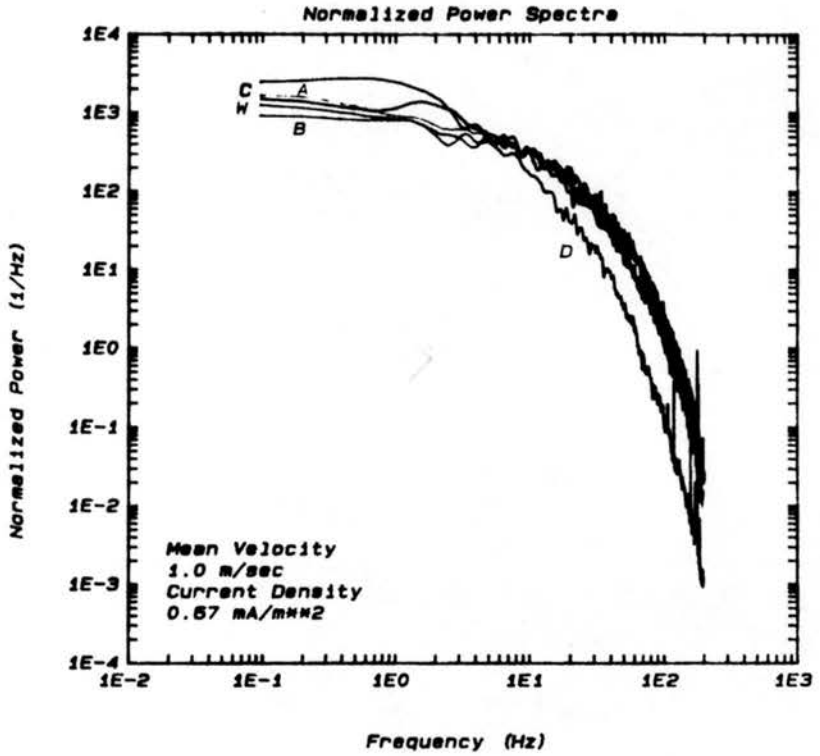

Figure 4.100. Normalized power spectra at 0.67 mA/m^2 and 1.0 m/s of all electrode geometries.

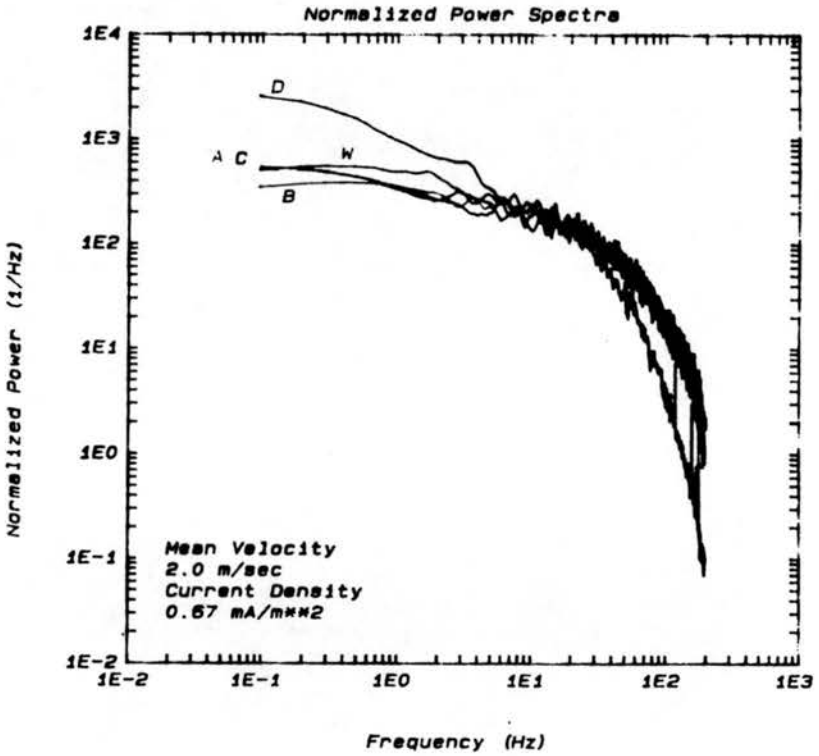

Figure 4.101. Normalized power spectra at 0.67 mA/m^2 and 2.0 m/s of all electrode geometries.

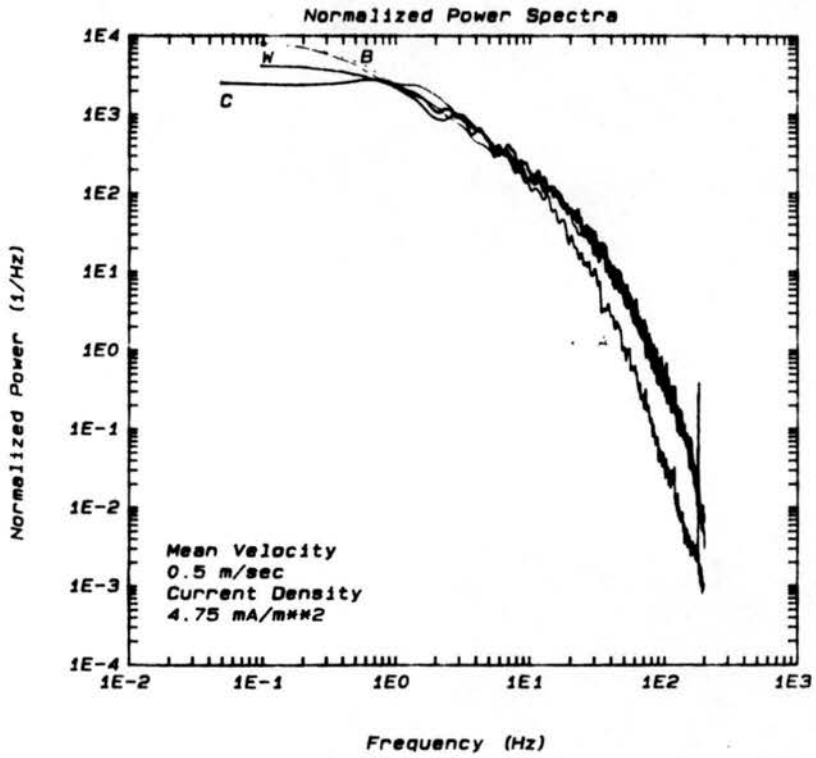

Figure 4.102. Normalized power spectra at 4.75 mA/m^2 and 0.5 m/s of all electrode geometries.

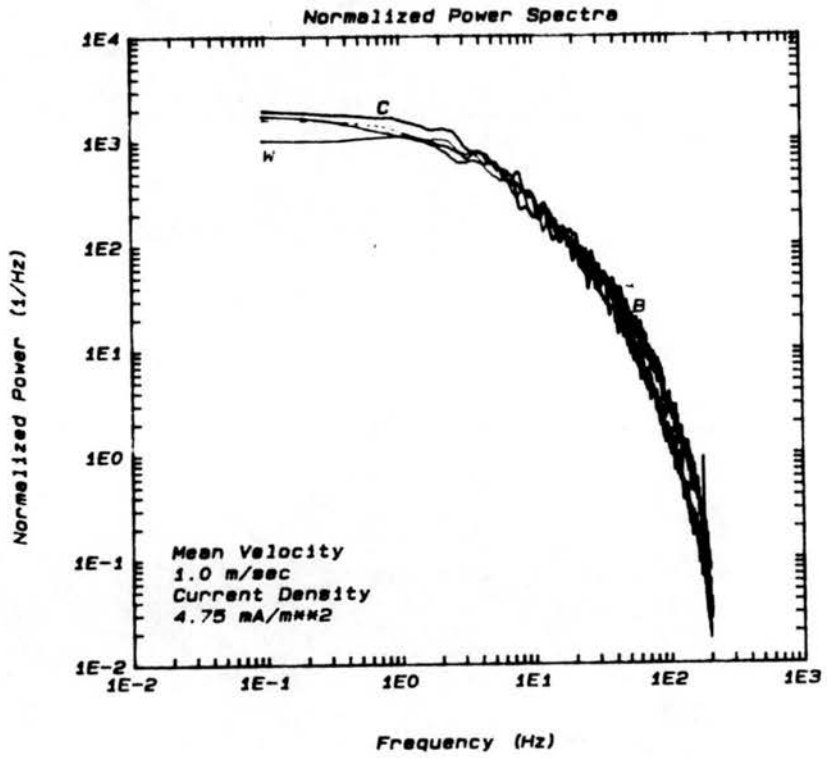

Figure 4.103. Normalized power spectra at 4.75 mA/m^2 and 1.0 m/s of all electrode geometries.

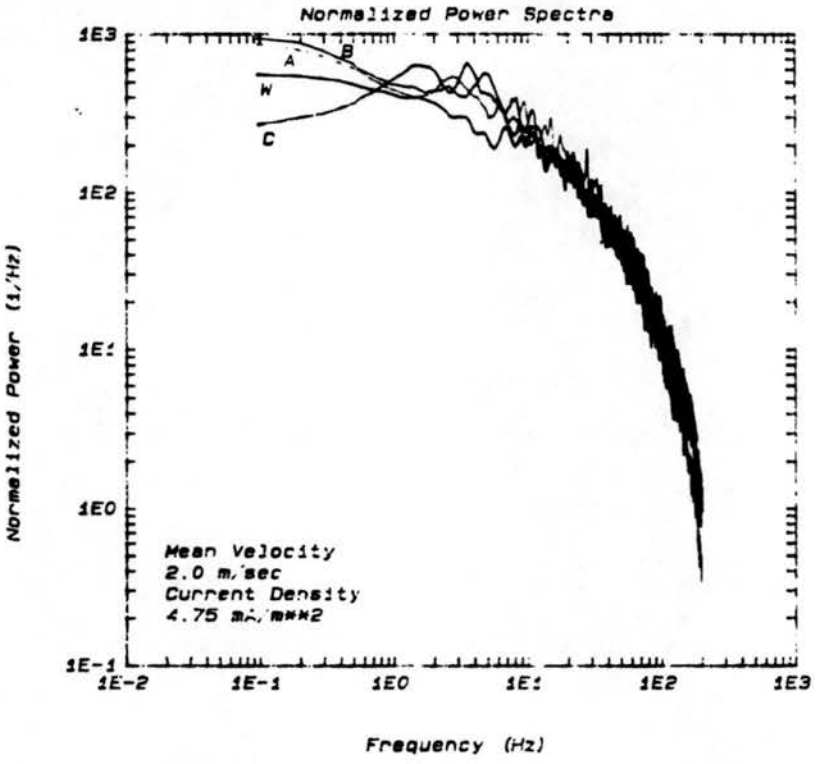

Figure 4.104. Normalized power spectra at 4.75 mA/m^2 and 2.0 m/s of all electrode geometries.

from the autocorrelation and represents an average or characteristic eddy size.

The integral length scales for all electrodes are plotted as a function of current density in Figures 4.105, 4.106, and 4.107. At all gas speeds, and for all geometries, the onset of corona causes a sharp decrease in the integral length scale. As seen with the laser light sheet, the structure of the background aerodynamic turbulence is "broken-up" by the the jet-like structure of the EHD secondary flow. The larger scales of the plate D electrode are the result of the wider channel geometry. The same scales are not observed for the wire electrodes probably because the wires discharge causes a jet-like flow on both sides of the channel.

After the initial drop in length scales associated with the onset of corona, the length scales change very little with an increase in current density. This is true for all electrodes, with one exception. The wire-plate geometry generates an increase in length scale from 2 to 4 cm when the current density is increased from 0.67 to 4.75 mA/m^2, as shown in Figure 4.105. This suggests that a secondary flow is being generated by the stronger current.

Figures 4.106 and 4.107 show that the wire-plate and all half-channel planar geometries produce similar length scales with the corona on at gas speeds of 1.0 and 2.0 m/sec (approximately 3 cm and 2 cm, respectively). This is not the case at a bulk velocity of 0.5 m/sec (Figure 4.105), when plate B produces a 5 cm length scale, plates A and C produce a 3 cm length scale and the wire-plate geometry is not constant, but rises with current density as described above.

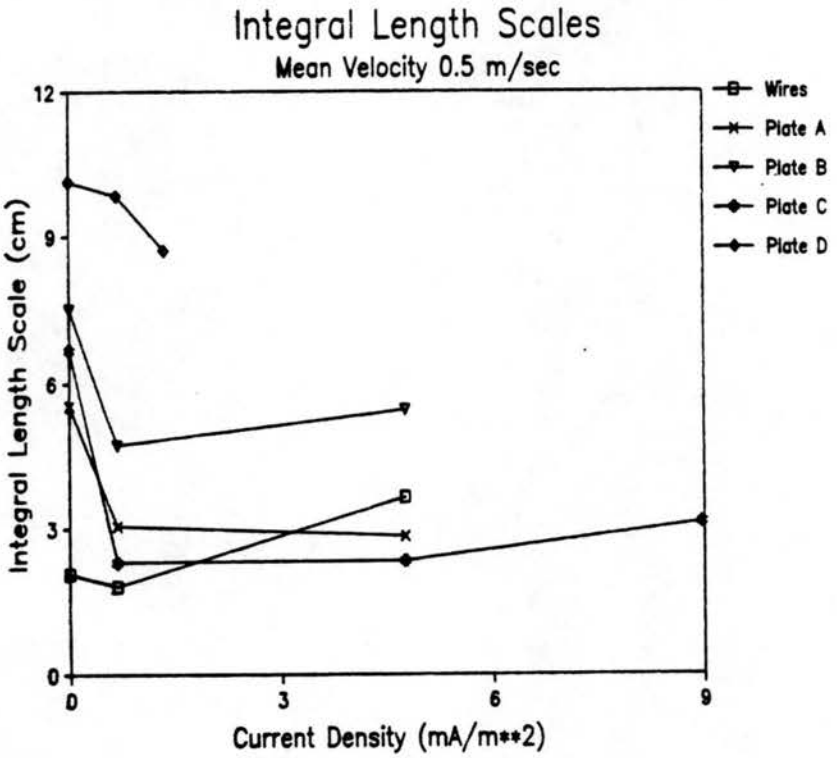

Figure 4.105. Plot of integral length scale as a function of current density at 0.5 m/s.

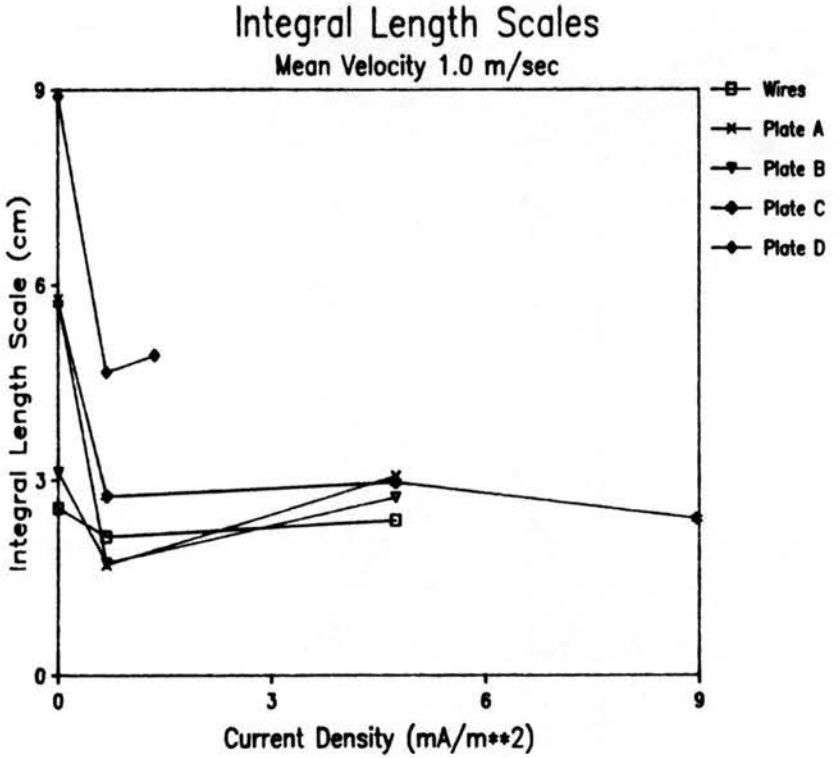

Figure 4.106. Plot of integral length scale as a function of current density at 1.0 m/s.

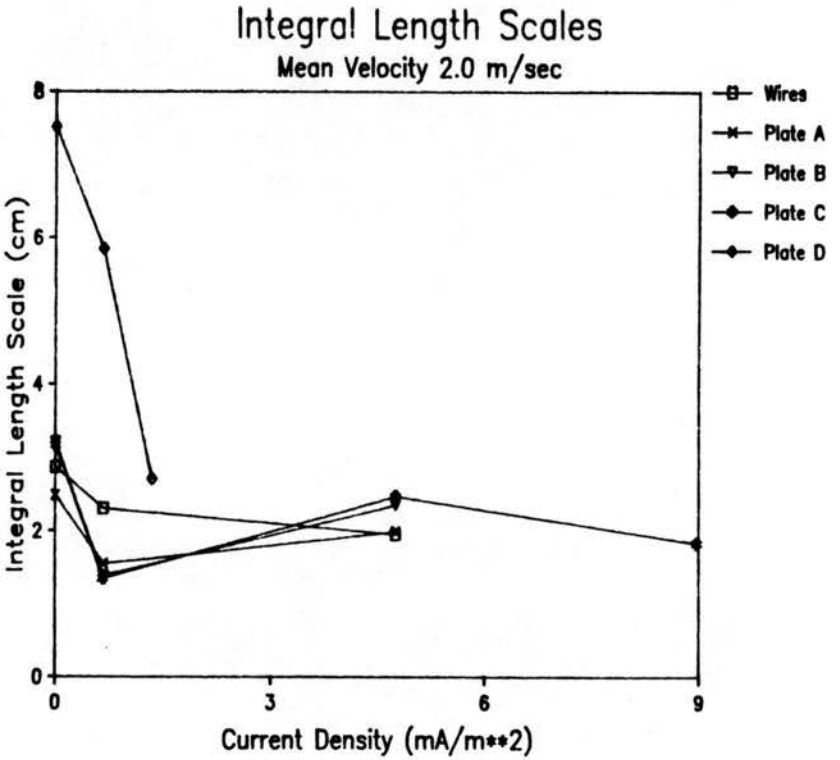

Figure 4.107. Plot of integral length scale as a function of current density at 2.0 m/s.

4.2.12 Eddy Diffusivities

The eddy diffusivities plotted in Figures 4.108, 4.109, and 4.110 as a function of current density are a measure of turbulent mixing within the flow and are calculated as the product of the integral length scale and the rms velocity. It has been observed (e.g. Feldman (1977) and Leonard et al. (1980,1981)) that an increase in turbulent mixing, and thus eddy diffusivity, is detrimental to the particle collection process in an electrostatic precipitator. As long as particle size is small, particles will closely follow the velocity fluctuations within the turbulent flow field and the particle diffusivity will be nearly identical to the eddy or turbulent diffusivity. Fuchs (1964) shows that neutrally buoyant particles with a radius less than or equal to 30 μm are completely entrained in the flow. The largest fly ash particulates in industrial precipitators fall within this range, as reported by Holzhauer (1985). However, since large particles in a precipitator have corresponding high electric migration velocities, it is not realistic to expect that they follow the gas motion. Certainly, fine particles from approximately 0.5 to 3 or 4 μm are entrained by the turbulent eddies. Thus, the eddy diffusivity is useful in predicting the fluid dynamical merits of the electrode geometries tested.

The general trend for all electrodes is that diffusivities rise with both bulk gas velocity and precipitator current density. At a bulk velocity of 2.0 m/sec the rise in diffusivity due to current density is negligible due to the small electric numbers at this velocity. In general, the planar electrodes generate higher diffusivities than the wire-plate configuration at all gas velocities and current densities. The exception occurs at a gas speed of 0.5

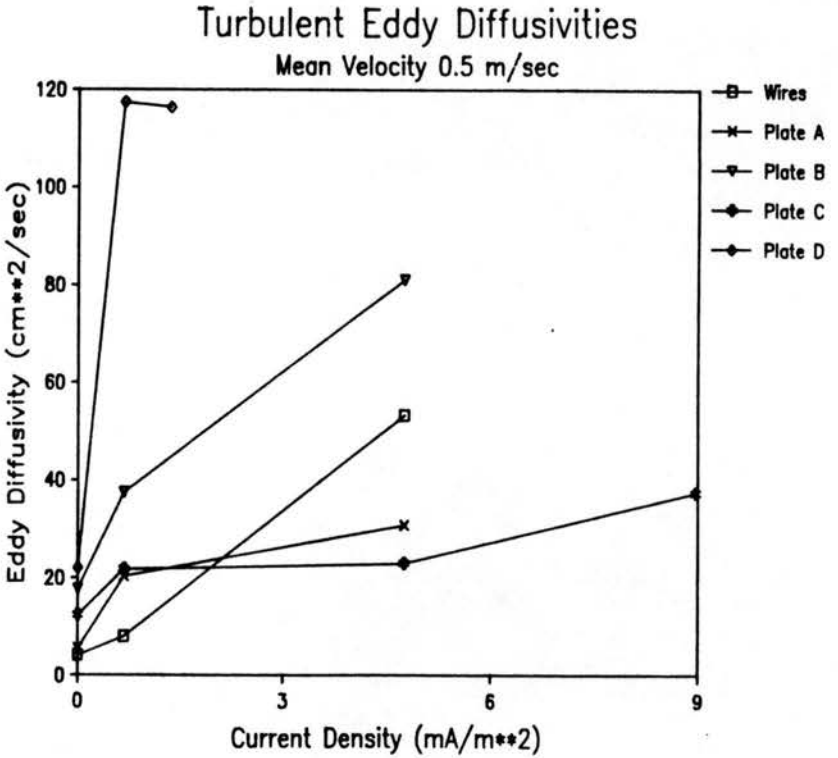

Figure 4.108. Plot of turbulent diffusivities as a function of current density at 0.5 m/s.

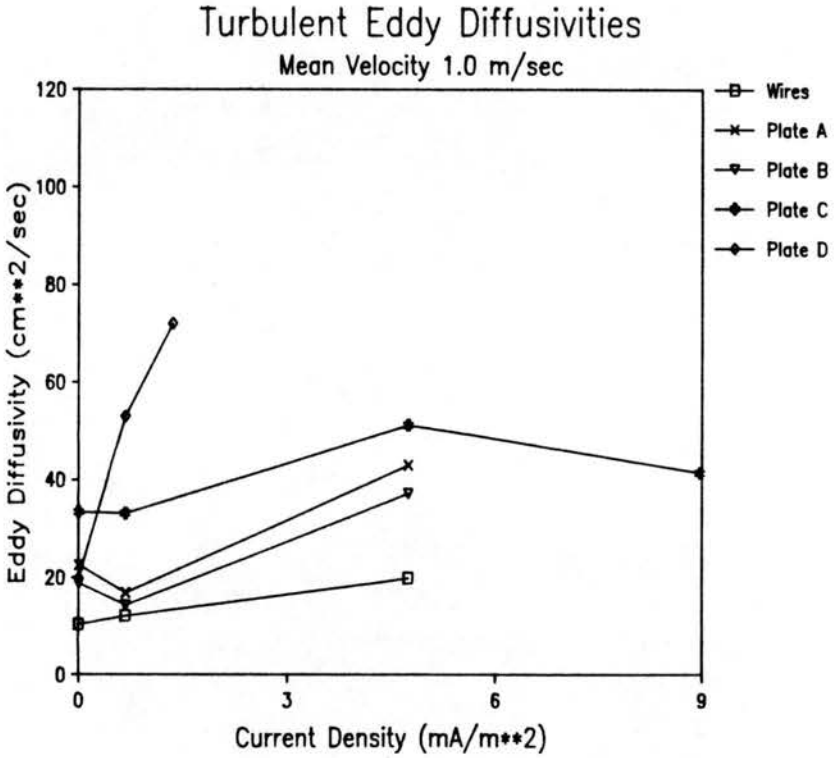

Figure 4.109. Plot of turbulent diffusivities as a function of current density at 1.0 m/s.

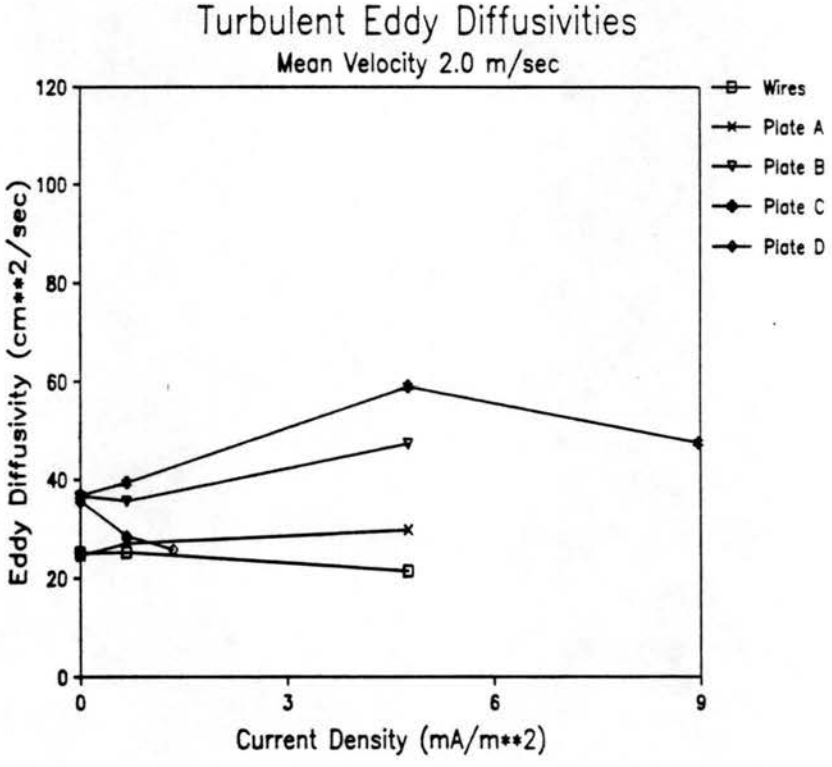

Figure 4.110. Plot of turbulent diffusivities as a function of current density at 2.0 m/s.

m/sec and a current density of 4.75 mA/m^2, as illustrated in Figure 4.108. Under these conditions the wire-plate design produces a larger diffusivity than plates A and C by a factor of two.

Plate D produces diffusivities higher than both the wire-plate geometry and the other discharge plates at flow speeds of 0.5 and 1.0 m/sec (Figures 4.108 and 4.109). This may be partly due to the secondary flow observed in the visualization study. The differences in diffusivity of the five electrodes is less significant at 2.0 m/sec. In fact, in the plate D full channel geometry, diffusivities actually decrease as current density increases at a gas velocity of 2.0 m/sec, as shown in Figure 4.110. This is an indication that if the edge effects of the planar geometry could be avoided, diffusivities might be decreased even at lower gas velocities.

CHAPTER 5

CONCLUSIONS

Electrohydrodynamic theory suggests that the nonuniform current distribution within the traditional wire-plate electrostatic precipitator induces large scale secondary flows detrimental to the collection efficiency. As a first step in designing a discharge configuration that is more advantageous from both a fluid dynamic and electrical standpoint, a novel barbed planer discharge electrode is designed to provide a more uniform current density. Electrical and fluid dynamic characteristics of four different barbed plate electrodes are evaluated and compared to characteristics of the conventional wire-plate electrode geometry.

Electrical characteristics are studied via current-voltage relationships for each electrode and by direct observation of the corona discharge. Fluid dynamic properties are studied via hot film anemometry and laser light sheet flow visualization. In addition to mean velocity and turbulent intensity calculations, spectral analysis is performed on the time series velocity data. The character of electrically generated turbulence is assessed by inspection of power spectra and use of the spectra to calculate length scales and turbulent diffusivities.

From an electrical standpoint, the novel planar geometries are a success. The current-voltage relationship is not unlike that of the standard wire-plate design and the current density delivered is well

within the range needed for industrial electrostatic precipitation. At higher current levels all barbs discharge and the current nonuniformities are reduced from the wire spacing of the wire-plate design to the barb spacing of the planar geometry, thus reducing the possibility of gas sneakage through areas of low current. One disadvantage of the planar design is that not all barbs discharge at low current levels. In this case, the current distribution is extremely nonuniform. Another disadvantage is that in a retrofit application where the wires are replaced by the barbed plate, the protruding barbs reduce the interelectrode spacing. As a result, sparkover occurs at lower voltage levels. This is easily remedied by increasing the plate spacing; however, this remedy makes retrofitting existing industrial installations more difficult. The increased electrode spacing would require a higher voltage to sustain a discharge on all barbs, as evidenced by the I-V curve of plate D. It has been suggested, however, (Yamamoto and Sparks, 1986) that high voltage, low current precipitators are more effective at controlling back corona with high resistivity ashes.

The fluid dynamic benefits of the planar electrodes are not as clearly defined as the electrical characteristics. Based on the hot-film anemometer measurements made downstream of the active precipitator, it is clear that geometry plays a significant role in turbulence production. At any given value for the dimensionless electric number the turbulence generation by the planar electrodes is as much as double that of the wire-plate precipitator. This increase is most significant for the electrode with the greatest number of discharge barbs (plate C). It is also significant for the full-channel geometry (plate D) at low gas velocities.

There is also a very different relationship between current density and turbulence intensity for the barbed plates and wire electrodes. Turbulence production increases with an increase in current density for all planar electrodes at all bulk gas velocities. Turbulence levels generated by the wire-plate design are relatively insensitive to increases in current density at the higher gas speeds.

The structure of the corona discharge in the two types of geometries provides a reasonable explanation for the difference in flow behavior. The wire discharge consists of discrete tufts that distribute themselves as uniformly as possible along the wire after corona initiation. Although at higher current levels more tufts appear and the existing tufts grow stronger, the tufts continue to re-distribute themselves in the most uniform fashion possible. It is speculated that the highly structured discharge produces circulating secondary flows that become stronger with increasing current in addition to the electrically generated turbulence. The sequence of events for the planar electrodes is quite different. Upon corona initiation only a few barbs discharge. As current is increased, more barbs begin to discharge but tufts do not re-distribute because they are restricted to the barbs. At each discharging barb there is a corona wind jet producing more turbulence.

In designing the planar electrode it was hoped that by decreasing the length scale of the corona discharge nonuniformity, the length scale of the turbulent flow field would also be reduced, thereby increasing the efficiency of the precipitator. Inspection of the spectra of the turbulent velocity measurements indicate that the barbed plates generally increases turbulence without decreasing eddy size. Calculation of integral length scales reveals that the planar

electrodes do not substantially reduce the scale of turbulence, but actually increase it in some cases. Turbulent diffusivities for the planar electrodes are higher than the wire-plate geometry in almost all cases. Exceptions occur for half-channel geometries at high currents and a low gas velocity and for the full-channel configuration at a gas velocity of density 2.0 m/sec. Neither planar electrode discharge barb pattern nor number appears to have an effect on the characteristics of the electrohydrodynamic flow.

In examining these results it must be taken into account that flow field measurements made downstream of the precipitator may not be representative of the actual flow within the precipitator. Plate end effects observed in the visualization procedure may have a significant effect on the downstream flow and substantially bias the data. In order to assess fully the value of the planar electrode design in the fluid dynamics sense, measurements of the flow field within the active precipitator must be made. A laser Doppler anemometer using fine, electrically resistant seed particles is one possible system for making such measurements.

Although the value of a planar electrode design is inconclusive from a fluid dynamics standpoint, there are many other characteristics that need to be explored before the idea is dismissed entirely. As mentioned above the planar electrode does restructure the discharge so as to reduce areas of low current, as opposed to the wire-plate design. In the wire-plate geometry, the EHD flow carries fine particles away from areas of high current near the discharge tufts and into areas of lower current density. This gas sneakage decreases efficiency by reducing particle charging and thus particle migration velocity in the direction of the collector plates. The barbed plate

electrode design may substantially improve precipitator performance by reducing sneakage. Other effects of geometry which must be considered include current distribution at the collector as it affects back corona and electro-mechanical clamping of the precipitated dust layer.

The most important test of any new precipitation design is its particle collection efficiency. There is a need for more experimentation with the barbed electrode geometry to assess fully its ability to improve precipitator performance.

REFERENCES

Akins, R. E., and Peterka, J. A., 1975, "Computation of Power Spectral Densities and Correlations Using Digital FFT Techniques," Technical Report # CER75-76REA-JAP13, Eng. Res. Center, Colorado State University.

Atten, P., McCluskey, F., and Lahjomri, A., 1985, "Electrohydrodynamic Simulation of Electrostatic Precipitators," IEEE/Trans. on Indus. Applications, 50 A, 1528-1533.

Atten, P., McCluskey, F., and Lahjomri, A., 1987, "The Electrohydrodynamic origin of Turbulence in Electrostatic Precipitators," IEEE Trans on Indus. Applications, IA-23, 4, 705-711.

Bendat, J. S., and Piersol, A. G., 1971, Random Data: Analysis and Measurement Procedures, New York:Wiley.

Bingham, C., Godfrey, M. D., Tukey, J. W., 1967, "Modern Techniques of Power Spectrum Estimation," IEEE Transactions on Audio and electroacoustics AU-15, 2, June, 56-66.

Blier, B. H., Jan. 19, 1971, "Electrostatic Precipitator," U.S. Patent 3,555,818.

Bridge, J. H., Oct. 9, 1906, "Electrically Treating Air or Other Gases," U.S. Patent 832,767.

Chattock, A. P., 1899, "On the Velocity and Mass of Ions in the Electric Wind in Air," Philos. Mag. J. Sci. 48, 401-420.

Davidson, J. H., 1984, "Secondary Flows and Turbulence in Electrostatic Precipitators," Ph.D. Dissertation, Duke University.

Davidson, J. H., and Shaughnessy, E. J., 1984, "An Electrostatic precipitator Facility for Turbulence Research," Proceedings: Fifth Symp. on the Transfer and Utilization of Particulate Control Technology, Kansas City, Missouri, Aug. 1984, (Vol. 2, 30-1; EPA/EPRI, Feb. 1986).

Davidson, J. H., and Shaughnessy, E. J., 1984, "Mean Velocity and Turbulent Intensity Profiles in a Large Scale Laboratory Precipitator," Presented at the Joint Power Generation Conference, Toronto, ASME Paper No. 84-JPGC-APC-1.

Davidson, J. H., and Shaughnessy, E. J., 1986, "Turbulence Generation by Electric Body Forces," Experiments in Fluids 4, 17-26.

Feldman, P. L., Kumar, K. S., cooperman, G. D., 1977, "Turbulent Diffusion in Electrostatic Precipitators," AIChE Symp. Series 165(73), 129-130.

Flippen, L. D., 1982, "Electrohydrodynamics," Ph.D. Dissertation, Duke University.

Fortescue, C. G., Aug. 29, 1922, "Apparatus for Electrical Precipitators," U.S. Patent 1,427,370.

Fichs, N. A., 1964, The Mechanics of Aerosols, New York: MacMillan, 258-259.

Hauksbee, F., 1709, Physico-Mechanical Experiments on Various Subjects, 1st ed., London, 53-64.

Holzhauer, R., 1985, "Cleaning Plant Air with Electrostatic Precipitators," Plant Engineering, 32-36.

Kumaran, A., Leach, R., and Self, S. A., 1983, "Anomalous Readings from Hot-Wire Anemometers in Strong Electric Fields," TSI Quarterly, July.

Larsen, P. S., and Christensen, E. M., 1986, "Secondary Flow and Turbulence in Electrostatic Precipitators," Third International Symposium on Applications of Laser Anemometry to Fluid Mechanics, Lisbon, Portugal.

Larsen, P. S., and Sorenson, S. K., 1984, "Effect of Secondary Flows and Turbulence on Electrostatic Precipitator Efficiency," Atmos. Environment 18, 1963-1967.

Leonard, G. L., Mitchner, M., and Self, S. A., 1980, "Particle Transport in Electrostatic Precipitators," Atmos. Environment 14, 1289-1299.

Leonard, G. L., Mitchner, M., and Self, S. A., 1981, "Precipitation from Turbulent Flows," Proc. Intl. Conf. on Electrostatic Precipitation, Monterey, California, 208-256.

Leonard, G. L., Mitchner, M., and Self, S. A., 1983, "An Experimental Study of the Electrohydrodynamic Flow in Electrostatic Precipitators," J. Fluid Mech. 127, 123-140.

Leonard G. L., Mitchner, M., and Self, S. A., 1982, "Experimental Study of the Effect of Turbulent Diffusion on Precipitator Efficiency," J. Aerosol Sci. and Tech. 13(4), 271-284.

MacDonald, J. R., and Dean, A. H., 1982, Electrostatic Precipitator Manual, Park Ridge, NJ: Noyes.

McKinney, P. J., and Davidson, J. H., 1988, "Microcomputer Based Turbulent Flow Data Acquisition and Analysis - ASYST Extended," Symposium on Small Computers for Fluid Mechanics Analysis and Research, ASME Winter Annual Meeting, Chicago.

Oglesby, S., Jr., and Nichols, G. B., 1978, Electrostatic Precipitation, New York: Marcel Dekker, Inc.

Ramadan, O. E., and Soo, S. L., 1969, "Electrohydrodynamic Secondary Flow," Phys. Fluids 12, 1943.

Robertson, J. A., Jan. 15, 1974, "Apparatus and Method for Electrical Precipitation," U.S. Patent 3,785,118.

Robinson, M., 1963, "The Origins of Electrical Precipitation," Electrical Engineering, 559-564.

Shaughnessy, E. J., Davidson, J. H., and Hay, J. C., 1985, "The Fluid Mechanics of Electrostatic Precipitators," Aerosol Science and Technology 4, 471-476.

Shively, W. L., Harlow, E. V., Apr. 2, 1940, "Gas Treating Apparatus," U.S. Patent 2,195,431.

Steuernagel, W., Apr. 1, 1969, "Electrode Discharge Plate for Dust Collection," U.S. Patent 3,435,594.

Tennekes, H., and Lumley, J. L., 1974, A First Course in Turbulence, Cambridge, Mass., MIT Press.

Ushimaru, K., Butler, G. W., and Milovsoroff, P., 1982, "An Experimental and Theoretical investigation of Electrostatic Precipitators," Flow Res. Rep. 219, Flow Industries, Kent, Washington.

White, J. H., 1963, Industrial Electrostatic Precipitator, Reading, MA: Addison-Wesley.

Yabe, A., Mori, Y., and Hijikata, K., 1978, "EHD Study of the Corona Wind Between Wire and Plate Electrodes," AIAA Journal, 16, 4, 340-345.

Yamamoto, T., and Sparks, L. E., 1986, "Numerical Simulation of Three-Dimensional Tuft Corona and Electrohydrodynamics," IEEE Trans. on Indus. Applications, IA-22, 5, 880-885.

Yamamoto, T., and Velkoff, H. R., 1981, "Electrohydrodynamics in an Electrostatic Precipitator," J. Fluid Mech. 108, 1-8.

APPENDIX A

COMPUTER SOFTWARE FOR DATA ACQUISITION AND ANALYSIS

A menu-driven software program TURBDATA (McKinney and Davidson, 1988), designed for use with the commercially available ASYST (A Scientific System) software on an IBM compatible microcomputer, acquires and analyzes hot-wire anemometer measurements of any turbulent flow. TURBDATA takes advantage of the ASYST scientific software package (MacMillan Software, 866 Third Avenue, New York, New York 10022) to provide hardware flexibility, computational speed, and impressive graphics. The program provides the specific statistical analyses required of a one-dimensional turbulent flow study and is flexible in terms of data acquisition and graphical display. In particular, the program includes computations for the PDF, skewness, kurtosis, power spectra, and integral length scale not expressly included in the ASYST function library. The computer code is copyrighted. For inquiries write to Peter J. McKinney, Engineering Research Center, Colorado State University, Fort Collins, CO 80523.

A.1 Turbdata Overview

An overview of TURBDATA is shown in the flowchart of Figure A.1. The main program is divided into four subprograms: HWCAL, HWDATA, HWAN, and HWPLOT.

The first subprogram, HWCAL, acquires and stores the necessary data for calibration of a hot-wire probe, curve-fits this data to

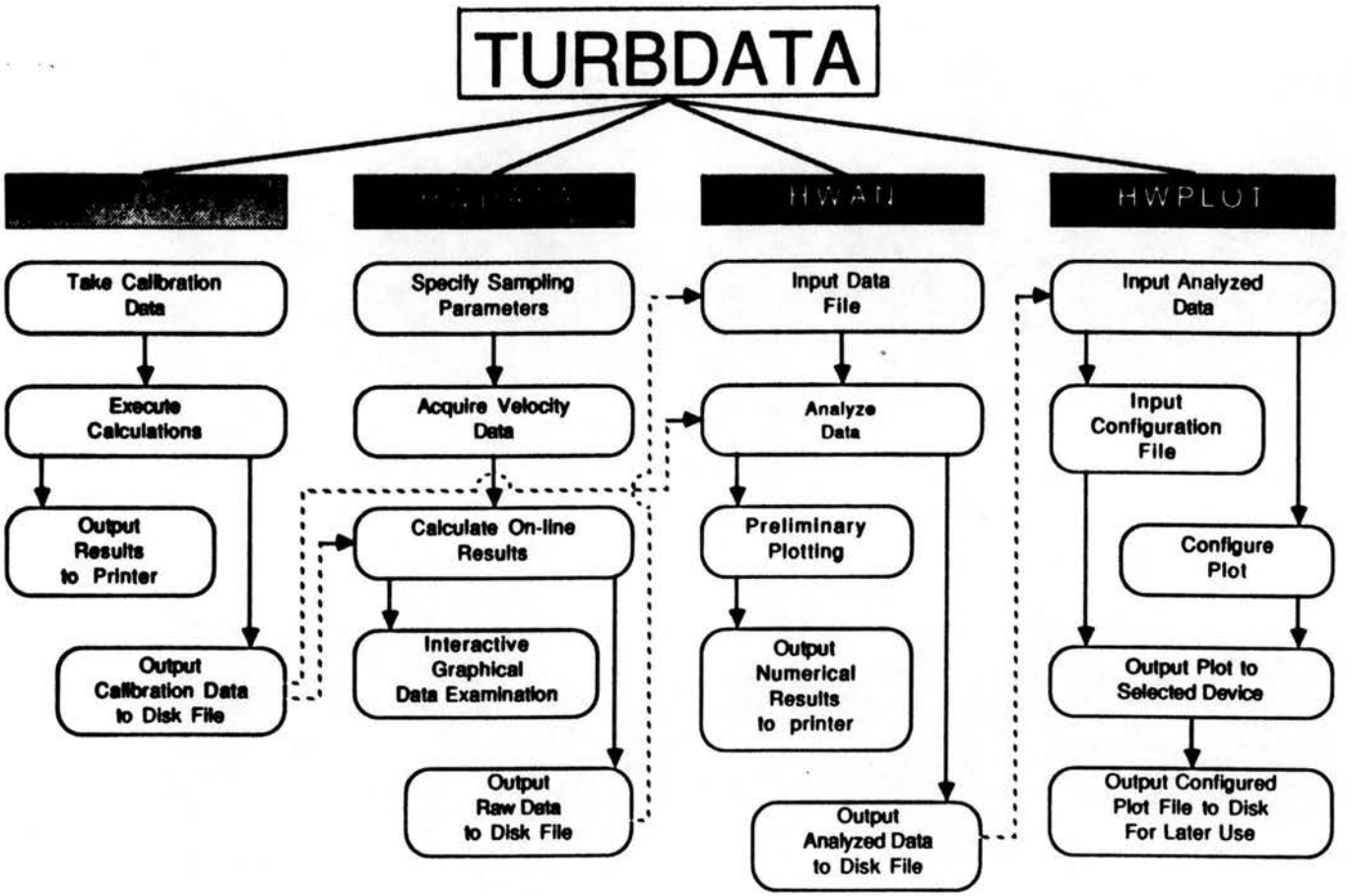

Figure A.1. Overview Flowchart of Turbulent Flow Data Acquisition and Analysis Program TURBDATA

obtain a calibration curve, and then computes and stores the polynomial coefficients relating velocity to bridge voltage. The second, HWDATA, controls the acquisition of anemometer flow measurements and includes some preliminary data analysis. The third, HWAN, completes a one-dimensional statistical analysis of the flow. The fourth, HWPLOT, presents the analyzed data in almost any graphical format.

TURBDATA is currently configured for acquisition and analysis of hot-wire anemometer flow measurements with almost any analog to digital (A/D) data acquisition board and an IBM/XT/AT compatible microcomputer. Minimum system hardware requirements are 640 kB of memory, a hard disk (a minimum capacity of 20 MB is suggested), a two-channel analog-to-digital data acquisition board, and a graphics monitor (monochrome is acceptable).

A.2 Description of ASYST

ASYST (A Scientific System) provides a powerful interpretive interactive environment for IBM/XT and AT compatible computers. Many built-in mathematical and graphical functions as well as a large collection of drivers for analog-to-digital I/O boards and other peripheral devices are included. Once in the ASYST program, a user may type individual commands or "words" and use ASYST in its interpretive fashion, much like a RPN based scientific calculator. Scalar and array variables may be created and manipulated in a stack format using the basic commands.

One of the most powerful features of ASYST is the ability to create user defined "words" which consist of a string of previously defined "words" either existing in the ASYST command library or user

defined. This feature allows the user to create a program in the usual sense by defining a series of functions, each calling upon both basic ASYST commands and user defined "words". "Word" definitions may be entered interactively or from a prepared ASCII code file. The user program may be loaded into the ASYST environment each computing session or stored permanently as part of ASYST.

A.3 Hot-Wire Calibration - The HWCAL Program

HWCAL is designed to quickly and accurately calibrate a hot-wire probe. A program flowchart suggesting a typical operating session is shown in Figure A.2. The program structure assumes that a voltage emitting pressure transducer is used to obtain pressure data for calculation of velocity from the Bernoulli equation. The pressure transducer output and the anemometer bridge voltage output are sampled using two channels of the A/D board. A calibration curve is obtained and an expression for velocity as a function of bridge voltage is computed. The present version of HWCAL is specifically configured for a Thermo-Systems Inc. (TSI) Model 1125 Calibrator. Special features include the ability to edit and view the calibration data, on-screen comparison of the data and the calibration curve-fit, and both hard copy and data file output.

Like the other TURBDATA subprograms, the menu structure of HWCAL is multi-tiered. The initial menu options are shown in Figure A.3. Selection of the first menu option permits the user to specify hot-wire type and serial number, pressure transducer characteristics, fluid properties, and the geometric configuration of the calibration device. The user may then obtain as many as 50 pressure data and corresponding bridge voltage data points on command. Each data point

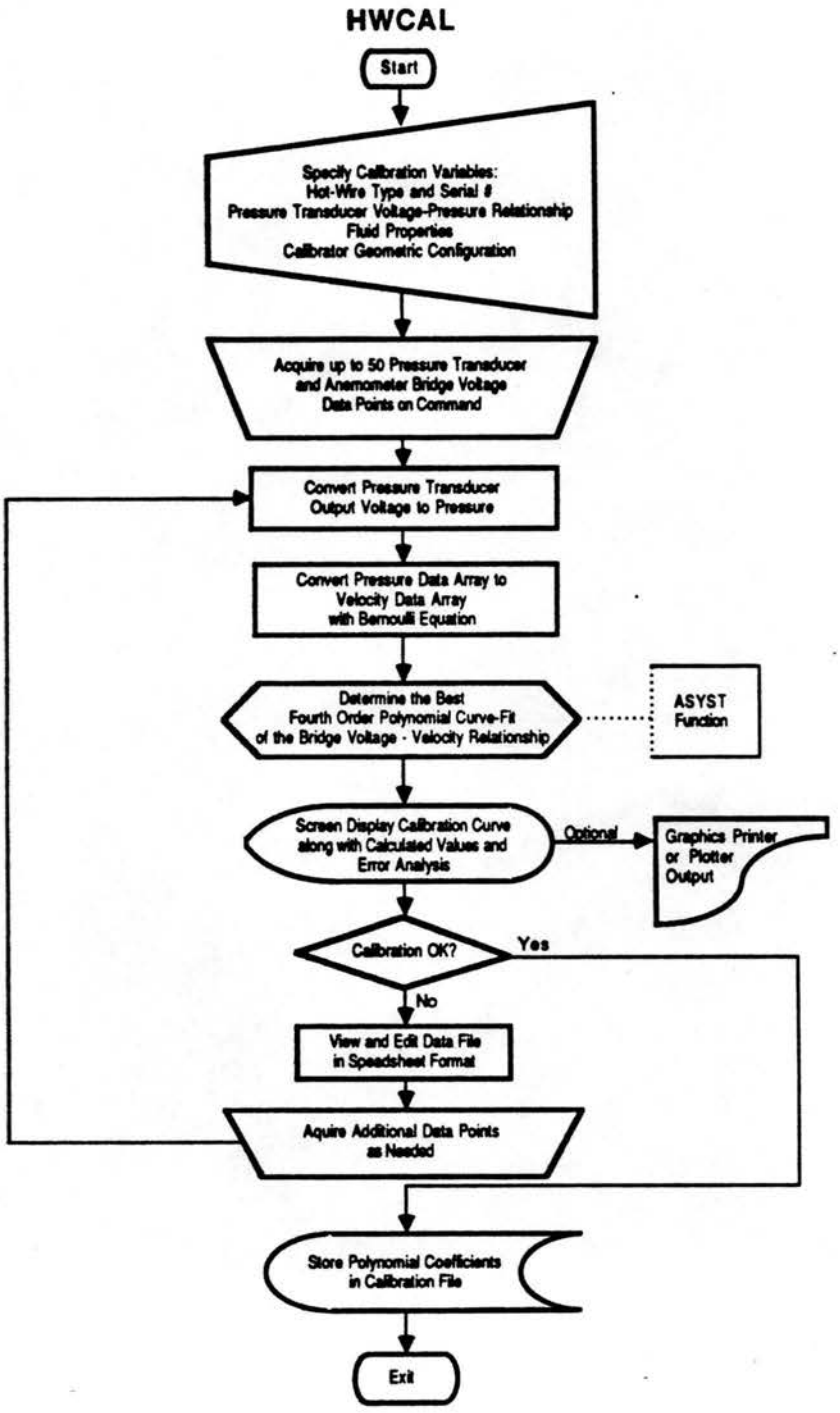

Figure A.2. Flowchart of a Typical Use of the Hot-Wire Calibration Subprogram HWCAL

```
      *** Menu ***

[F1]  Take Calibration Data
[F2]  Display/Edit Data Array
[F3]  Analyze Data
[F4]  Load Data File
[F5]  Save Data File
[F6]  View Data File
[F7]  Execute ASYST Command
[F8]  Initialize Variables
[F9]  Print Data Arrays
[F10] Exit

Make a Selection Please:
```

Figure A.3. Main Menu of HWCAL

is the average of 100 samplings over a 2-second interval. If a simultaneous sample and hold A/D is used, the pressure and bridge voltages are sampled at the same time. Otherwise, the two channels are sampled alternately.

The analysis section of the program calculates the fluid velocity from the measured pressures and uses an ASYST curve-fitting command to obtain a fourth-order polynomial equation relating velocity to bridge voltage. The calibration analysis is completed on-line with immediate graphical screen presentation of the calculated velocities along with the curve-fit and statistical error analysis. The resulting plot may be dumped to a dot matrix or other graphics printer. Figure 3.10 is an example of the subprogram output.

The second menu option permits interactive viewing and editing of the data in a spreadsheet format. Additional data points may be added to the data set after analysis and/or editing to achieve improved accuracy.

Menu options 4 through 6 are file manipulation commands. Calibration data, along with the computer polynomial coefficients and any entered comments, may be saved in a standard ASYST binary file suitable for use by the data acquisition and analysis routines. Options 5 and 6 permit any saved file to be viewed or loaded back into the program data array for further editing or additions.

Menu option 9 provides a tabular output of the calibration data to an attached printer. Option 8 clears all program variables and resets the program so that calibration of a different hot-wire probe may begin. Option number 7 enables the user to enter any ASYST command without leaving the program. Menu item 10 terminates the program. The exit function may be configured so that either the ASYST

session is ended immediately or only the subprogram is exited and the user remains within the ASYST environment.

A.4 Data Acquisition - The HWDATA Program

HWDATA is a general hot-wire data acquisition routine. A flowchart showing a typical user pattern is presented in Figure A.4. The hot-wire bridge voltage output is acquired at user specified sampling rates in single data sweeps as large as 114,688 points. The voltage data is converted to velocity using the polynomial coefficients obtained from a specified calibration file. Features of HWDATA include preliminary plotting of the time series velocity data and calculation of mean and root mean square (rms) velocity values. Extensive error handling is provided to prevent a program crash due to I/O errors. Data may be output to a standard ASYST file with a large text section. Multiple data arrays of up to 16,384 points may be stored in a single data file.

The HWDATA main menu is shown in Figure A.5. Upon selection of menu item 1, the user is prompted for values of sample size, time between samples, input voltage gain, and input voltage DC offset. Data may be acquired in one sweep of up to 16,384 points at sampling rates up to 19,752 Hz. The maximum sampling rate in the present configuration is limited by the ASYST software operating in an XT environment. Higher sampling rates may be obtained using direct memory access (a feature supported by ASYST but difficult to incorporate into a flexible sampling program). Menu item 3 begins acquisition of a single sweep of data as specified.

Menu item 4 is selected to sample more than 16,384 points. Up to 114,688 contiguous data points may be acquired at rates up to 909 Hz.

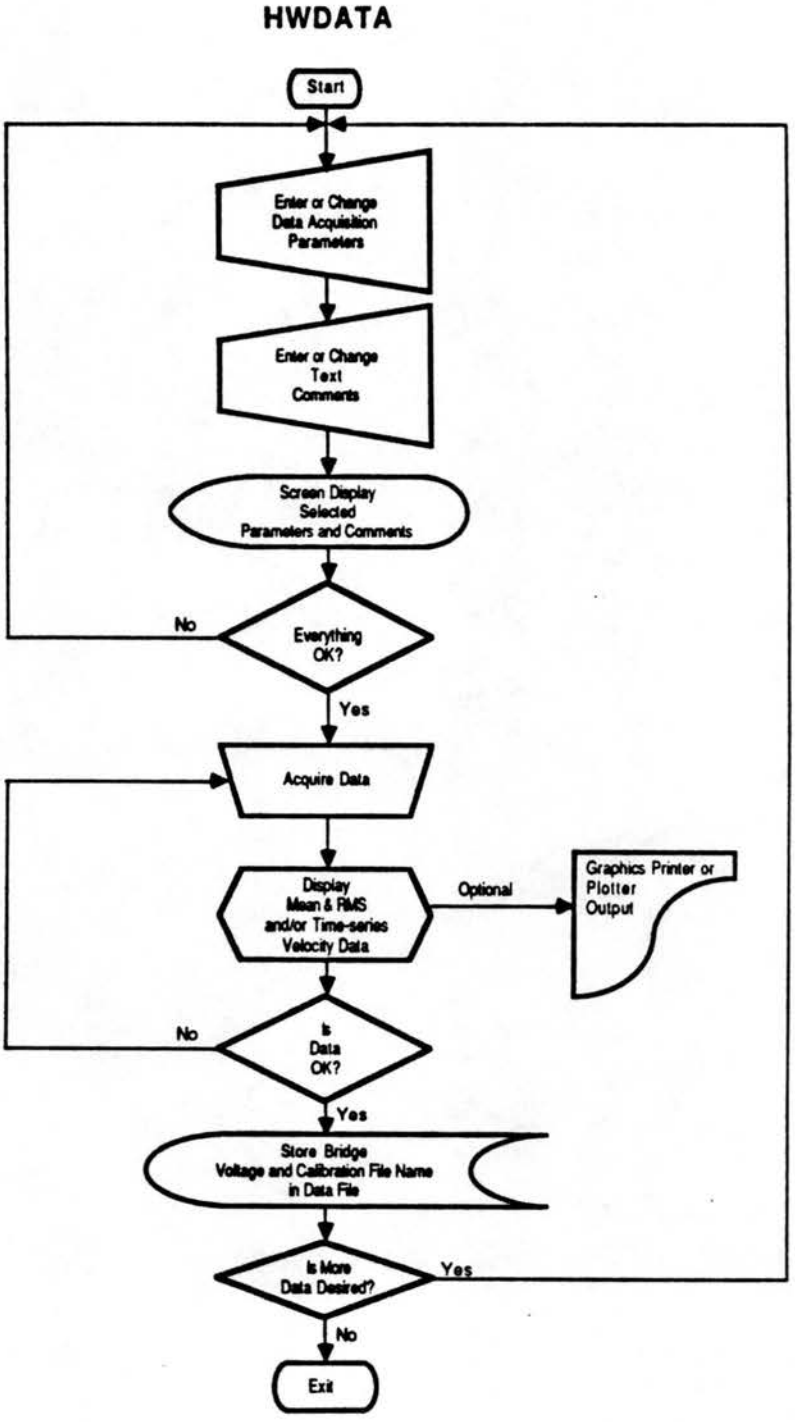

Figure A.4. Flowchart of a Typical Use of the Data Acquisition Subprogram HWDATA

```
*** Hot Wire Data Acquisition ***

[F1]  Set Single Sweep Parameters
[F2]  Enter Descriptive Text
[F3]  Acquire Single Data Sweep
[F4]  Acquire Multiple Data Sweeps
[F5]  Manipulate Files
[F6]  Plot & Calculate
[F7]  Review Profile
[F8]  Initialize Data Arrays
[F9]  Enter Asyst Command
[F10] Exit

Make a Selection Please:
```

Figure A.5. Main Menu of HWDATA

When acquiring more than 16,384 points, the maximum sampling rate is reduced by the need to swap data from the twin 8,192 A/D input buffers to temporary arrays in the remaining available memory. Since all available memory is used for acquired data storage, the data must be stored in a file before any calculations are performed. Therefore, the user is required to have opened a data file using menu option 5 prior beginning the sampling sweep. Once a file has been opened and item 4 is selected, the user is prompted for the number of 16,384 point sweeps (1 - 7) and the sampling rate.

Menu selection number 2 brings up a second tier menu allowing the user to change any of 8 text comment variables, including hot-wire type and serial number as well as calibration file specification. These text strings may be stored in any data file along with the bridge output voltage data. The comment variable text strings may be used to identify the file in terms of the physical phenomena under study (e.g. bulk fluid velocity, probe location, filter settings, etc.).

Main menu item 7 places a parameter status display on the screen. Figure A.6 is an example of this display. The text comment variables as well as data acquisition parameters are indicated.

File creation and manipulation is handled through the main menu option 5. The file manipulation sub-menu allows the user to open, close, or view any ASYST file. A user may create a new data file and store the text strings specified in main menu option 2 in the file, or append a data array to the file. In this manner, multiple sample sweeps may be placed in a single file.

To monitor the fluid flow and data acquisition process, calculation and display of mean and rms velocities is possible prior

```
Single Sweep Data Acquisition Settings:
Number of Data Points to be Taken.....  4096
Time Betwen Data Points (milliseconds).  1.0000
DC Offset.............................  .0000
Gain..................................  1.0000

Multiple Sweep Data Acquisition Settings:
Number of 16,384 Point Sweeps.........  1
Time Betwen Data Points (milliseconds).  1.1000

File Variables:
Currently Open File..................... (none)
Calibration File Specification......... (none)

Text Entries:
H.W. Type...... (no hot wire specified)
H.W. Location.. (no location specified)
Gas Speed...... (no gas speed specified)
H.V. Settings.. (no high voltage settings specified)
Electrode Type. (no electrode type specified)
Comments....... (no comments entered)
Name........... (no name entered)

Press any key to continue ....
```

Figure A.6. Data Acquisition Parameter Screen Display

to entering the analysis subprogram, HWAN. In addition, a plot of the time series data may be displayed on the screen. These options are available through menu option 6. The bridge voltage values may be plotted directly or velocities may be computed and plotted. The calibration file specified in the text entry menu is accessed to obtain the calibration curve coefficients. If a file has not been specified, the user is prompted for the name of one. The plotting options make use of the ASYST command "ARRAY.READOUT" which enables the user to interactively "zoom in" on specific sections of the data series. A help screen is provided to facilitate the use of this option.

Menu options 8 through 10 are similar to the corresponding operations in HWCAL.

A.5 Data Analysis - The HWAN Program

The analysis subprogram, HWAN, computes statistical characteristics of time-series velocity data including mean and rms velocities, turbulent intensity, probability density function (PDF), skewness, kurtosis, one-dimensional power power spectrum and integral length scale. A generalized flowchart of HWAN is shown in Figure A.7. Statistical computations are based on the procedural techniques presented by Bendat and Piersol (1971) and rely to a great extent on the built-in statistical functions provided by the ASYST Analysis package. ASYST does not include functions for determining the PDF or its third and fourth central moments. Thus new functions or "word" definitions are written to compute the PDF, skewness, and kurtosis as well as the integral length scale. Additional features of HWAN include a selection of smoothing techniques for the PDF and spectrum,

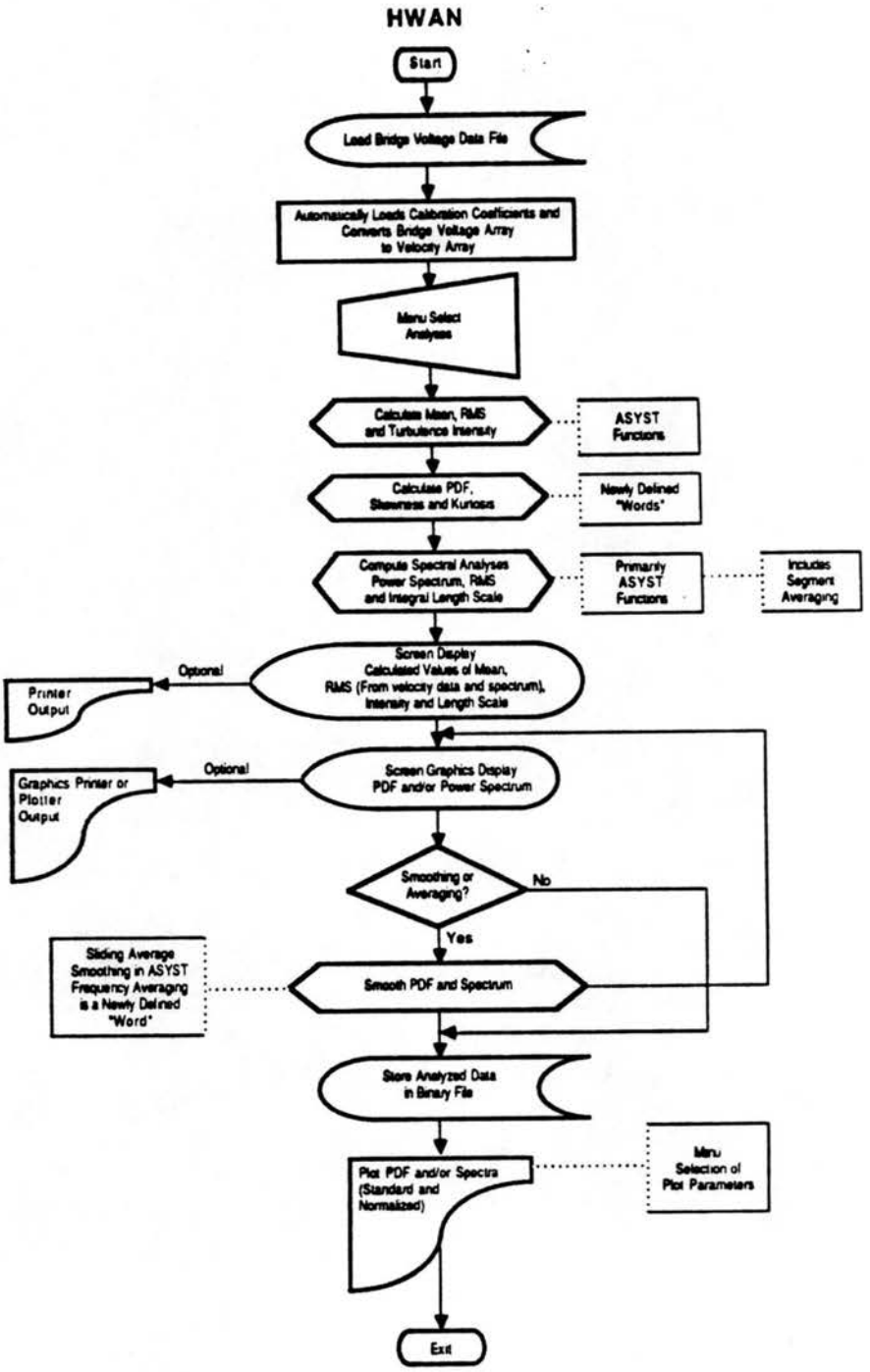

Figure A.7. Flowchart of a Typical Use of the Data Analysis Subprogram HWAN

graphical screen and/or plotter display of the PDF and power spectrum, and output of the analyzed data file in a format compatible with ASYST or easily accessed by other programs.

The main menu of HWAN is shown in Figure A.8. The actual statistical analysis is completed by selecting the first main menu option. A secondary analysis menu permits selection of the desired computations. The user may specify any combination of the statistical properties listed earlier. The rms velocity is determined from both the raw velocity data and by computing the area under the spectral curve. This provides a check of the accuracy of the spectral analysis. The built-in statistical functions of ASYST are used extensively in this portion of the program.

The HWAN program code listed in Figure A.9 is an example of programming in ASYST and illustrates the use of ASYST statistical functions. Each ASYST "word" definition name is preceded by a colon and terminated with a semicolon. The first section of the code referred to as ":MEAN.RMS.I.CALC computes the mean and rms velocities and turbulent intensity from the time series velocity data. Note that direct mathematical manipulation of arrays is possible. Unlike programming in Fortran or Basic, Do-loops are not required. In the second section of code, the power spectrum is computed by completing a 4096 point fast fourier transform (FFT) of the zero mean velocity data to which a cosine taper has been applied. The word ":POWERPASS" first completes a cosine taper of 10 percent of the velocity data at both the beginning and end of the data set, and then computes a 4096 FFT, resulting in a useful power spectrum of 2048 points. (The last half is a mirror image of the first half.) Note the simple use of the ASYST command FFT for computing the fourier transform of the tapered

```
*** Analysis Main Menu ***

[F1]  Analysis
[F2]  View Analysis Results
[F3]  Plot Menu
[F4]  Plot Options Menu
[F5]  File Manipulation
[F6]  Change Plot Title Block Location
[F7]  Edit Plot Title Block
[F8]  Smoothing
[F9]  ASYST Command
[F10] Exit

Your Selection Please:
```

Figure A.8. Main Menu of HWAN

```
: MEAN.RMS.I.CALC
    CR ." Calculating Mean....."
    DATA SUB[ 1 , NPTS ] MEAN MEAN.VEL :=

    CR ." Calculating RMS....."
    DATA SUB[ 1 , NPTS ] MEAN.VEL - 2. ** []SUM NPTS 1 - FLOAT / MS :=
    MS SQRT RMS :=

    CR ." Subtracting Mean From Data....."
    DATA SUB[ 1 , NPTS ] MEAN.VEL - DATA SUB[ 1 , NPTS ] :=

    CR ." Calculating Turbulence Intensity....."
    RMS MEAN.VEL / 100. * TURB.INTENSITY :=

    \ Getting velocity string for title block
    VEL.STRING TITLE @[ 1 ] W:=
;

: POWERPASS
    RANGE 10 / FIX TAPER :=                          \ get taper range
    RAD                                              \ select radians for
                                                     \ trig. operations

    1 TAPER RAMP TAPER FLOAT / PI * COS - 2. /       \ compute left end taper
    DATA SUB[ START , TAPER ] *                      \ multiply data by taper
    DATA SUB[ START , TAPER ] :=                     \ replace data by
                                                     \ tapered data

    1 TAPER TAPER RAMP - TAPER FLOAT / PI * COS - 2. / \ compute right end taper
    DATA SUB[ START RANGE + TAPER - , TAPER ] *       \ multiply data by taper
    DATA SUB[ START RANGE + TAPER - , TAPER ] :=      \ replace data by
                                                     \ tapered data

    DP.REAL.FFT                                      \ set FFT output to be DP
    DATA SUB[ START , RANGE ] FFT                    \ compute FFT

    SUB[ 2 , RANGE 2 / ]                             \ get positve frequencies
                                                     \ greater then 0

    ABS 2. ** ZREAL 2. * DELTA.T .001 * * RANGE /    \ compute power spectra
    0.875 /                                          \ adjust for cosine taper
    10000. *                                         \ convert to (cm^2/s^2/Hz)
    POWERSPEC SUB[ 1 , RANGE 2 / ] +                 \ add to spectral array
    POWERSPEC SUB[ 1 , RANGE 2 / ] :=
;

: SPECTRA.CALC
   CR ." Calculating Power Spectra......."

   0. POWERSPEC :=

    NPTS 4096 <= IF
        CR ."   1 FFT Segment Required"
        CR ."     Beginning Segment 1....."
        1 START := NPTS RANGE := POWERPASS
    THEN
    NPTS 8192 = IF
        CR ."   2 FFT Segments Required"
        CR ."     Beginning Segment 1....."
        1 START := 4096 RANGE := POWERPASS
        CR ."     Beginning Segment 2....."
        4097 START := POWERPASS
        POWERSPEC 2. / POWERSPEC :=
        POWERSPEC[0] 2. / POWERSPEC[0] :=
    THEN
    NPTS 16384 = IF
        CR ."   4 FFT Segments Required"
        CR ."     Beginning Segment 1....."
        1 START := 4096 RANGE := POWERPASS
        CR ."     Beginning Segment 2....."
        4097 START := POWERPASS
        CR ."     Beginning Segment 3....."
        8193 START := POWERPASS
        CR ."     Beginning Segment 4....."
        12289 START := POWERPASS
        POWERSPEC 4. / POWERSPEC :=
        POWERSPEC[0] 4. / POWERSPEC[0] :=
    THEN
;
```

Figure A.9. Section of Code from HWAN

data. Spectral analysis of larger data arrays is possible only by segment averaging since ASYST's FFT routine handles a maximum of 4096 complex values. The segment averaging is completed in the last section of the code listing, ":SPECTRA.CALC", which uses or "calls" the previously defined word "POWERPASS". The integral length scale (not listed in this section of code) is computed from the digitally obtained autocorrelation function.

The second main menu option displays the calculated values of the mean and rms velocities (both the raw data calculation and the spectral determination of the rms value are listed), the turbulence intensity, and the integral length scale. This menu option is designed for checking of the computed values for obvious errors prior to final output of the data file. The values can be dumped to a printer if a hard copy output is desired.

The plot menu option 3 allows the user to select from several data plotting options including: velocity as a function of time (much like an X-Y stripchart recorder), the PDF, the power spectrum, and a power spectrum normalized to unit power obtained by dividing each spectral point by the rms velocity. The plot options menu is used to specify the plot output format and device (either a Hewlett-Packard (HP) plotter and/or graphics monitor from which the plot can be dumped to a graphics printer). Menu selections 6 and 7 are used to specify plot title. More extensive plotting options are available in the graphics subprogram HWPLOT.

Both the probability density function and power spectrum can be smoothed with a nine-point sliding average by selecting menu item 8. Additionally, the power spectrum can be frequency averaged.

File manipulation in HWAN is similar to that described for the data acquisition subprogram HWDATA.

A.6 Graphics - The HWPLOT Program

HWPLOT is an X-Y plotting program designed to take advantage of the ASYST graphics and plotting capabilities and present them in a menu-driven format. The combination of HWPLOT and ASYST provides a degree of flexibility in scaling and graph presentation not found in many commercial plotting programs. Figure A.10 is a generalized flowchart of HWPLOT. The program is directly applicable to the TURBDATA subprograms (such as HWAN analysis file input and power spectra normalizing) but is general enough to use for many plotting needs (ASCII data files may be loaded as well). A variety of HP plotters and video display standards are supported. Up to six data sets may be plotted at one time. Linear or log scales may be used on either axis with automatic or user specified scaling. Plot files may be saved for future editing or batch plotting.

The main subprogram menu is displayed in Figure A.11. Individualized plotting is facilitated through the use of a many-tiered menu system. The second tier menu shown in Figure A.12 is displayed upon selecting main menu item 1. In this menu, the number of data sets and the plot appearance are specified by indicating if certain standard plot components are to be drawn. For example, selection of the title block option places a user specified title on the plot when the plot key (main menu item 3) is pressed. A highlighted bar may be moved among the fields at the right of the screen to enter the desired parameter for each selection. This type

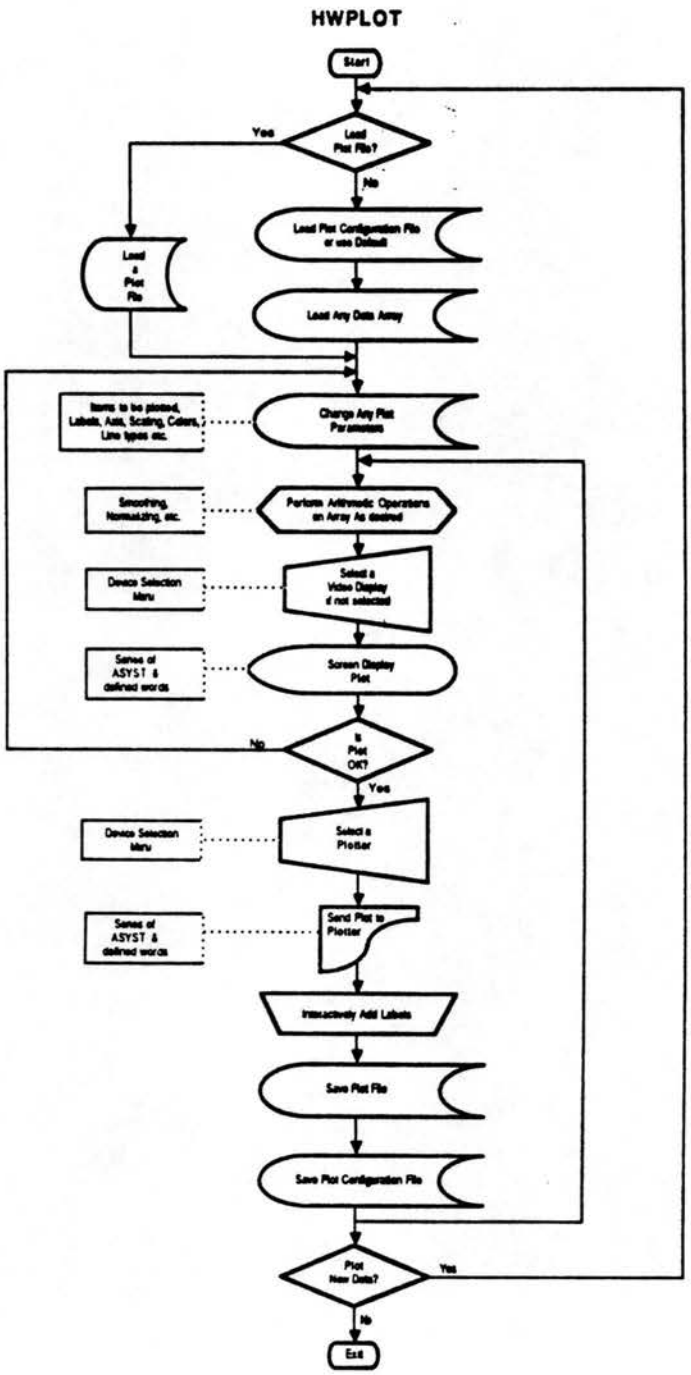

Figure A.10. Generalized Flowchart of the Graphics Subprogram HWPLOT

```
*** Plot Program Main Menu ***

[F1]  Select Plot Items
[F2]  Set Plot Parameters
[F3]  Plot
[F4]  Labelling Menu
[F5]  File Manipulation
[F6]  Change/Initialize Plotting Device
[F7]  Save/Load Options and Plots
[F8]  Array Operations
[F9]  ASYST Command
[F10] Exit

    Your Selection Please:
```

Figure A.11. Main Menu of HWPLOT

```
        *** Plot Item Selection Menu ***

Data Set #1.....                                    1
Data Set #2.....                                    1
Data Set #3.....                                    1
Data Set #4.....                                    0
Data Set #5.....                                    0
Data Set #6.....                                    0
Lower/Left Axis.....                                1
Upper/Right Axis.....                               1
Axis Grids.....                                     0
Line Key.....                                       0
Main Heading.....                                   1
X-axis Label.....                                   1
Y-axis Label.....                                   1
Title Block .....                                   1
Data set number tags.....                           0
Enter label entry mode immediately after plot.....  0

                                    Enter Value <CR>:

Entering a '1' causes option to be plotted.
Entering a '0' causes option not to be used.
Use cursor keys to move up & down, enter <CR> only to exit.
```

Figure A.12. Plot Parameter Specification Secondary Menu of Main Menu Option 1 for HWPLOT

of parameter specification process is used extensively throughout HWPLOT.

Main menu option 2 allows the user to determine the plot size; location and orientation; axis scaling; data character type or data line type for each data set; and label character size and slant. This menu also enables the user to select colors and locations (if applicable) for each of the plot items listed in Figure A.12. The plot scaling selection is a good example of the subprogram versatility. This option, handled in the third tier menu shown in Figure A.13, allows the user to select either automatic or manual scaling.

Plot label texts are specified with main menu item 4. The user may enter text strings for a main menu, the plot heading and a separate title block, the X and Y axes labels, and a curve or data identification key. Outlining is available for the title block and identification kay. This menu also permits interactive labeling of a plot displayed on the screen or plotter.

Other features available from the main menu include a device selection menu (offering several HP plotters and CGA, Hercules, and EGA video modes) and a plot and configuration file menu (main menu item 7). Item 7 permits the user to save and/or load all defined parameters to or from a configuration file for later use. A default configuration file is loaded at the beginning of each session and may be changed to suit the user's needs. The plot data may also be saved along with all parameters in a plot file. This plot file may be reloaded at a later time for reconfiguration and/or plotting.

HWPLOT includes a file manipulation section very similar to the other TURBDATA subprograms. Both ASYST and ASCII files may be

```
*** Scaling Parameter Menu ***

                                    X                Y
Minimum.........................     .0000000         .0000000
Maximum.........................   10.0000000       10.0000000
Number of Divisions.............   10.0000000       10.0000000
First Labelled Tick.............     .0000000         .0000000
Ticks Per Label.................    2.0000000        2.0000000
Tick Size ( 0.0 - 1.0 ).........     .0100000         .0100000
Linear/Log Scale (0/1)..........     .0000000         .0000000
Manual/Auto Scaling (0/1).......    1.0000000        1.0000000
Scaling Factor (linear only)....    1.0000000        1.0000000
Tick Label Width (linear only)..    5.0000000        5.0000000

                                Enter Value <CR>:

An Axis Scaling Factor of 1 is normal scaling.
Tick Label Width is in Units of Characters.
Use cursor keys to change fields, Hit <CR> to exit.
```

Figure A.13. Plot Scaling Third Tier Menu of HWPLOT

accessed with special provisions being made for the loading of power spectra and PDF arrays from an HWAN analysis file. Once loaded, the data arrays may be modified using the "Array Operations" command on the main menu. This submenu enables the user to smooth a curve with a sliding average, perform any mathematical manipulation of a data array (including a special menu selection for computing normalized power spectra), clear or edit a data array, and duplicate any array.

APPENDIX B

NONDIMENSIONALIZATION OF THE NAVIER-STOKES EQUATION WITH ELECTRIC BODY FORCE TERM

The Navier-Stokes equation is given by:

$$\rho \left[\frac{\partial u_i}{\partial t} + u_j \frac{\partial u}{\partial x_j} \right] = - \frac{\partial p}{\partial x_i} + \mu \frac{\partial^2 u_i}{\partial x_j^2} + \rho_c E_i \ . \tag{B.1}$$

Letting,

$$u^* = \frac{u}{U}$$

$$x^* = \frac{x}{L}$$

$$p^* = \frac{p}{\rho U^2} \tag{B.2}$$

$$J^* = \frac{JA}{I}$$

$$t^* = t \frac{U}{L}$$

then the following expressions are obtained,

$$u = u^* U$$

$$x = x^* L$$

$$p = p^* \rho U^2 \qquad \text{(B.3)}$$

$$J = \frac{J^* I}{A}$$

$$t = t^* \frac{L}{U} .$$

Substituting the expression in Eqns. B.3 into Eqn. B.1 with J_i/β substituted for the electric body force, the dimensionless equation of motion is given by,

$$\rho \left[\frac{\partial (u_i^* U)}{\partial \left(t_i^* \frac{L}{U} \right)} + u_j^* U \frac{\partial (u_i^* U)}{\partial (x_j^* L)} \right] = - \frac{\partial (p^* \rho U^2)}{\partial (x_i^* L)} + \mu \frac{\partial^2 (u_i^* U)}{\partial (x^* L)^2} + \frac{J_i^* I}{A\beta} \qquad \text{(B.4)}$$

Eliminating terms and dropping the * notation, the final form of the dimensionless Navier-Stokes equation is given by

$$\frac{\partial u_i}{\partial t} + u_j \frac{\partial u_i}{\partial x_j} = - \frac{\partial p}{\partial x_i} + \frac{1}{Re} \frac{\partial^2 u_i}{\partial x_i^2} + F J_i \qquad \text{(B.5)}$$

where

$$Re = \frac{LU}{\nu} \qquad F = \left[\frac{IL}{\beta A \rho U^2} \right] .$$